JOURNAL OF GEOPHYSICAL RESEARCH, VOL. 102, NO. D19, PAGES 23,429-23,465, OCTOBER 20, 1997

Observing Earth's atmosphere with radio occultation measurements using the Global Positioning System

E. R. Kursinski[1]

Division of Geological and Planetary Sciences, California Institute of Technology, Pasadena

G. A. Hajj, J. T. Schofield, and R. P. Linfield

Jet Propulsion Laboratory, California Institute of Technology, Pasadena

K. R. Hardy

AS&T, Palo Alto, California

Abstract. The implementation of the Global Positioning System (GPS) network of satellites and the development of small, high-performance instrumentation to receive GPS signals have created an opportunity for active remote sounding of the Earth's atmosphere by radio occultation at comparatively low cost. A prototype demonstration of this capability has now been provided by the GPS/MET investigation. Despite using relatively immature technology, GPS/MET has been extremely successful [*Ware et al.*, 1996; *Kursinski et al.*, 1996], although there is still room for improvement. The aim of this paper is to develop a theoretical estimate of the spatial coverage, resolution, and accuracy that can be expected for atmospheric profiles derived from GPS occultations. We consider observational geometry, attenuation, and diffraction in defining the vertical range of the observations and their resolution. We present the first systematic, extensive error analysis of the spacecraft radio occultation technique using a combination of analytical and simulation methods to establish a baseline accuracy for retrieved profiles of refractivity, geopotential, and temperature. Typically, the vertical resolution of the observations ranges from 0.5 km in the lower troposphere to 1.4 km in the middle atmosphere. Results indicate that useful profiles of refractivity can be derived from ~60 km altitude to the surface with the exception of regions less than 250 m in vertical extent associated with high vertical humidity gradients. Above the 250 K altitude level in the troposphere, where the effects of water are negligible, sub-Kelvin temperature accuracy is predicted up to ~40 km depending on the phase of the solar cycle. Geopotential heights of constant pressure levels are expected to be accurate to ~10 m or better between 10 and 20 km altitudes. Below the 250 K level, the ambiguity between water and dry atmosphere refractivity becomes significant, and temperature accuracy is degraded. Deep in the warm troposphere the contribution of water to refractivity becomes sufficiently large for the accurate retrieval of water vapor given independent temperatures from weather analyses [*Kursinski et al.*, 1995]. The radio occultation technique possesses a unique combination of global coverage, high precision, high vertical resolution, insensitivity to atmospheric particulates, and long-term stability. We show here how these properties are well suited for several applications including numerical weather prediction and long-term monitoring of the Earth's climate.

1. Introduction

Given the nonlinear character of the climate system, an understanding of both its natural variability and its response to anthropogenically driven changes in radiative forcing requires long-term observations of temperature structure and water vapor concentrations in the troposphere and stratosphere. These parameters must be measured with sufficient accuracy, resolution, and spatial and temporal coverage to improve our knowledge of the fundamental processes involved in global change [*Houghton et al.*, 1990]. With the development of the Global Positioning System (GPS) satellite network, an opportunity now exists to acquire valuable new temperature, pressure, and humidity data using radio occultation. Timely delivery of occultation data would represent an important, new contribution to the set of observations available for operational meteorology and, in particular, could play a significant role in global numerical weather prediction (NWP). Since the occultations are widely distributed, the data from even one receiver in low Earth orbit (LEO) represents a significant contribution to the global observing system, particularly in remote areas where little high vertical resolution information presently exists. If many such receivers were in LEO, they would represent a very major source of information on the atmosphere's temperature and humidity fields [*Eyre*, 1994]. The unique combination of global coverage, high precision, high vertical resolution, long-term stability, and all-weather viewing, enabled by the long GPS wavelengths, will complement and enhance data sets obtained by existing in situ and remote sounding techniques.

[1]Now at Jet Propulsion Laboratory, California Institute of Technology, Pasadena.

Paper number 97JD01569.
0148-0227/97/97JD-01569$09.00

In radio occultation the radio path between an orbiting transmitter and an orbiting receiver traverses the Earth's atmosphere and is deflected primarily by the vertical gradient of atmospheric refractivity. At radio wavelengths, bending angle is derived from the Doppler shift in the refracted beam, given sufficiently accurate frequency and orbit geometry measurements. Refractivity can then be retrieved from the bending angle profile. From the midtroposphere to the mesosphere, profiles of atmospheric bulk density and therefore pressure and temperature can be derived from refractivity profiles. In the lower troposphere, water vapor also makes a significant contribution to refractivity, so that temperature and water cannot be retrieved independently using the present GPS frequencies. However, radio occultation bending angle and refractivity do provide important constraints on temperature and humidity profiles for numerical weather prediction models. At low latitudes in the lower troposphere, refractivity variations are dominated by water vapor, and high vertical resolution humidity profiles can be retrieved, given independent temperature data.

Radio occultation measurements of the terrestrial atmosphere using signals transmitted by GPS satellites and received by one or more satellites operating in LEO can yield approximately 500 profiles per LEO orbiter daily. High vertical resolution is provided by limb-sounding geometry and a point-like field of view, although in practice, resolution is limited by diffraction effects to approximately 1 km at the limb or lowest height of the radio path. Precision is limited by the accuracy with which the Doppler frequency shift can be determined. Profile measurements are inherently stable in the long-term because frequency is derived either from stable atomic reference clocks or from less stable clocks whose instabilities can be solved for and removed. This resolution and precision can be achieved with modest spacecraft attitude control capabilities, because Doppler shift is independent of spacecraft orientation and both the transmitter and the receiver have broad fields of view. Finally, because GPS occultation measurements are made at radio wavelengths, they are insensitive to particulates, which contaminate many tropospheric remote sounding techniques.

The application of the radio occultation technique to the remote sounding of the Earth's atmosphere was first suggested in the 1960s [*Fishbach*, 1965; *Lusignan et al.*, 1969]. However, to achieve the global coverage and accuracy needed to enhance the existing atmospheric data set, multiple orbiting transmitters and receivers were required at a cost exceeding the level of interest. As a result, the practical and theoretical development of the radio occultation concept was directed toward the remote sounding of planetary atmospheres through a combination of efforts primarily at the Jet Propulsion Laboratory (JPL) and Stanford University. Radio occultation is now well established in the NASA planetary program due to its successful application to the atmospheres of Venus, Mars, and the outer planets through missions including the Mariner, Pioneer, and Voyager series [e.g.. *Fjeldbo et al.*, 1971; *Kliore and Patel*, 1982; *Lindal et al.*, 1983; *Hinson and Tyler*, 1983; *Tyler et al.*, 1986, 1989; *Lindal*, 1991].

Utilization of the GPS network of satellites to characterize the Earth's atmosphere by radio occultation was originally conceived for the NASA Earth Observing System in the form of the GPS Geoscience Instrument (GGI) [*Yunck et al.*, 1988]. Subsequently, GPS radio occultation capabilities and applications have been discussed by a number of authors [*Hardy et al.*, 1992; *Yuan et al.*, 1993; *Gorbunov and Sokolovskiy*, 1993; *Kursinski et al.*, 1995] and have drawn attention in the general literature [*Kerr*, 1992]. The first of a series of opportunities to demonstrate the GGI concept came with the GPS-MET investigation led by the Universities Corporation for Atmospheric Research (UCAR) with funding from NSF, NOAA, and NASA [*Ware et al.*, 1996]. This mission placed a modified TurboRogue receiver developed by JPL and Allen Osborne Associates into a 70° inclination, LEO in April 1995 as an addition to the payload of the Microlab 1 spacecraft developed for NASA by the Orbital Sciences Corporation. The assessment of accuracy and resolution of the initial GPS-MET results has been under way since launch through comparison with radiosondes and satellite data. Our team has focused on comparing occultation results with The European Centre for Medium-Range Weather Forecasts (ECMWF) weather model analyses to take advantage of (1) quality-screened radiosonde and passive sounder data assimilated into the model, (2) the translation of the very different radiosonde and passive nadir-sounding resolutions to the model resolution which is more consistent with that of the occultation observations, and (3) one of the best estimates of the global state of the atmosphere. Initial results indicate rms temperature differences w.r.t. ECMWF are roughly 1.5 K with mean differences of the order of 0.5 K in the northern hemisphere where model results are most accurate [*Hajj et al.*, 1995; *Kursinski et al.*, 1996]. Comparison of geopotential height derived from occultation data with ECMWF agree on average to 10 to 20 m with a scatter of 20 m rms [*Leroy*, 1997]. Poorer agreement in the southern hemisphere presumably reflects the impact of sparse radiosonde data on ECMWF model performance.

While these initial comparison results are very promising, they only establish upper limits on accuracy and resolution because of limitations in the ECMWF model, the assimilated data, and the initial occultation results, which should improve as occultation instrumentation and inversion techniques evolve. The primary goal of this paper is to develop and establish first-order estimates of the resolution and accuracy inherent to the profiles of refractivity, density, pressure, and temperature derived from GPS occultations. This includes the development of a systematic and comprehensive examination of sources of error and their impact on retrieved quantities representing the first such analysis in the 30 year history of the spacecraft radio occultation technique. Such estimates define a baseline of expectation for developers to compare against and explain to those developing methods of assimilating occultation data into models what the sources and characteristics of error are so as to better optimize the assimilation process. Having estimated resolution and accuracy, areas where these features can have a significant impact will be identified and described briefly.

To accomplish these objectives, the paper is structured as follows. It begins with an overview of the occultation concept and technique (sections 2.2 and 2.3). Sources of atmospheric attenuation which may limit the altitude range of the observations are then described together with their impact on measurement sensitivity (section 2.4). The spatial resolution of the observations and derived quantities is then developed in terms of both the vertical weighting contribution to an individual measurement and the diffraction limit (section 2.5). Section 3 presents a detailed examination of sources of error. Finally, having established the vertical range and resolution and expected accuracy, areas in atmospheric science where the occultation observations will have a significant impact are identified and discussed briefly in section 4. This paper focuses almost entirely on the dry atmosphere profiles of density, pressure, and temperature. The accuracy of water vapor retrieved from GPS occultations has been discussed by *Kursinski et al.* [1995], the results of which are summarized in section 2.3.

2. Overview of the Occultation Technique

2.1. GPS Radio Occultation Concept

The GPS consists of 24 satellites, distributed in six orbital planes about the globe. Each satellite orbit is circular, with an

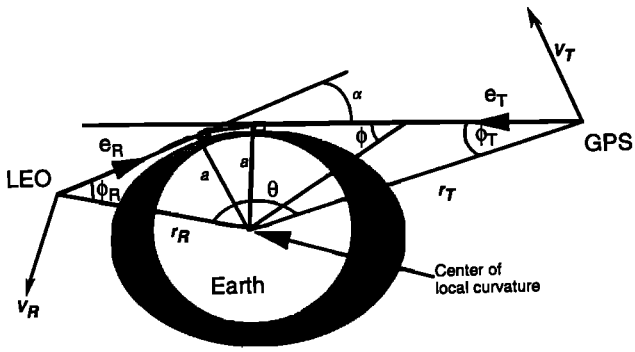

Figure 1. Instantaneous occultation geometry for the Global Positioning System (GPS) and low Earth orbiter (LEO) satellites defining variables for the derivation of α and a from Doppler shift, spacecraft position, and spacecraft velocity measurements.

inclination of ~55°, a period of 12 hours and an altitude of 20,200 km. Although the GPS was designed and developed as a navigation aid by the U.S. Air Force, the civilian community has taken advantage of its capabilities for many additional high-precision applications including now the study of the atmosphere. A schematic representation of atmospheric profiling by GPS radio occultation, using a receiver in LEO, is given in Figure 1. From the standpoint of the receiver, an occultation occurs whenever a GPS satellite rises or sets and the ray path from its transmitter traverses the Earth's atmospheric limb. With 24 GPS satellites, a single GPS receiver in a near-polar orbit at 800 km will observe over 500 occultations per day, distributed fairly uniformly about the globe (Figure 2). This number can be doubled if the receiver is also capable of receiving signals from the Russian Global Navigation Satellite System (GLONASS) constellation, a network similar in function and performance to the GPS. All of these occultations provide useful atmospheric data. The horizontal distribution of coverage depends chiefly on the inclination and period of the LEO satellite orbit. Better coverage is achieved by placing additional receivers in orbit. A set of 25 GPS/GLONASS receivers in diverse low Earth orbits would provide approximately 25,000 daily occultations yielding an average of one profile every 150 km square.

GPS-LEO occultation observations are made in a limb-scanning mode, where vertical scanning is provided by relative motion between the GPS and the LEO satellites (Figure 1). In the geometrical optics approximation, a ray passing through the atmosphere is refracted according to Snell's law due to the vertical gradient of density and hence refractive index. The overall effect of the atmosphere can be characterized by a total bending angle α, an asymptotic ray miss-distance or impact parameter a, and a tangent radius r_t defined in Figure 1 depicting the instantaneous GPS-LEO occultation geometry. During an occultation, as the ray path descends or ascends through the atmosphere, the variation of α with r or a depends primarily on the vertical profile of atmospheric refractive index. This profile can be retrieved from measurements of α as a function of a during the occultation, subject to the assumption of local spherical symmetry (section 2.2).

The time dependence of both α and a during an occultation can be derived from accurate measurements of the Doppler-shifted frequency of the transmitter signal at the receiver. Frequency is obtained from the derivative with respect to time of the signal phase measured by the receiver. Doppler shift is determined by the projection of spacecraft velocities onto the ray paths at the transmitter and receiver, so that atmospheric bending contributes to the measured Doppler shift. Data from several GPS transmitters can be used to establish the precise positions and velocities of the GPS and LEO satellites and to calculate the Doppler shift expected in the absence of bending. The atmospheric contribution to Doppler shift, derived by subtracting the expected shift from the measured shift, can then be combined with satellite position and velocity knowledge to give an estimate of α and a (section 2.2).

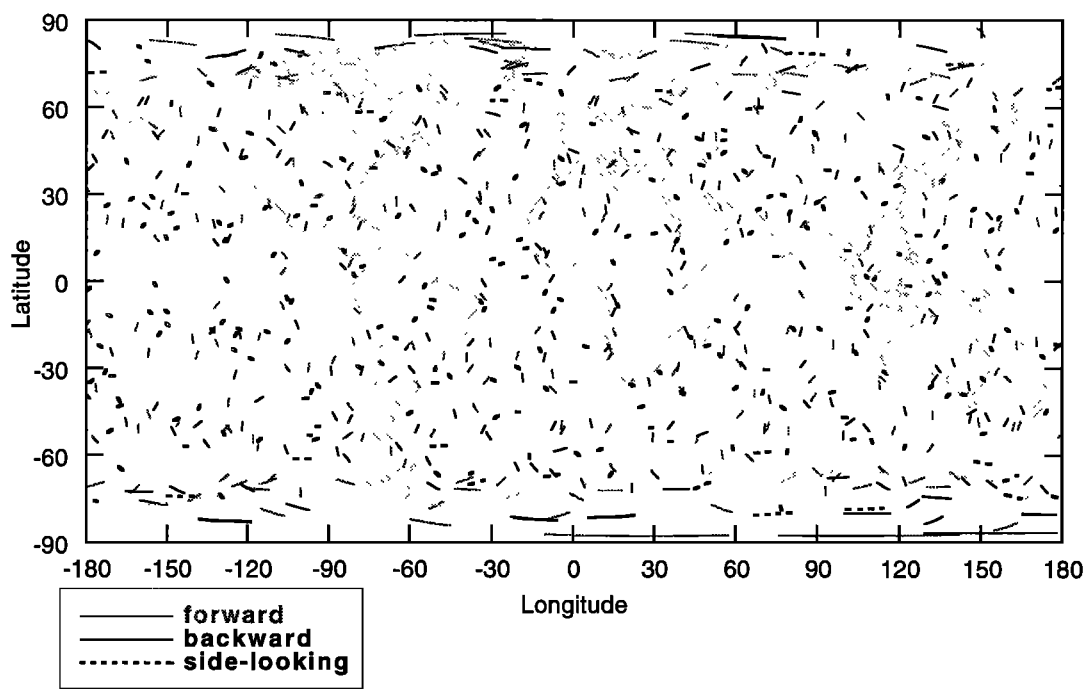

Figure 2. Distribution of occultations observed in 9 day by a polar orbiter at 800 km altitude viewing 24 GPS satellites. Solid lines indicate setting or ingress occultations, thin solid lines are rising or egress occultations, and dashed lines are side-viewing or grazing occultations. Line length is approximately along-track averaging interval (see section 2.5).

The accurate retrieval of atmospheric refractivity profiles depends on accurate estimates of α and a which, in turn, depend on accurate measurements of transmitter signal phase and satellite position and velocity as a function of time. Each GPS satellite continuously transmits right-hand circularly polarized signals at two L band frequencies, 1575.42 MHz (L1) and 1227.6 MHz (L2), corresponding to wavelengths of 19.0 cm and 24.4 cm, respectively. These are modulated at a frequency of 10.23 MHz by a pseudo-random precision ranging code (P code) [*Spilker*, 1978]. The L1 carrier signal is also modulated at a frequency of 1.023 MHz by a coarse/acquisition (C/A) ranging code. In order to make full use of the atmospheric information contained in these signals, a GPS receiver operating in LEO must be able to measure the phase and amplitude of the L1 and L2 carrier signals. Comparison of L1 and L2 phase measurements forms the basis for separating atmospheric and ionospheric contributions to α (section 3.7).

2.2 Atmospheric Bending and Refractive Index Profile Retrieval: Theory

2.2.1 Atmospheric refraction and spherical symmetry. In the geometric optics approximation to the propagation of electromagnetic radiation the path of a ray passing through a region of varying refractive index is determined globally by Fermat's principle of least time and locally by Snell's law. In the most general case, it is not possible to retrieve the three-dimensional variation of index of refraction n from measurements of α as a function of a during an occultation. However, the variation of n along a limb path in the Earth's atmosphere is dominated by the vertical density gradient so that, to the first order, the gradient of n is directed radially and the local refractive index field is spherically symmetrical such that the total refractive bending angle is

$$\alpha(a) = 2\int_{r_t}^{\infty} d\alpha = 2a\int_{r_t}^{\infty} \frac{1}{\sqrt{r^2n^2 - a^2}} \frac{d\ln(n)}{dr} dr \qquad (1)$$

where r is distance from the center of curvature and the integral is over the portion of the atmosphere above r_t. Equation (1), the forward calculation of $\alpha(a)$ given $n(r)$, can be inverted by using an Abelian transformation to express $n(r)$ in terms of α and a [*Fjeldbo et al.*, 1971].

$$n(r) = \mathrm{Exp}\left[\frac{1}{\pi}\int_{a_1}^{\infty} \frac{\alpha}{\sqrt{a^2 - a_1^2}} da\right] \qquad (2)$$

where $a_1 = nr$ is the impact parameter for the ray whose tangent radius is r. Given $\alpha(a)$, (2) can be evaluated numerically.

2.2.2 Departures from spherical symmetry. The derivation of $n(r)$ from $\alpha(a)$ using the Abel transform inversion of (2) is only valid for a spherically symmetrical atmosphere. However, the ellipsoidal shape of the Earth and horizontal gradients in atmospheric structure produce small departures from spherical symmetry in the refractive index field. Furthermore, the ray paths for a given occultation do not generally scan the atmosphere vertically nor are they coplanar. Measurements of $\alpha(a)$ will therefore be affected by tangential refractivity gradients and occultation geometry, and (2) will introduce systematic errors into retrieved profiles of $n(r)$ (section 3.11).

Errors associated with the Abel transform inversion depend on the accuracy with which the spherical symmetry approximation applies locally. First-order errors due to the ellipsoid can be eliminated by selecting a center and radius of curvature appropriate to the latitude and orientation of the occultation measurement. For a given ray path, the majority of atmospheric bending occurs within a horizontal interval of 200-300 km centered on the tangent point (section 2.5). The local spherical symmetry approximation will be accurate for a given occultation provided the horizontal scale of atmospheric structure is greater than this interval and the spread of tangent points lies well within it.

The results of the simulations described in section 3 show that the Abel transform will generally be quite accurate as an initial retrieval scheme for GPS occultations of the Earth's atmosphere. Improved accuracy requires incorporation of known local horizontal structure into the profile retrieval process. Such a scheme has been developed for the special case of elliptical symmetry to invert radio occultation observations of the oblate atmospheric structure of the outer planets [*Lindal*, 1991]. More general approaches are evolving to take advantage of multiple occultations and a priori information [*Gorbunov and Sokolovskiy*, 1993; *Eyre*, 1994; *Hajj et al.*, 1994].

2.2.3 The derivation of $\alpha(a)$ from Doppler shift measurements. As noted in section 2.1, the effect of atmospheric bending on a GPS signal received at a LEO receiver can be measured as an additional Doppler shift relative to that expected for a straight line signal path. Subject to the assumption of local spherical symmetry, Doppler shift can be combined with satellite position and velocity vector measurements to determine $\alpha(a)$. Using the geometry and notation of Figure 1, the Doppler shift f_d in the transmitter frequency f_T, measured at the receiver produced by the projection of the spacecraft velocities onto the ray paths, is given by

$$f_d = \frac{f_T}{c}\left(\mathbf{V_T}\cdot\hat{\mathbf{e}}_T + \mathbf{V_R}\cdot\hat{\mathbf{e}}_R\right) =$$
$$-\frac{f_T}{c}\left(V_T^r \cos\phi_T + V_T^\theta \sin\phi_T + V_R^r \cos\phi_R - V_R^\theta \sin\phi_R\right) \qquad (3)$$

where $\mathbf{V_R}$ and $\mathbf{V_T}$ are receiver and transmitter velocity vectors, $\hat{\mathbf{e}}_R$ and $\hat{\mathbf{e}}_T$ are unit vectors representing the direction of the ray path at the receiver and transmitter, and c is the velocity of light. The RHS of (3) has resolved the velocity vectors into radial (superscript r) and tangential (superscript θ) components, and ϕ_T and ϕ_R are the angles between the ray path and the spacecraft position vector at the transmitter and receiver (Figure 1). In writing (3), the relativistic contributions to the received frequency have been eliminated on the basis of knowledge of orbital geometry and Earth's gravity field.

Under spherical symmetry, Snell's law becomes

$$n\, r \sin\phi = \text{constant} = a = n\, r_t \qquad (4)$$

known as Bouguer's rule (*Born and Wolf*, 1980). As $r \rightarrow \infty$, $n \rightarrow$ unity, so that the constant term in (4) must equal a, the impact parameter, defined in Figure 1. Furthermore, at the ray tangent radius r_t, also defined in Figure 1, $\sin\phi$ = unity so that $a = nr_t$. From Bouguer's rule and the geometry of Figure 1, we have:

$$r_T \sin\phi_T = r_R \sin\phi_R = a \qquad (5)$$

$$\alpha = \phi_T + \phi_R + \theta - \pi \qquad (6)$$

where r_R and r_T are the distances of the receiver and transmitter from the center of curvature, and θ is the angle between the transmitter and the receiver position vectors.

Given measurements of transmitter and receiver position and velocity vectors, transmitter frequency, and Doppler shift, $\alpha(a)$ can be derived iteratively from (3), (5), and (6) by eliminating ϕ_T and ϕ_R. Note that because Bouguer's rule is invoked, this derivation is only exact under the assumption of local spherical symmetry. Errors in α and a due to this assumption

have a small effect on retrieved refractive index profiles compared with the use of the Abel transform inversion and are included in the analysis of section 3.

2.3. Derivation of Atmospheric Properties From Refractive Index Profiles

2.3.1. The dependence of refractive index on atmospheric properties. In order to derive atmospheric properties from retrieved profiles of the real component of atmospheric refractive index n, it is necessary to know how these properties influence n. At microwave wavelengths in the Earth's atmosphere, n contains contributions from four main sources. These are, in order of importance, the dry neutral atmosphere, water vapor, free electrons in the ionosphere, and particulates (primarily liquid water). Their effects are given to first order by

$$N = (n\text{-}1) \times 10^6 = 77.6\frac{P}{T} + 3.73 \times 10^5 \frac{P_w}{T^2} + 4.03 \times 10^7 \frac{n_e}{f^2} + 1.4\,W \qquad (7)$$

where N is refractivity, P is atmospheric pressure in mbar, T is atmospheric temperature in Kelvin, P_w is water vapor partial pressure in mbar, n_e is electron number density per cubic meter, f is transmitter frequency in Hertz, and W is liquid water content in grams per cubic meter. Throughout this paper, the four refractivity terms in (7) are referred to as the dry, moist, ionospheric, and scattering terms.

The dry refractivity term is due to the polarizability of molecules in the atmosphere, i.e., the ability of an incident electric field to induce an electric dipole in the molecules. Dry refractivity is proportional to molecular number density and is dominant below ~60-90 km. The moist refractivity term is due primarily to the large permanent dipole moment of water vapor and becomes significant in the lower troposphere. The form of the dry and moist terms in (7) was given originally by *Smith and Weintraub* [1953], and their accuracy is discussed in section 3.9. The ionospheric term in (7) which is a first-order approximation to the Appleton-Hartree equation [*Papas*, 1965] is mainly due to free electrons in the ionosphere and becomes important above ~60-90 km. The scattering term given in (7) is due to liquid water droplets suspended in the atmosphere. For ice crystals the scale factor is roughly 0.6 rather than 1.4 [*Kursinski*, 1997]. For realistic suspensions of water or ice the scattering term is small in comparison with the other terms and is therefore neglected [Kursinski, 1997].

A representative example of atmospheric bending as a function of ray path tangent height is shown in Figure 3. The first curve is bending due to the vertical refractivity structure of the U.S. Standard Atmosphere. Bending decreases rapidly with tangent altitude, from 1° to 2° near the surface to ~2 x 10^{-5} deg. at 80 km where the bending is roughly equal to the measurement precision. The small size of measurement error relative to bending angle magnitudes in the lower atmosphere demonstrates the extreme precision with which atmospheric delay can be determined.

The second and third curves in Figure 3 include the bending contribution of the ionosphere based on Chapman layer representations of the E- and F-region electron density profiles. The second and third curves include the ionospheric bending under nighttime and daytime conditions, respectively, at the maximum of the solar cycle. Ionospheric bending depends weakly on altitude for tangent altitudes below 80 km because ionospheric refractivity gradients are greatest above 90 km, significantly above the ray path tangent point. Under daytime conditions during the maximum of the solar cycle, ionospheric bending exceeds atmospheric bending above 30 km and therefore must be well calibrated to derive accurate profiles in the middle atmosphere.

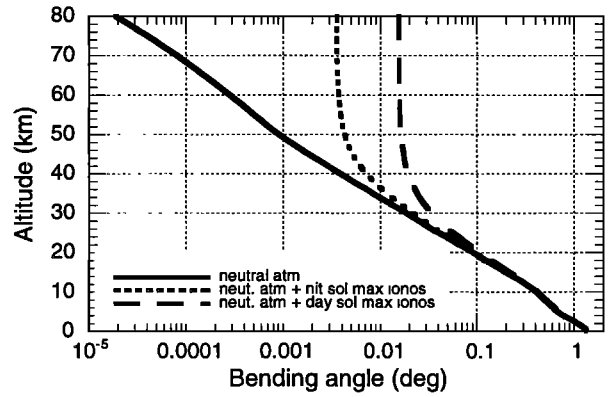

Figure 3. Atmospheric and ionospheric bending for limb ray paths plotted as a function of ray path tangent height. Solid line, bending calculated for U.S. Standard Atmosphere [*Champion et al.*, 1985]. Long-dashed line, bending calculated for U.S. Standard Atmosphere plus typical midlatitude ionosphere during daytime, solar maximum conditions. Short-dashed line, bending calculated for U.S. Standard Atmosphere plus typical midlatitude ionosphere during nighttime, solar maximum conditions.

It is clear from (7) that there is ambiguity between the contributions of the dry, moist, and ionospheric terms to refractivity. Separation and removal of the dispersive ionospheric contribution in (7) using the dual GPS transmitter frequencies L1 and L2 is described in detail in section 3.7.

2.3.2. Derivation of pressure and temperature. After correcting for the ionosphere, only the dry and moist atmospheric contributions to refractivity remain. In regions where the atmosphere is drier than a volume mixing ratio of 10^{-4}, the moist term can be neglected and (7) reduces to N = 77.6 P/T. Combining this with the equation of state (the ideal gas law) gives density as a function of refractivity:

$$\rho(r) = \frac{N(r)\,m}{b_1 R} = \frac{P(r)\,m}{T(r)\,R} \qquad (8)$$

where R is the gas constant, m is the mean molecular mass of dry air, $\rho(r)$ is the air density in kg m^{-3}, and b_1 = 77.6 N-unit K mbar^{-1}. The small effects of nonideal behavior, ignored in (8) for simplicity and clarity, are discussed in section 3.9. In dry air below the homopause (~100 km altitude), m is a known constant, so that pressure can be obtained from density by integrating the equation of hydrostatic equilibrium:

$$\partial P/\partial r = -g\rho \qquad (9)$$

where g is the acceleration due to gravity. The integration is started at a pressure level derived from a temperature guess high in the atmosphere. Initial pressure errors in the temperature guess decrease rapidly as the integration moves deeper into the atmosphere (section 3.10), and accurate temperature profiles can be derived from profiles of ρ and P throughout the stratosphere down to the midtroposphere and below depending on latitude.

The presence of significant tropospheric water vapor complicates the interpretation of refractivity. However, in the colder tropospheric regions, where water vapor concentrations are small, accurate profiles of density, pressure, and temperature can be retrieved, given an estimate of humidity. From (7) and the gas law,

$$\rho = \frac{m}{b_1 R}\left(N - \frac{b_2 P_w}{T^2}\right) \qquad (10)$$

where $b_2 = 3.73 \times 10^5$ K^2 mbar^{-1}, and m is now the mean molecular mass of moist air. Pressure and temperature profiles are derived from the density profile using (9), and the new temperature and mean molecular mass profiles are then used in (10) to update the estimate of ρ. This process is repeated iteratively a few times until the derived temperature profile converges. Water vapor concentration estimates can be obtained from independent observations, weather analyses or climatology. Sensitivities to water vapor uncertainties are characterized in section 3.13.

2.3.3 Derivation of water vapor. Deeper in the troposphere, water vapor concentrations increase contributing up to 30% to net refractivity and can locally dominate the vertical refractivity gradients and bending near the surface in the tropics. Equation (7) can be rearranged to solve for water vapor, so that

$$P_W = \frac{N T^2 - b_1 P T}{b_2} \qquad (11)$$

The recovery of water vapor from measurements of N, using (11), requires knowledge of temperature derived from climatology, independent observations, or weather analyses. The vertical scales of water vapor variability, generally much smaller than that of the dry atmosphere, may also be used to constrain the wet and dry contributions to refractivity. In practice, $T(r)$ is assumed and $P_w(r)$ and $P(r)$ are derived iteratively from (9), (10), and (11).

The accuracy to which lower tropospheric water vapor profiles can be retrieved has been estimated by *Kursinski et al.* [1995]. At low latitudes, humidity derived from individual profiles should be accurate to 20% up to 6 or 7 km altitude and to better than 5% within the convective boundary layer, given independent temperature at accuracies of ~1.5 K presently available from weather analyses. Accuracies decrease at higher latitudes and during winter conditions such that at 45° latitude, 20% accuracy varies from approximately 5 km in the summer to 2-3 km in the winter. The accuracy of averaged water vapor for climatological purposes will depend on climatological temperature accuracy and may be of the order of 3 times better than the accuracy of individual water vapor profiles.

2.4. Atmospheric Attenuation: Signal-to-Noise Performance

In the lower troposphere, increasing pressure and humidity reduce the strength of the occulted signals while increasing their variability, a combination which could limit the altitude range of the occultation coverage. While these problems have, in fact, limited initial GPS-MET coverage in the lower troposphere, they are surmountable with improvements in instrumentation and inversion techniques within the resolution constraints defined in section 2.5. In order to acquire an occulted signal, the signal-to-noise intensity ratio (SNR) at the receiver must exceed a critical value of about 10. If SNR falls below this value, phase lock and the signal are lost. SNR is determined by GPS transmitter power, receiver noise performance, observational geometry, and signal attenuation due to the atmosphere. In the lower troposphere, signal acquisition can be further complicated by atmospheric multipath where several weak occulted signals exist simultaneously. The effects of atmospheric multipath and atmospheric attenuation and the SNR performance expected from a GPS receiver in low Earth orbit are described below.

2.4.1. Atmospheric attenuation. The attenuation mechanisms affecting propagation of GPS signals across the atmospheric limb are absorption by atmospheric constituents, extinction by particle scattering, and defocusing. Atmospheric absorption at L band wavelengths is dominated by the far wings of pressure-broadened molecular oxygen which reduces GPS signal intensities by a factor of 2 for a limb path with a tangent height near the surface based on spectra from *Chahine et al.* [1983]. Extinction caused by realistic suspensions of water droplets or ice particles in the atmosphere is negligible at L band wavelengths [*Kursinski*, 1997].

The dominant attenuation mechanism is defocusing, which occurs when rapidly changing vertical refractivity gradients cause adjacent, nearly parallel rays entering the atmosphere to bend differentially and diverge, reducing (or sometimes enhancing) signal intensity at the receiver. The intensity of an occulted signal after defocusing can be represented by the approximate expression [*Haugstad*, 1978]

$$I = I_0 M, \text{ where } M = (1 + D\,\partial\alpha/\partial a)^{-1} \approx (1 - D\alpha/H_\alpha)^{-1}, \qquad (12)$$

I is the observed signal intensity, I_0 is the signal intensity observed in the absence of defocusing, D is the distance from the receiver to the limb, α is bending angle, and a is the impact parameter (see Figure 1). H_α is the local bending angle scale height defined by the approximation $\alpha = \alpha_0 e^{-(a-a_0)/H_\alpha}$, where $a \approx a_0$. The variation of the defocusing factor M with limb ray path tangent altitude, calculated for a vertical refractivity profile corresponding to a radiosonde ascent from Hilo, Hawaii, in July 1991, assuming spherical symmetry, is illustrated in Figure 4a. Three general features of the curve should be noted. Firstly, a gradual, overall reduction in M with decreasing altitude is caused by the exponential increase of bending angle with decreasing altitude (Figure 3, (12)). Secondly, rapid vertical variations in M are associated with sharp vertical changes in the refractivity gradient caused primarily by vertical water vapor mixing ratio fluctuations. These variations provide a sensitive measure of the local refractivity scale height and humidity fluctuations. Finally, signals with ray path tangent heights that fall within certain vertical intervals are attenuated completely. In Figure 4a, attenuation is complete at the top of the marine boundary layer near 3.8 km associated with the transition between the boundary layer and the overlying atmosphere.

Complete attenuation occurs at ray path tangent altitudes where the vertical refractivity gradient becomes so large that the radius of curvature of the ray is smaller than the radius of curvature of the atmosphere, causing the ray to curve down into the surface. This happens when the refractivity gradient dN/dr $\leq -10^6/R_c$, where R_c is the radius of curvature of the atmosphere; for a mean value of R_c, $dN/dr \sim -0.16$ N-units m^{-1}. Of the vertical gradients in pressure, temperature, and water vapor contributing to dN/dr via (7), only the water vapor gradient is capable of producing critical gradients. Under conditions representative of the top of the marine boundary layer, water vapor partial pressure gradients of ≤ -34 mbar km^{-1} will produce critical gradients. During the 1969 Atlantic Trade wind Experiment (ATEX), the transition at the boundary layer top was ~200 thick on average with mean changes in temperature and water vapor partial pressure across the region of 5 K and 6 mbar [*Augstein et al.*, 1974]. The resulting contributions to dN/dr by the average temperature and moisture gradients are about -0.03 N-units m^{-1} and -0.12 N-units m^{-1}, respectively. While the temperature contribution is small, the mean water vapor gradient is 75% of the critical value, indicating a significant fraction of occultations will experience critical refraction in regions where a sharp inversion caps the marine boundary layer.

The vertical extent of the critical refraction interval is derived from Bouguer's rule. In order for a ray to leave the atmosphere, ϕ in (4) must be less than or equal to $\pi/2$ away from the tangent point, such that $nr \geq n_t r_t$ where the subscript "t" refers to the ray path tangent where ϕ is $\pi/2$. It follows that $r_1 n_1 = r_0 n_0$ where the indices 1 and 0 refer to the tangent points of the extreme ray paths, respectively, at the top and bottom of the interval of complete attenuation. The vertical extent of the

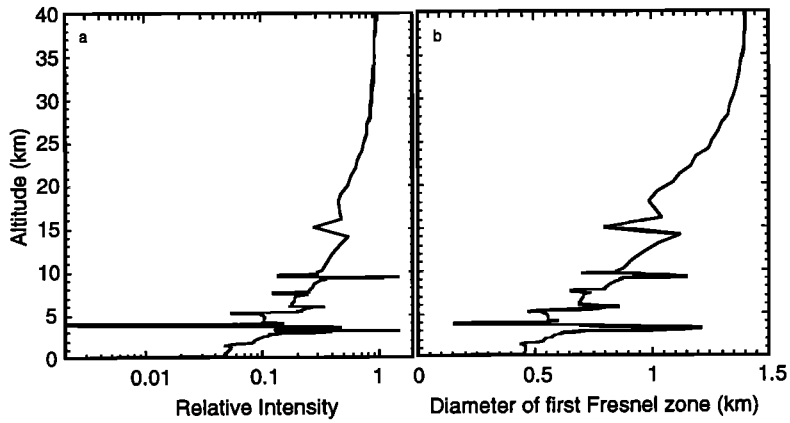

Figure 4. (a) Variation of defocusing factor M with altitude (equation (12)). (b) The diameter of the first Fresnel zone defined by (14) and (15) plotted as a function of ray path tangent height. Both M and diameter of the first Fresnel zone are calculated for a refractivity profile derived from radiosonde temperature and humidity profiles, assuming spherical symmetry. Radiosonde ascent 1200 UT, July 11, 1991, Hilo, Hawaii.

interval is given by

$$\Delta r = r_1 - r_0 = r_1 (1 - n_1/n_0) = r_1 \Delta n / n_1 \approx r_1 \Delta n,$$

where $\Delta n = n_0 - n_1$. The large change in index of refraction Δn occurs primarily across the boundary layer transition region which has a vertical extent Δz. Therefore

$$\Delta r \approx r_1 (dn/dz)_{tr} \Delta z = r_1 \eta / R_c \Delta z \approx \eta \Delta z$$

where η is the ratio between the large index of refraction gradient across the transition region $(dn/dz)_{tr}$ and the critical index of refraction gradient $1/R_C$. The vertical interval of critical refraction therefore depends on both the magnitude and the vertical extent of the large refractivity gradient. As an example, an extremely large vertical moisture gradient observed by a radiosonde over Hilo, Hawaii (October 1, 1993 0000 UT) exceeded the critical gradient by a factor of 3 over a vertical interval $\Delta z \sim 80$ m such that an occultation of this region would have observed a vertical interval of critical refraction 240 m in extent.

Accurate recovery of refractivity structure below the critical refraction interval using the Abel transform requires that the existence of the singularity in the $\alpha(a)$ profile due to the infinite bending angle at the critical refraction interval be identified and that the numerical implementation of the Abel transform integrate across the singularity. Structure within the interval must be derived via interpolation. Errors in derived refractivity below the interval due to an imperfect representation of the singularity will be greatest at the bottom edge of the critical refraction interval and will decrease rapidly at lower altitudes. Because of the singularity, ray tracing inversion schemes may prove better suited for recovering vertical stucture under these conditions. This is presently an area of research.

The prototype GPS-MET receiver typically tracks to 5 km altitude or lower, which indicates that critical refractivity gradients extending over sufficiently large vertical and horizontal scales to extinguish occulted GPS signals must be at or below 5 km altitude. Given the low SNR of the receiver, it is likely that critical refraction regions lie still lower in altitude probably associated with the extreme gradients of capping inversions marking the transition between the boundary layer and the free troposphere at the trade wind inversion. Critical refraction is therefore probably limited to within 4 km (and more typically 2 km) of the surface at low latitudes and lower altitudes at higher latitudes. Any degradation in accuracy associated with these extreme gradients beyond the accuracy expectations summarized in section 3.14 will be limited to the altitude interval within a few kilometers of the surface.

2.4.2 Atmospheric multipath. Atmospheric multipath occurs when an interval of high refractivity gradient overlies a region of lower gradients resulting in more than one signal path between the transmitter and the receiver. It is generally produced by water layers and is therefore more frequent at lower latitudes. From the standpoint of retrieving vertical refractivity profiles, each of the multiple signal paths has a unique tangent height and therefore samples a unique value of a in the α versus a profile. Therefore the receiver must be capable of acquiring each of the multiple signals to enable recovery of the complete $\alpha(a)$ profile for the Abel transform (equation (2)). Given that its design is minimally modified from a ground-based receiver, the prototype GPS-MET receiver does not fair well in the presence of atmospheric multipath because of the problems the weak and interfering multiple signals pose for the phase-locked loop. Improvements in signal tracking, enabling recovery of multiple signals consistent with the attenuation discussion below, are under development at JPL and will be incorporated in several receivers launching over the next 3 years.

2.4.3 Signal-to-noise performance. The GPS network transmits relatively powerful signals designed for simple, hand-held receivers. In the absence of atmospheric attenuation the prototype GPS-MET receiver with a small hemispherical field-of-view antenna in low Earth orbit has obtained SNRs of ~1-2 x 10^3 over the 20 ms integration period used at present for the radio occultation observations. Future instrumentation will improve upon this SNR by perhaps an order of magnitude.

Allowing for the molecular oxygen attenuation factor of 2 near the surface and the SNR of 10 required for receiver phase lock, attenuation by a factor of at least 100 (20 dB) in intensity due to atmospheric defocusing can be tolerated before loss of signal occurs. This margin is sufficient for signals to be tracked throughout the atmosphere with the exception of regions of very sharp refractivity gradients (Figure 4a). GPS signal paths will in fact probe the entire atmosphere apart from occasional small critical refraction intervals just discussed. Implications of SNR on the accuracy of derived refractivity, pressure, and temperature are discussed in section 3.3.

Encryption of GPS signals for military purposes is another issue. Two types of encryption exist: selective availability (SA), which alters the apparent GPS satellite positions, and anti-spoofing (AS), which eliminates jamming of the GPS receivers by false signals. Methods for eliminating SA are dis-

cussed in section 3.8. The AS encryption affects the L1 and L2 P-code signals (section 2.1) and therefore calibration of the ionosphere (section 3.7). A classified receiver which has knowledge of the encryption code can recover the full precision of the signal. An alternative method is a nonclassified cross-correlation approach which produces little degradation when SNRsare high (section 3.3). Unfortunately, the SNR of the cross-correlated signal decreases as the square of the atmospheric attenuation such that the factor of 40 attenuation due to molecular oxygen absorption and defocusing near the surface (Figure 4a) will decrease the SNR of the cross-correlated signal by 1600 (32 dB). The integration time used when the ray path tangent point is in the lower troposphere is of the order of 1 to 2 s as defined by the time for the ray path to descend or ascend a Fresnel diameter (section 2.5, Figure 19). Therefore given the SNR of 10, the cross-correlated signal should have a 1 s SNR of 42 dB or greater in the absence of the atmosphere. While cross-correlation SNRs of the prototype GPS-MET instrumentation are not this high, future instrumentation will produce 1 s cross-correlation SNRs of the order of 47 dB, indicating the ionosphere calibration can be maintained through most of the troposphere with unclassified instrumentation. Since errors due to incomplete calibration of the ionosphere are generally negligible in the lower troposphere (sections 3.7 and 3.14), interpolation or extrapolation of the ionosphere calibration across the short vertical intervals in the troposphere, where attenuation is too large to maintain cross-correlation tracking, should have negligible impact on retrieval accuracy.

2.5 Spatial Resolution

2.5.1 Limits to vertical and horizontal resolution. This section considers the fundamental limits to the spatial resolution of atmospheric profiles retrieved from GPS radio occultation measurements. The vertical resolution of a single, instantaneous bending measurement is determined by the contribution of individual atmospheric layers to net bending along the ray path (equation (1)). Better vertical resolution can be retrieved from a profile of closely separated measurements, subject to limits imposed by diffraction. For the limb-sounding geometry appropriate to GPS radio occultation, horizontal resolution may be defined by the distance traversed by the radio path as it enters and exits a layer having a vertical resolution of ΔZ; in this case, the horizontal and vertical resolution are related by the approximate expression

$$\Delta L = 2(2R\Delta Z)^{1/2} \tag{13}$$

where ΔL is horizontal resolution, ΔZ is vertical resolution, and R is the radius of the atmosphere at the ray path tangent height.

The vertical resolution expected from GPS radio occultation measurements is described below, and the possibility of improving on the limits imposed by diffraction is discussed. The section concludes by noting the need for measurements such as the radio occultations with spatial resolution compatible with the vertical and horizontal scales of characteristic atmospheric structure.

2.5.2 Vertical resolution: individual measurements of bending angle. The variation of the vertical resolution of an individual bending angle measurement (one in a sequence of measurements taken during an occultation) is illustrated in Figure 5 as a function of ray path tangent altitude for the atmospheric profile used in Figure 4a. The curves on the right show the relative contribution of each altitude interval to net atmospheric bending for several tangent altitudes. These contribution functions are strongly peaked at the tangent altitude due to the limb-sounding geometry and exponential variation of refractivity with altitude (equation (1)). Vertical resolution, defined as the vertical interval above the tangent height contributing 50% to net bending, is plotted as a function of tangent altitude in the left-hand side of Figure 5. For the atmospheric profile used in Figure 5, the 50% bending interval varies from 0.5 to 2.0 km corresponding via (13) to a 50% horizontal interval from 160 to 320 km. The smallest 50% interval occurs at ray path tangent altitudes near 3.8 km where large vertical refractivity gradients associated with rapid

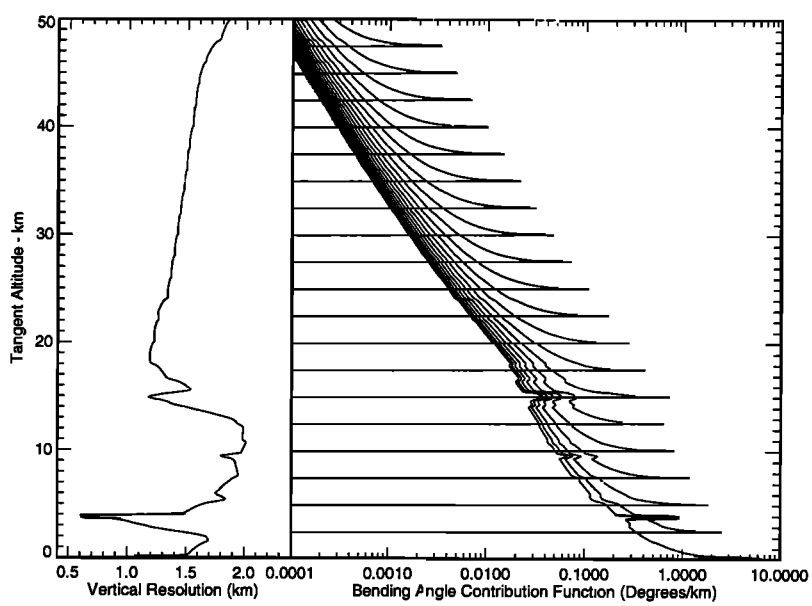

Figure 5. Bending contribution functions on the right and vertical resolution profile on the left for individual radio occultation bending angle measurements plotted as a function of altitude. Resolution is defined here as the vertical interval between the ray path tangent height and the height at which half of the total bending has been accumulated. These curves are calculated for a refractivity profile derived from radiosonde temperature and humidity profiles, assuming spherical symmetry. Radiosonde 1200 UT, July 11, 1991, Hilo, Hawaii.

changes in humidity across the top of the boundary layer concentrate the bending, causing vertical resolution to improve in a region where it is needed most.

Although the vertical resolution of single occultation measurements is described well by Figure 5, the vertical resolution of refractivity profiles retrieved from GPS radio occultation profiles can be significantly better, given profiles of closely spaced bending angle measurements, high measurement precision, and an inversion scheme that correctly represents the contribution of different levels to bending angle. All of these conditions are met for GPS occultations measured by a LEO satellite, provided the atmosphere is locally spherical in structure so that the Abel transform inversion of (1) can be used. Under these conditions, the ultimate limits to vertical and horizontal resolution of retrieved profiles are set by diffraction.

2.5.3 Vertical resolution: diffraction limit. The theory of section 2.2 assumes that transmitter signals follow a dimensionless ray path to the receiver. This is the path of minimum phase delay relative to the delay associated with neighboring, physically realizable paths. However, a geometrical ray path is an approximation to Fresnel diffraction as wavelength approaches zero. Because signals originate at a point source and are detected by a receiver phase-locked to the minimum phase delay, the cross-beam sampling at the limb takes the form of concentric Fresnel zones of a positive and negative response centered on the ray path. The contributions of adjacent Fresnel zones cancel so that the effective sampling can be represented by the first Fresnel zone [*Born and Wolf*, 1980].

In the absence of significant atmospheric bending, the diameter of the first Fresnel zone Z_F at the ray path tangent level is given by

$$Z_F = 2\,[\lambda L_T L_R / (L_T + L_R)]^{1/2}$$
$$\approx 2\,[\lambda L_R]^{1/2} \quad (\text{If } L_T >> L_R) \tag{14}$$

where λ is the GPS signal wavelength, and L_T and L_R are the distance from the transmitter and receiver to the limb respectively. L_T is approximately 28,500 km for the GPS transmitters and, for a receiver in a 700 km altitude orbit, L_R is about 3100 km. At the GPS L1 wavelength of 19 cm, (14) yields a value for Z_F of 1.4 km. From (13) the horizontal resolution corresponding to a vertical resolution of 1.4 km is about 270 km.

Diffraction-limited vertical resolution is also influenced by the vertical refractivity gradient. When this gradient increases, the vertical diameter of the first Fresnel zone decreases and vertical resolution improves in accordance with the expression

$$Z_F = Z_F(\text{free space})\; M^{1/2} \tag{15}$$

where M is defined in (12) [*Fjeldbo and Eshleman*, 1969]. The variation of M with altitude for the temperature and humidity profiles acquired during a radiosonde ascent from Hilo, Hawaii, in July 1991 is shown in Figure 4a, and the altitude dependence of Z_F, derived from (15), is displayed in Figure 4b. The gradual decrease in Z_F from 1.4 km in the stratosphere to less than 0.5 km near the surface is due to the exponential increase of refractivity gradient with decreasing altitude. Within the troposphere, rapid variations in Z_F are due primarily to sharp changes in vertical refractivity gradient caused by changes in humidity. This effect is particularly strong within a few hundred meters of the surface and at the top of the boundary layer near 3.8 km, where diffraction-limited vertical resolution lies in the 100 to 200 m range.

From the examples given above, it is clear that diffraction-limited vertical resolution of GPS radio occultation measurements is comparable to or better than the vertical resolution imposed by atmospheric structure on a single bending angle measurement. Furthermore, vertical resolution is best in the troposphere and in regions with large vertical refractivity gradients where it is most needed. The diffraction limited horizontal resolution of occultation measurements in the cross-beam direction is approximately 1.4 km at all levels, because horizontal refractivity gradients are generally small.

2.5.4 Improved vertical resolution. Vertical resolution superior to that imposed by Fresnel diffraction may be possible. Atmospheric structures smaller than the Fresnel scale produce diffraction patterns in the signal measured by the receiver, known as phase and amplitude scintillations. Because occulted signals are monochromatic with well defined phase, scintillation measurements obtained during an occultation can, in principle, be inverted to remove the effects of diffraction and reconstruct vertical profiles at resolutions finer than the Fresnel scale, provided atmospheric structure varies primarily in the vertical rather than horizontal direction such that the one dimensional (1-D) diffraction pattern acquired in the occultation recovers sufficient information to allow an inversion.

Techniques for inverting and removing the effects of diffraction in Voyager occultation observations of the Saturnian and Uranian ring systems were developed by researchers at Stanford University which dramatically improved radial resolution relative to diffraction-limited scales [*Marouf et al.*, 1986]. The removal of diffraction effects within an atmosphere is more complicated because the atmosphere is a three-dimensional structure. The idea has been extended to atmospheres, using the thin phase screen approximation, to detect and characterize planetary waves in the Uranian stratosphere [*Hinson and Magalhaes*, 1991]. Development of a Fourier optics approach to account for and remove the effects of diffraction from observations of thin atmospheres is under development [*Karayel and Hinson*, 1997]. Another idea is to "back propagate" the signal from the actual reception location to a location closer to the Earth's limb [*Gorbunov et al.*, 1996; *Gorbunov and Gurvich*, 1997] which reduces the Fresnel zone size and improves vertical resolution. Lowering the reception altitude from 700 km to 100 km (~the height of layers in the E region of the ionosphere) via back propagation would improve vertical resolution by 40%. If the altitude could be reduced to 30 km, vertical resolution would increase by a factor of 2.2, improving near-surface resolution to ~200 m (Figure 4b), a significant increase given the small vertical extent of the boundary layer.

2.5.5. The importance of consistent vertical and horizontal resolution. From (13) the ratio of horizontal to vertical resolution for GPS radio occultation measurements is approximately $\Delta L/\Delta Z \sim 2(2R/\Delta Z)^{1/2}$, and ranges from 190 when ΔZ = 1.4 km to 700 when ΔZ = 0.1 km, with typical tropospheric values near 270. These magnitudes are similar to the ratio of consistent horizontal and vertical resolution discussed by *Lindzen and Fox-Rabinowitz* [1989] for quasi-geostrophic flow and internal gravity waves and to that of regional and global atmospheric models. For quasi-geostrophic flow the ratio is the Rossby ratio between vertical and horizontal scales given by the expression

$$\Delta L/\Delta Z = N_B/f_o \tag{16}$$

where f_o is the Coriolis parameter and N_B is the Brunt-Väisälä frequency. The similarity between the GPS values and those derived from (16) demonstrates that the relationship between vertical and horizontal resolution for GPS radio occultation measurements is consistent with most atmospheric structure and that occultation measurements are well suited for assimilation into regional and global weather prediction models. Further, the ability to routinely probe the troposphere in a limb-sounding geometry complements the high horizontal resolu-

tion but more limited vertical resolution of nadir-viewing observations.

3. Refractivity Profile Inversion: Sources of Error and Expected Accuracy

3.1. Introduction

In this section, the accuracy with which refractivity, density, pressure, and temperature can be derived from occultation observations is discussed and assessed. The section is structured as follows. Section 3.2 begins with a general overview of error propagation through the profile retrieval process working sequentially through derivations of refractivity, density, pressure, and temperature. The overview is followed by a sequence of subsections briefly describing each of the errors identified below. Using the approach described in section 3.2, the impact of each error on derived refractivity, pressure, and temperature is characterized. When possible, analytic methods are used. Finally, the individual error contributions are drawn together into an overall, vertical accuracy budget for refractivity, density, pressure, and temperature which also defines the limiting sources of error. A reader primarily interested in the error summary may wish to move immediately to section 3.14.

Individual error sources can be grouped into three categories: measurement errors, calibration errors and retrieval errors. The more significant sources are summarized below and are discussed in this order in the rest of this section. The measurement errors include signal to noise ratio performance, clock instability, local multipath; calibration errors include residual ionospheric effects, orbit determination accuracy differencing schemes to remove clock error; and retrieval errors include refractivity constant uncertainties, uncertainties in Abel and hydrostatic integral boundary conditions, horizontal refractivity structure, geometrical optics approximation, and water vapor/density ambiguity.

3.2. Error Propagation Through GPS Profile Retrievals

To characterize the individual sources of error which follow, a general description of the propagation of errors through the retrieval process is needed. For errors related to the phase observations, the first step is to determine the response of the transformation from measured atmospheric phase delay to refractivity to a single phase perturbation. This impulse response includes the sequential conversion from phase to frequency, then bending angle, and finally, refractivity (via the Abel transform). Knowledge of the impulse response allows a complete description of the impact of phase measurement errors on refractivity as well as density, which is proportional to refractivity in the absence of significant water vapor. The second step describes the transformation of refractivity errors into errors in pressure through the hydrostatic integral. The third step describes how errors in refractivity and pressure combine to produce temperature errors via the ideal gas law.

3.2.1. Impact of phase error on refractivity. Imperfect phase measurements degrade derived refractivity accuracy. Derivation of refractivity from measurements of phase can be divided into three steps: (1) phase is differentiated to produce frequency; (2) frequency is transformed into bending angle; and (3) bending angle is converted into refractivity via the Abel integral. These steps are linear, at least at the error magnitudes discussed in this section, and the error in refractivity due to errors in phase can therefore be described using linear system theory as [*Papoulis*, 1984]

$$\delta N(t) = \delta\phi(t) \otimes h_D(t) \otimes h_A(t) \qquad (17)$$

where δN and $\delta\phi$ are refractivity and phase errors, h_D is the impulse response of the differentiation step, h_A is the impulse response of the combined second (frequency to bending angle) and third (Abel transform) steps and circled times signifies convolution. Describing the transformation of noise in terms of an impulse response also allows the refractivity retrieval process to be characterized in the Fourier domain, described by *Kursinski* [1997] which will be used in sections 3.4 and 3.5 to describe the effects of clock instability and local multipath error.

The impulse response of the differentiator depends on the particular numerical implementation chosen. For simplicity, a simple discrete differentiator which differences consecutive phase samples is used here:

$$h_D(t) = \frac{\delta(t+\frac{\tau}{2}) - \delta(t-\frac{\tau}{2})}{\tau} \qquad (18)$$

where $\delta(t)$ represents the Dirac delta function, and t is the time interval between phase measurements, which is set to the time required for the ray path to cross the diameter of the first Fresnel zone, the practical resolution limit in the geometric optics approximation (14). The impulse response $h_A(t)$ will be characterized numerically by inputting a set of Doppler frequencies containing a single-frequency error into the bending angle and Abel transformation steps. Integration of the Abel transform requires numerical integration, the details of which affect response to errors. The specific implementation used here approximates a continuous representation of $\alpha(a)$ for the Abel integration by fitting a cubic polynomial to $\ln(\alpha)$ as a function of a where the natural logarithm is used because, to first order, the dependence of bending angle on miss distance is exponential. Figure 6 shows the response of the Abel transform to a single 1 mm s^{-1} error equivalent to a frequency error of 5×10^{-3} Hz for a radio wavelength of 20 cm. The response includes errors in derived radius and height.

From (18), it is clear that a single-phase error produces a double pulsed frequency error which, when convolved with h_A, produces the vertically focused refractivity error shown in Figure 7, defining the refractivity error response to phase error. The altitude of the largest refractivity error in Figure 7 occurs at the altitude of the first of the two frequency peaks. The second frequency pulse cancels much of the remaining contribution of the convolution of h_A with the first frequency pulse.

3.2.2. Relationship between height and time. Because phase noise is a typically a function of time, (17) re-

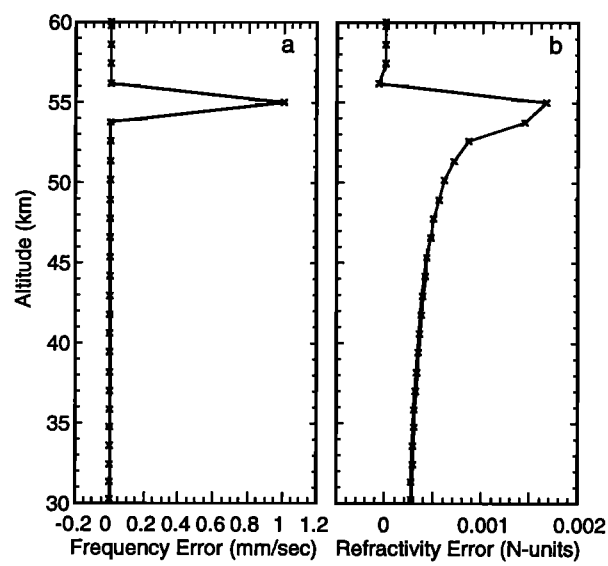

Figure 6. (a) Single frequency measurement error. (b) Refractivity error response to frequency error in Figure 6a.

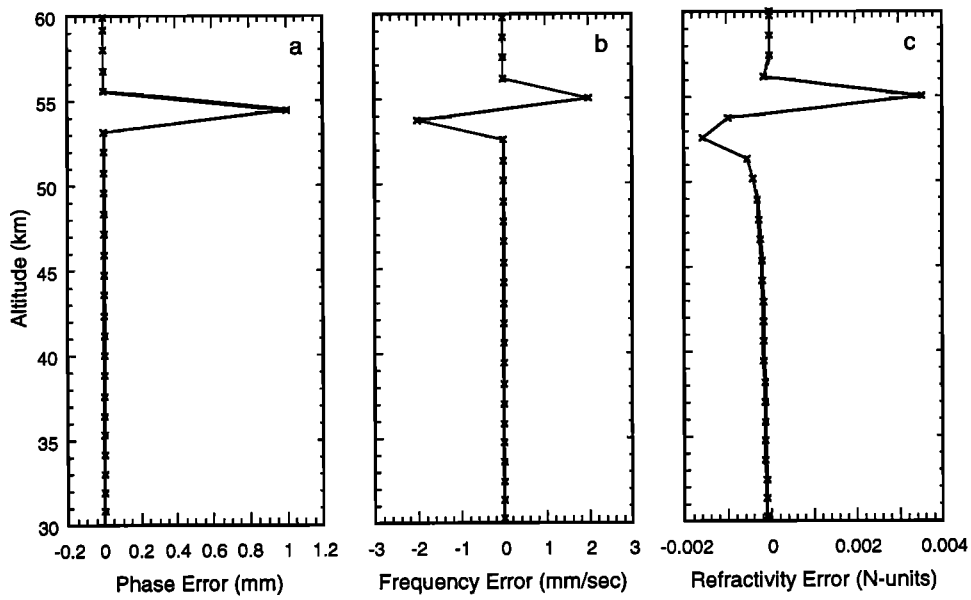

Figure 7. (a) Single phase error. (b) Frequency error resulting from Figure 7a. (c) Refractivity error response to frequency error in Figure 7b.

lates measurement error to refractivity error as a function of time, whereas atmospheric refractivity is a function of height to first approximation. Time and height are related by the rate at which the ray path tangent height descends (or ascends in a rising occultation) through the atmosphere. At altitudes near the tropopause and above, where bending is not too large, this rate is roughly $V_\perp$, the component of the LEO orbital velocity orthogonal to the limb, typically between 2 and 3 km s^{-1}. For consideration of measurement noise the region most affected is the stratosphere because, as will be shown, sources of error other than measurement noise dominate in the lower stratosphere and below.

3.2.3 Scaling the impulse response to shorter and longer integration times. Frequency error is proportional to phase error divided by the phase estimation time interval τ_{est} so refractivity error must be proportional to τ_{est}^{-1}. Since vertical resolution is also tied to τ_{est}, an improvement in refractivity error will come at the expense of vertical resolution. Of the various sources of error, thermal noise, described in section 3.3, exhibits the greatest sensitivity to τ_{est}. For thermal noise, rms phase error is proportional to $\tau_{est}^{-1/2}$, and frequency and therefore refractivity error scale in proportion to $\tau_{est}^{-3/2}$. The $\tau_{est}^{3/2}$ scaling can be used at high altitudes where thermal noise can dominate other sources of error in a trade-off of resolution for accuracy. For instance, increasing τ_{est} by a factor of two will reduce the resolution by the same factor of two but reduce thermal error by a factor of 2.8, which is equivalent to raising the altitude at which a level of accuracy is achieved by a scale height.

The magnitude of the discrete frequency error impulse response $h_A(t)$ is proportional to the sampling interval because the frequency error is not a true delta function due to the finite width of the input error pulse. The numerical implementation of the Abel integral interpolates between the samples, and the actual error in the Abel transform is somewhat triangular in shape where the width at the midheight of the triangle is the time interval between samples fed into the Abel integral. Therefore when the interval separating the discrete values which make up the impulse response is changed, the magnitude of each of the discrete values scales as the square root of the ratio of the new and original intervals.

3.2.4 Effect of Errors in Refractivity on Density and Pressure. Under dry conditions, density is proportional to refractivity via (8), and so density errors are proportional to refractivity errors and their fractional errors are equal. The effect of water vapor on retrievals of density, pressure, and temperature becomes important in the warm regions of the troposphere, as is described in section 3.13. In the extremely dry air found in the cold (< 250 K) regions of the troposphere and stratosphere, where density is directly proportional to refractivity, pressure is derived from density via the hydrostatic integral

$$P(z) = P(z_u) + \int_z^{z_u} g\,\rho\,dz'$$

where z_u is the height at which the integral is initiated and $P(z_u)$ is the pressure at that height. The choice of z_u is discussed in section 3.10 based upon a trade-off between noise characteristics described later. The fractional pressure error is then

$$\frac{\delta P(z)}{P(z)} = \frac{\delta P(z_u)}{P(z)} + \frac{\int_z^{z_u} g\,\delta\rho(z')\,dz'}{P(z)} \tag{19}$$

The contribution to the fractional pressure error at z by the error in the initial guess of pressure at z_u, $\delta P(z_u)$, decreases exponentially as z decreases. As temperature is less variable than pressure at middle atmospheric heights, $P(z_u)$ is probably best estimated from estimates of $T(z_u)$ and $\rho(z_u)$ with $T(z_u)$ estimated from a combination of climatology, models, and other observations and $\rho(z_u)$ derived directly from the occultation observations themselves. The pressure error can be written as

$$\frac{\delta P(z)}{P(z)} = \left(\frac{\delta T(z_u)}{T(z_u)} + \frac{\delta\rho(z_u)}{\rho(z_u)}\right)\frac{P(z_u)}{P(z)} + \frac{\int_z^{z_u} g\,\delta\rho(z')\,dz'}{P(z)} \tag{20}$$

3.2.5. Effects of Refractivity Errors on Geopotential Height. Atmospheric fluid dynamics equations are generally written with pressure rather than altitude as

the vertical coordinate such that the geopotential associated with a pressure level becomes a dependent variable of fundamental interest. Since the change in pressure with height is defined via the hydrostatic and ideal gas law as

$$\frac{\delta P}{P} = -\frac{m\,g}{R\,T}\,\delta z$$

errors in pressure height δz and geopotential $\delta\Phi$ are related to the fractional pressure error as follows

$$\frac{\delta P}{P} = -\frac{\delta z}{H} = -\frac{\delta\Phi}{g\,H} \tag{21}$$

Therefore the approximate geopotential height error can be found by multiplying the fractional pressure error at any derived pressure level by the local pressure scale height.

3.2.6. Effect of Density and Pressure Errors on Temperature. Temperature is derived via the ideal gas law $T = P/(R\rho)$, and fractional temperature error is therefore related to fractional errors in density and pressure by

$$\frac{\delta T}{T} = \frac{\delta P}{P} - \frac{\delta\rho}{\rho} \tag{22}$$

The fractional mean square error in temperature is given by

$$\left\langle\left(\frac{\delta T}{T}\right)^2\right\rangle = \left\langle\left(\frac{\delta P}{P}\right)^2\right\rangle + \left\langle\left(\frac{\delta\rho}{\rho}\right)^2\right\rangle - 2\left\langle\frac{\delta\rho}{\rho}\,\frac{\delta P}{P}\right\rangle \tag{23}$$

The magnitude of the temperature error therefore depends on the vertical correlation of the density error. If the density error correlation length is small such that density error varies rapidly relative to a scale height, its integrated effect in the pressure error (equation (19)) is small, causing the rapid density errors to map almost directly into temperature errors. When density errors vary slowly relative to a scale height, the fractional pressure error will be greater than the fractional density error, and the pressure error contribution to temperature error will dominate. When the density error correlation length is roughly a scale height, fractional density and pressure errors will be comparable, and the fractional temperature error will be smaller than either of them. Note that when density error systematically increases as $(z_u\text{-}z)^n$, the temperature error will pass through zero at a height, n scale heights below z_u, marking the transition between the density error dominated region above and the pressure error dominated region below.

3.3. Thermal Noise

The finite GPS signal strength and the receiver amplifier noise combine to produce a random phase error, referred to as thermal error, which is independent from sample to sample. Because thermal errors vary rapidly with height, they contribute significantly to refractivity and temperature error at high altitudes but produce little pressure error.

The mean square error of thermal phase noise is given by

$$\left\langle\delta\phi(\tau)^2\right\rangle^{1/2} = \frac{\lambda\,\sigma_n(\tau)}{2\pi A} = \frac{\lambda}{2\pi}\left(2\,SNR_0\,\tau\right)^{-1/2}$$

where $<\delta\phi^2>^{1/2}$ is rms phase error in units of length, τ is the integration time in seconds, λ is the GPS signal wavelength, A is the signal amplitude, σ_n is the root-mean-square (rms) of the thermal noise, and SNR_0 is the signal-to-noise ratio for an integration time of 1 s. The signal strength is determined by GPS transmitted power, antenna gain, and the atmospheric attenuation mechanisms discussed in section 2.4; σ_n is determined by the receiver amplifier and blackbody radiation received from the Earth. Table 1 shows the SNRs and rms thermal phase errors representative of the prototype GPS-MET and future receiving systems. Using future generation LEO receiver hardware, the rms phase measurement errors will be ~0.05 mm for an integration time of 0.5 s, the approximate time for a ray path tangent point to descend a Fresnel diameter Z_F in the middle atmosphere. Subsequent amplification of the phase error by a factor of 3 due to ionosphere calibration (section 3.7) and 2 due to clock double-differencing (section 3.8) yields a calibrated rms phase error of ~0.3 mm in 0.5 s for the GPS receiver being developed within JPL. When the AS encryption is on (section 2.4), use of an unclassified receiver with a small receiving antenna will roughly double the thermal error (column 3, Table 1).

3.3.1. Refractivity Error. Using the impulse response described in section 3.2 (equation (17)), the refractivity noise variance due to thermal noise is

$$\left\langle\delta N_i^2\right\rangle = \left\langle\left(\sum_{j=1}^{j\,max}\delta\phi_j\,h_{DA_{i-j}}\right)^2\right\rangle = \left\langle\delta\phi^2\right\rangle\sum_{j=1}^{j\,max}h_{DA_{i-j}}^2 \tag{24}$$

where j is the sample number counted from the first sample used in the Abel transform and $j_{max} = (z_a\text{-}z)/Z_F$ where z_a is the height at which the Abel transform is initiated. The second step of (24) can be made because the sample-to-sample correlation is zero and $<\delta\phi^2>$ is independent of altitude at least for ray paths at or above the tropopause where thermal noise can be a significant contributor to refractivity error. More than 95% of the total variance of the impulse response given in Figure 7 is contributed by the phase error in the measurement made at the altitude of the refractivity retrieval such that the impact of white phase noise on derived refractivity is quite focused vertically. The rms refractivity error of (24) is also independent of altitude. An rms refractivity error of 0.0012 N-units produced by an rms phase error of 0.3 mm in 0.5 s corresponds to fractional refractivity errors of ~0.6% and 2% at 50 and 60 km altitude depending on latitude and season which are significant at high altitudes.

3.3.2. Pressure Errors. Given a sequence of independent refractivity errors, the pressure error via (19) is

$$\delta P(z) = \sum_{j=1}^{j\,max}\int_{z_i}^{z_i+z_F} g\,\delta\rho(z')\,dz'$$

Table 1. Expected Signal-to-Noise Ratios (SNR) and Phase Precision

	GPS/MET, AS-Off	AS-Off, High SNR	AS-On, High SNR
C/A SNR_V (1 s)	300	1000	1000
C/A phase (mm)	0.13	0.04	0.04
Ion corrected phase	0.4	0.12	0.2
1 s phase error after double differencing	0.8	0.24	0.4

AS, Anti-Spoofing; C/A, Coarse Acquisition.

where $j_{max} = (z_h - z)/z_F$ and z_h ($\leq z_Q$) is the height at which the hydrostatic integral is started. Since the $\delta\rho$ errors are independent of one another, the rms pressure error is random walk in form described as

$$\langle \delta P(z)^2 \rangle^{1/2} = \langle \delta\rho^2 \rangle^{1/2} g\, z_F^{1/2} (z_h - z)^{1/2} \quad (25)$$

The square root dependence on altitude in (25) represents the weakest height dependence of any pressure error considered here, and the fractional pressure error therefore decreases rapidly as z decreases because of the exponential increase in pressure with decreasing height.

3.3.3. Temperature errors. Combining (24) and (25) into (23) yields

$$\frac{\langle \delta T(z)^2 \rangle^{1/2}}{T(z)} \cong \frac{\langle \delta\rho^2 \rangle^{1/2}}{\rho(z)} \left[\frac{z_F (z_h - z)}{H(z)^2} - 2\frac{z_F}{H(z)} + 1 \right]^{1/2} \quad (26)$$

where $H(z)$ is the pressure scale height at the altitude z. Beginning at z_h, the density error contribution (the third term in the brackets) dominates that of the pressure error (the first term in the brackets) until $(z_h - z) \sim H^2/z_F$, which for representative values of $z_F = 1.4$ km and $H = 7$ km, is about 5 scale heights or 35 km. Therefore, the density error contribution to temperature error generally dominates that contributed by pressure error in altitude regions where the contribution of thermal noise is significant.

3.4. Clock and Troposphere Errors

Since signal phase is the principle observable in occultation observations, the phase stability of the reference clocks of the GPS transmitters and receivers is important. The phase error associated with fractional frequency stabilities of 10^{-13} available from ultrastable quartz oscillators does not limit accuracy. GPS satellite cesium clock instabilities are approximately an order of magnitude larger over the timescales of interest (0.01 to 60 s) and could be important at high altitudes. The most significant clock-related error at present is the intentional variation of the GPS signal frequencies, referred to as selective availability (SA), which is applied for security reasons. Removal of the SA modulation, which would otherwise ruin the observations, and clock instability via differencing, is discussed in section 3.8.

Even though clock error can largely be removed through differencing, it will be characterized here for several reasons. First, a tropospherically induced error is introduced on the GPS links to ground-based receivers used in differencing (section 3.8) with stability characteristics very similar to those of high-quality crystal oscillators. Second, if the SA modulation is turned off as the *National Research Council* [1995] has recommended, it can be advantageous to not difference, depending on the magnitude of clock error relative to the penalties incurred in increased thermal and local multipath errors. Finally, since this work represents a broad and systematic assessment of radio occultation technique accuracy, the results developed here are also relevant to planetary occultation experiments where differencing is not an option.

Clock noise is best described in the Fourier frequency domain, and the transformation of clock phase error into refractivity, density, pressure, and temperature will therefore be characterized in terms of the Fourier domain relationships developed by *Kursinski* [1997].

3.4.1 Refractivity density, pressure, and temperature error. The phase noise spectra of reference clocks is generally power law in form [*Barnes et al.*, 1971]:

$$S_\phi(f) = \sum_{k=1}^{k\,max} A_k |f|^{-b_k} \quad (27)$$

where f is the Fourier frequency. For noise characterized by $b \leq 2$, which includes the cesium and rubidium clocks used on the GPS satellite transmitters and hydrogen maser frequency references used on the ground, (27) can be plugged into the Fourier domain equations for mean square errors in refractivity, density, pressure, and temperature, respectively, in the work of *Kursinski* [1997], to estimate errors in these same quantities due to clock instability. For $b \geq 3$, which includes quartz oscillators used in many space-borne applications, filtering to attenuate the low-frequency phase noise is required to make the refractivity variance finite. Differencing the phase of each occultation measurement with the phase of measurements taken just prior to the occultation can provide the necessary attenuation. In this case, the filtered phase noise power spectrum $S_{\phi filt}(f)$ is defined as

$$S_{\phi\,filt}(f) = 4 \sin^2(\pi f t_{occ})\, S_\phi(f) \quad (28)$$

where t_{OCC} is the length of an occultation. For clock phase noise characterized by $3 \leq b \leq 4$, (28) can be plugged into the mean square error equations of *Kursinski* [1997] to estimate errors in refractivity, density, pressure, and temperature.

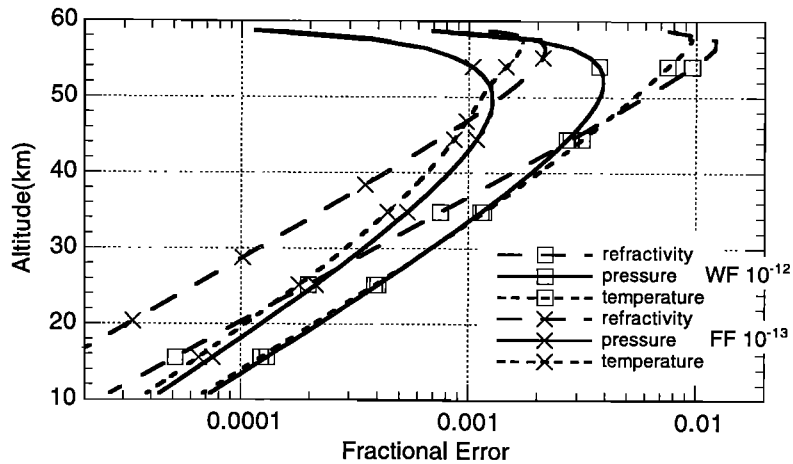

Figure 8. Fractional refractivity, pressure, and temperature errors resulting from clock-type instabilities. (a) $\sigma_y(1\text{ s}) = 10^{-13}$, b=3 representative of ultra-stable quartz oscillators or tropospheric propagation noise. (b) $\sigma_y(1\text{ s}) = 10^{-12}$, b=2 representative of GPS satellite cesium oscillator instabilities.

3.4.2. Discussion. Figure 8 shows fractional rms refractivity, pressure, and temperature errors for two types of noise. The first represents GPS transmitter cesium clock noise (b=2 or white frequency (WF) noise with a 1 s Allan deviation of 10^{-12}). The second is representative of ultrastable quartz clocks noise such as the TOPEX and Mars Observer oscillators and tropospheric noise introduced on the differencing links described previously (b=3 or flicker frequency (FF) noise with a 1 s Allan deviation of 10^{-13}). In both cases the Abel transform is initiated at 60 km. The difference between the cesium and the quartz type errors is indicative of the improvement which results if the GPS transmitter clock instability is differenced out. While the 1% refractivity error near 60 km due to the cesium will have some influence on refractivity accuracy, the small magnitude of these errors indicates clock errors should not dominate retrieval error in general.

3.5. Local Multipath

The broad-beam receiver antennas which significantly simplify GPS instrumentation are unfortunately sensitive to local multipath which occurs when multiple images of the signal arrive at the antenna after scattering off structures in the vicinity of the antenna. In contrast, atmospheric multipath occurs when sharp vertical variations in atmospheric refractivity structure create multiple, simultaneous signal paths through the atmosphere. As discussed in more detail by *Kursinski* [1997], local multipath creates slowly varying phase errors, a fraction of a wavelength in magnitude which affects accuracy, particularly pressure and geopotential accuracy, in the middle atmosphere where it may be the limiting error.

To evaluate the impact of local multipath on the retrieved refractivity profiles, the Fourier representation of the refractivity retrieval scheme developed by *Kursinski* [1997] is used. The multipath phase noise spectrum depends on the specific antenna and spacecraft configuration. Therefore in order to make further progress, some spectral characteristics must be assumed. A reasonable first-order approximation is to take a representative local multipath phase noise variance σ_ϕ^2 and distribute it uniformly across a frequency interval, $\pm\Delta f$ in width. A frequency cut off of 0.01 Hz is used, representative of the high frequency limit for multipath on a 1 m size spacecraft [*Kursinski*, 1997]. The rms phase error σ_ϕ will be taken as 10 mm, representative of expected values for broad beam antennas [*Kursinski*, 1997].

3.5.1. Refractivity, pressure, and temperature error. Plugging the local multipath noise power spectral density of $\sigma_\phi^2/(2\Delta f)$ into the fourier domain equations for mean square errors in refractivity, density, pressure, and temperature, respectively, in the work of *Kursinski* [1997] yields estimates of rms errors in these same quantities. Refractivity error grows as the square root of Δz, the altitude interval between the retrieval altitude and the Abel integral initialization altitude z_u. The pressure error grows as $\Delta z^{3/2}$, consistent with (19). At 10 mm rms and z_u= 60 km, the refractivity error is of the order of 1% between 50 and 60 km and decreases rapidly at lower altitudes. The resulting pressure error is significant throughout the stratosphere with an rms geopotential height error ranging from about 60 m near the stratopause to 6 m at 20 km altitude, indicating multipath may limit geopotential accuracy through much of the stratosphere, particularly under nighttime or solar minimum conditions.

The fractional temperature error is the difference between the fractional refractivity and pressure errors. The maximum temperature error occurs about 3 km below z_u and for z_u = 60 km the error is ~2.5 K. Temperature error also exhibits a distinct minimum at 1.5 scale heights below z_u, consistent with the refractivity and pressure error scaling with Δz as discussed in section 3.2. The secondary maximum error near 40 km is about 0.8 K. In the future, more directional antennas may reduce this error at a cost of instrumental complexity, cost, and size. Also, scattering in the vicinity of the receiving antenna may be modeled such that multipath error is reduced during processing.

3.6. Orbit Determination

As discussed in section 2.2, knowledge of the time-evolving viewing geometry is fundamental to interpreting the occultation observations, and errors in geometry will degrade retrieved accuracy. The present level of orbital accuracy which can be achieved using GPS, is sufficient to make their contribution to retrieval errors very small.

3.6.1. Position Errors. Satellite position primarily affects retrieved refractivity altitudes. GPS transmitter and LEO receiver orbits are known to the meter and several centimeter levels, respectively [*Bertiger et al.*, 1994]. For a receiver orbiting at 700 km altitude the distance from the transmitter to the limb is roughly 9 times that of the receiver to the limb, such that the uncertainty in the ray path height at the limb is ~10 cm. Since other errors limit the geopotential height of pressure surfaces to at least the meter level, the contribution of a position error is not significant.

3.6.2. Refractivity, Pressure and Temperature Errors due to Velocity Error. Orbital velocity error affects the retrieval process primarily through the component of the velocity error projected along the ray path. This component contributes directly as an erroneous atmospheric Doppler frequency. An error in velocity can therefore be treated as a frequency estimation error using the impulse response approach described in section 3.2. The velocity of the receiver can be determined to ~0.05 mm s^{-1} [*Bertiger and Wu*, 1996]. Figure 9 shows the effect of a 0.05 mm s^{-1} velocity error on refractivity, pressure and temperature. All errors are small with a maximum rms errors in geopotential height and temperature errors of ~10 m and 0.3 K at ~50 km and 57 km, respectively, for z_u = 60 km. The errors decrease rapidly at lower altitudes indicating orbital velocity error should not limit retrieval accuracy at any altitude. Orbital acceleration errors over the short occultation duration are very small and therefore negligible.

3.7. Incomplete Calibration of the Ionosphere

The signal path is bent during propagation through the ionosphere on the way into and out of the neutral atmosphere. This bending effect must be removed to derive an accurate representation of neutral atmospheric structure, particularly at stratospheric altitudes and above. Although the presently used calibration scheme of *Vorob'ev and Krasil'nikova* [1993] removes most of the ionospheric effect, some residual remains. Simple simulations indicate that the nighttime ionospheric structure during the maximum of the solar cycle and daytime ionosphere at solar minimum will be removed to a level below that of other significant errors. Simulations also indicate that residual daytime ionosphere during solar maximum will be a limiting source of error in the stratosphere with the presently used calibration scheme. Small-scale ionospheric structure not eliminated entirely in the calibration process will appear as bursts of noise in the retrievals.

Ionospheric refractivity is dispersive and represented to first order (in MKS units) as $40.3\times10^6\, n_e/f^2$, where n_e is the electron density and f is the radio signal frequency. The full Appleton-Hartree expression for ionospheric refractivity is given by *Papas* [1965], and a more complete power series expansion can be found, for example, in the work of *Bassiri and Hajj* [1993]. Each GPS satellite continually radiates signals at two frequencies such that the dispersive ionospheric effect observed on links to ground-based receivers can be removed to

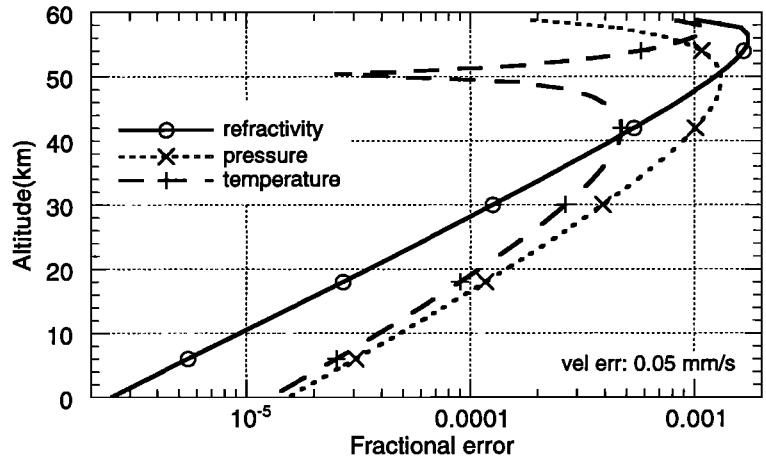

Figure 9. Fractional refractivity, pressure, and temperature errors resulting from a 0.05 mm/s velocity error along the line of site between the transmitter and the receiver.

first order using a linear combination of the two GPS signal frequencies

$$c_1 L_1 - (c_1 - 1) L_2 = L$$

where L is the optical path length along a signal path defined as

$$L_{opt} = \int_{path} n\, dl = \int_{path} (1 + N)\, dl$$

L_1 and L_2 are the optical path lengths at the two GPS signal frequencies, 1.57542 and 1.2276 GHz, respectively, and the coefficient,

$$c_1 = \left(1 - f_2^2/f_1^2\right)^{-1}$$

is equal to 2.5457.

In an occultation geometry, dispersive separation of the two GPS signal paths necessitates a different approach such as the one used here which was developed by *Vorob'ev and Krasil'nikova* [1993]. Substituting for the index of refraction given in (7) and (1) and expending in powers of ($1/f$) keeping only the first two leading terms, the total bending of the radio signal (assuming a spherically symmetric index of refraction) is given by

$$\alpha(a) = 2a \int_{r_0}^{\infty} \frac{\frac{dn_{neut}}{dr}\, dr}{n_{neut}\sqrt{(n_{neut} r)^2 - a^2}} + 2a \frac{40.3}{f^2} \int_{r_0}^{\infty} \frac{\frac{dn_e}{dr}\, dr}{n_{neut}\sqrt{(n_{neut} r)^2 - a^2}} . \quad (29)$$

The first and second terms on the RHS of (29) correspond to the bending induced by the neutral atmosphere and ionosphere, respectively. The ionosphere-free bending is then

$$\alpha_{ion-free}(a) = c_1 \alpha_1(a) - (c_1 - 1)\alpha_2(a) \quad (30)$$

where α_1 and α_2 are the total bending angles for the two GPS signal frequencies. Application of (30) requires, in general, that the discrete set of derived values of $\alpha_2(a_2)$ be interpolated to the set of a_1 values.

A penalty in applying this calibration is the amplification of thermal and local multipath errors. Assuming thermal noise at the two signal frequencies is comparable, the rms thermal error after application of the calibration is increased by a factor of ~3. The effect on local multipath noise scales similarly. This amplification factor of 3 is included in the discussions of thermal and local multipath noise in sections 3.3 and 3.5.

To quantify to first order the performance of (30) at removing the effects of the ionosphere, simulated occultation measurements have been generated by ray tracing through a model consisting of Chapman layer representations of the F and E layers of the ionosphere and a representative neutral atmosphere. The four extremes of the diurnal and solar cycles have been represented on the basis of the typical midlatitude ionosphere electron densities [*Rich and Basu*, 1985; *Kelley*, 1989]. Table 2 shows the residual bending angle error at 60 km altitude left after calibration for each of the four cases.

3.7.1. Pressure and temperature. The nighttime solar minimum error is very small and the nighttime solar maximum and daytime solar minimum errors are sufficiently similar that only daytime solar maximum and nighttime solar maximum errors will be considered further. The impact of the

Table 2. Error Due to Incomplete Calibration of the Ionosphere

Solar and Diurnal Cycles	Fractional Bending Angle Error at 60 km	Fractional Refractivity Error at 55 km	Height (km) Where Fractional Refractivity Error = 0.001
Solar maximum, daytime	-0.065	-0.03	38
Solar maximum, nighttime	-0.004	-0.0017	51
Solar minimum, daytime	-0.0025	-0.0012	53
Solar minimum, nighttime	-0.0001	-0.00005	>> 60

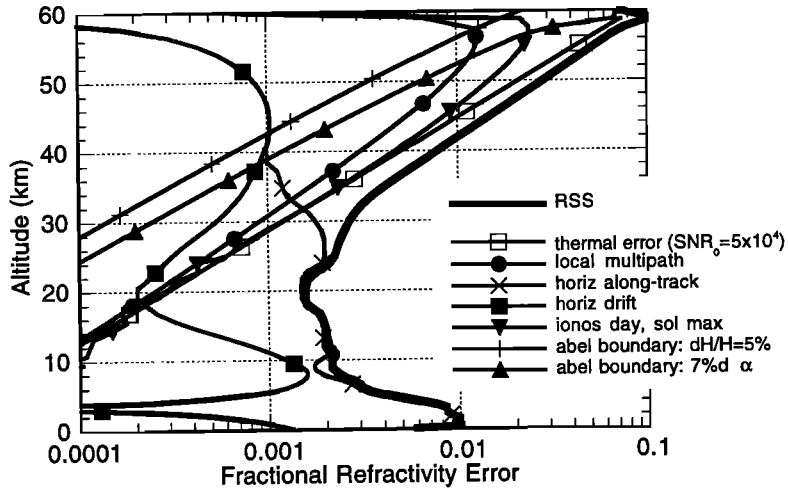

Figure 10. Summary of refractivity errors versus height. Thermal error, 1 s SNR=5 x 10^4; local multipath, 10 mm rms spread over 0.01 Hz; horizontal refractivity structure, along track from simulation and horizontal motion of ray path tangent point from tropospheric and stratospheric climatologies near 30°S for June-July-August; ionosphere error, daytime, solar maximum conditions; Abel boundary errors, 7% in α, 5% in H_α.

daytime, solar maximum ionosphere on derived refractivity, pressure, and temperature is shown in Figures 10-12. Analogous results for nighttime solar maximum ionosphere conditions are shown in Figures 13-15. The Abel and hydrostatic integrals in Figures 10-15 were initiated with occultation data at 60 km. Refractivity errors increase approximately as the square root of Δz and fractional refractivity error therefore grows approximately exponentially with height. The geopotential height error in Figure 11 indicates that residual ionosphere during daytime solar maximum conditions will limit accuracy above 25 km altitude. The peak temperature error of 6.5 K for daytime, solar maximum conditions occurs one Fresnel diameter below 60 km, and a secondary peak of -1.5 K occurs near 43 km (Figure 12). The temperature error for all cases goes through zero near 50 km, consistent with the square root dependence of refractivity error on altitude (section 3.2). The other three ionosphere cases do not appear to limit accuracy.

3.7.2. Discussion. The fractional errors in density, pressure, and temperature all decrease rapidly with decreasing height because the density, pressure, and temperature errors vary slowly relative to the exponential dependence of pressure and density on height. The negative bias apparent in the refractivity errors in Table 2 indicates that the calibration scheme defined by (30), overcorrects slightly for the effects of the ionosphere and may be the one source of error which leaves a systematic bias signature in the retrievals. The temperature error behavior will be somewhat more complicated, as indicated in Figures 12 and 15.

The residual ionosphere errors in Figures 10-15 can be improved using a better calibration scheme which leaves a residual zero-mean error. Higher-order corrections to upward looking ground-based GPS receiver observations have been developed to reduce errors by an order of magnitude [*Bassiri and Hajj*, 1993]. A similar higher-order correction scheme should

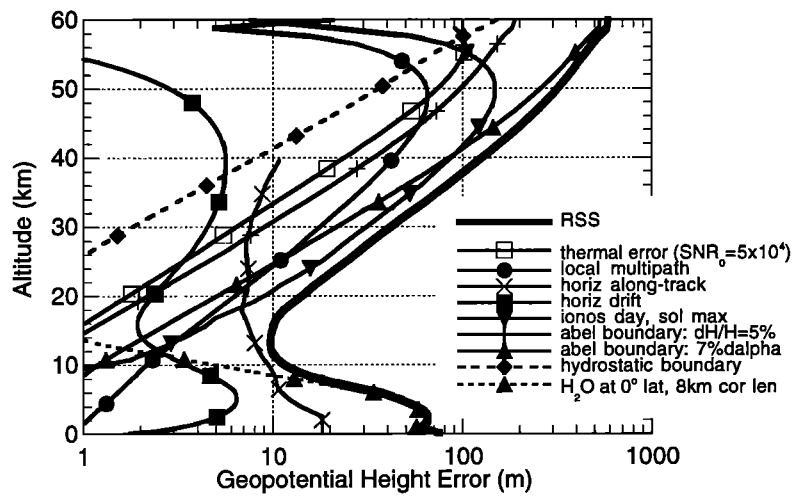

Figure 11. Summary of geopotential height errors versus height. Thermal error, 1 s SNR=5x10^4; local multipath, 10 mm rms spread over 0.01 Hz; horizontal refractivity structure, along track from simulation and horizontal motion of ray path tangent point from tropospheric and stratospheric climatologies near 30°S for June-July-August; ionosphere error, daytime, solar maximum conditions; Abel boundary error, 7% in α, 5% in H_α; hydrostatic boundary error, 5 K; tropospheric water vapor, 0° latitude with 8 km vertical correlation length based on Figure 22.

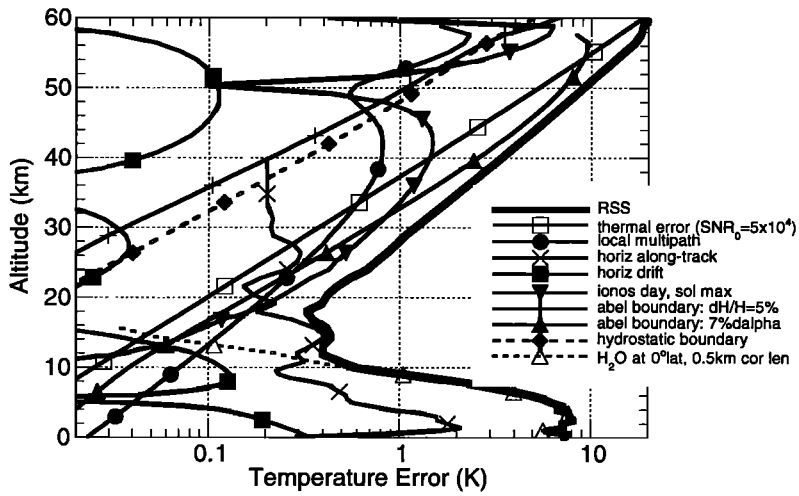

Figure 12. Summary of temperature errors versus height. Conditions same as Figure 11.

reduce ionospheric residual errors by at least a factor of 3. Nighttime observations at stratospheric altitudes should be very accurate for climate studies using the first-order correction.

3.7.3. Caveats. The double Chapman layer representation of the F and E regions of the ionosphere used in the simulations presented here is realistic in a first-order climatological sense. However, it contains neither horizontal nor small-scale variations in structure. In the presence of horizontal variations, another source of error not considered here enters in the inversion process because the total bending is derived on the basis of the assumption of spherical symmetry of the total index of refraction. This assumption is far less accurate in the ionosphere than in the neutral atmosphere due to the fact that the ray probes the ionosphere with a much longer scale than the neutral atmosphere. However, the error introduced by the nonspherical symmetry of the ionosphere is of the order of $(1/f^2)$ or higher (simply because the total ionospheric bending is of the order of $(1/f^2)$ or higher); therefore the linear combination of (30) will cancel the $(1/f^2)$ term leaving residual higher-order terms which are comparable with the terms considered in the simulation.

Calibration of small-scale variations in plasma density may be more problematic. Because the ray paths of the two GPS signal frequencies do not overlap for their entire length, the effect of plasma structure which varies over the scale of the separation between the two paths (of the order of 10-500 m depending on the ionosphere and the tangent height) does not cancel completely when the present calibration is applied. In addition, structural variations on vertical scales smaller than the Fresnel zone diameter will produce scintillation (diffraction) effects which differ at the two wavelengths because Fresnel zone size depends on wavelength (equation (14)). These effects will be relatively rapid, somewhat similar to thermal noise and will be present during portions of occultations. The E region, which exhibits sharp, small-scale structure and can vary dramatically over timescales of minutes [*Kelley*, 1989], is a likely culprit. Further, ionospheric scintillations produced at low latitudes by occasional rapid evening recombination events or magnetic storm activity will produce some residual effect because of sub-Fresnel structure. The overall conclusion is that the residual errors simulated here are probably representative at least in a climatological sense,but a more complete assessment of the impact of the ionosphere is

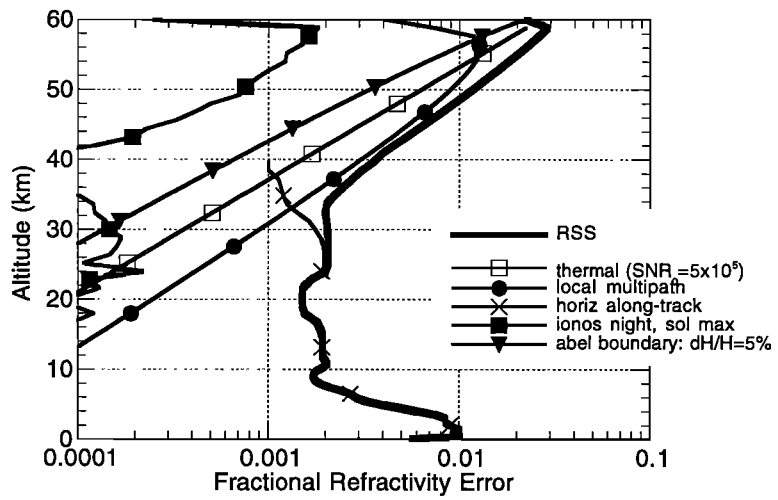

Figure 13. Summary of refractivity errors versus height. Thermal error, 1 s SNR=5x10^5; local multipath, 10 mm rms spread over 0.01 Hz; horizontal refractivity structure, along track from simulation; ionosphere error, nighttime, solar maximum conditions; Abel boundary error, 5% in H_α.

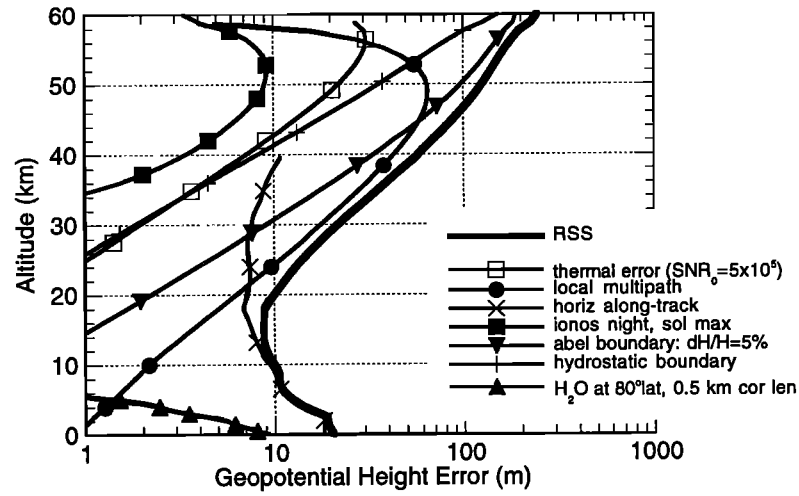

Figure 14. Summary of geopotential height errors versus height. Thermal error, 1 s SNR=5x10^5; local multipath, 10 mm rms spread over 0.01 Hz; horizontal refractivity structure, along track from simulation; ionosphere error, nighttime, solar maximum conditions; Abel boundary error, 5% in H_α; hydrostatic boundary error, 5 K; tropospheric water vapor, 80° latitude with 0.5 km vertical correlation length based on Figure 22.

warranted, as is the development of a higher-order calibration scheme.

3.8. Differencing Schemes to Remove Clock Instabilities

The instability of the transmitter and receiver reference clocks and more importantly the SA encryption on the transmitter signal can be reduced to insignificant levels by differencing. Use of the double differencing scheme was in fact a crucial factor enabling the prototype GPS-MET mission through substantial reduction of both cost and development schedule. While the SA modulation can be eliminated with a classified facility, a more attractive, unclassified approach is to eliminate the SA modulation and inherent clock instabilities by differencing [*Hajj and Kursinski*, 1991, *Hardy et al.* 1994]. The general receiver and transmitter geometry required for differencing is shown in Figure 16. Three differencing schemes are summarized in Table 3.

The differencing concept can be understood using scheme 1 in Table 3. In scheme 1 the carrier phase of link A (the occultation link in Figure 16) is subtracted from that of link B (the link between GPS1 and a ground receiver), which differences out the GPS1 SA modulation and clock instabilities effectively replacing them with the instabilities of the ground receiver reference clock. Reduction or removal of the SA modulation without a classified facility requires either schemes 1 or 3. With either of these schemes and 1 s sampling and cubic interpolation, phase errors due to the SA modulation can be reduced to less than 0.1 mm [*Wu et al.*, 1990]. The reduction of receiver clock instabilities with schemes 2 and 3 eliminates the need for a high-quality receiver clock which significantly reduces the size, power, and cost of LEO receiver instrumentation.

The penalty of a differencing scheme is the additional thermal and local multipath noise on each differencing link. Since thermal noise is uncorrelated between links, the rms thermal error increases as the square root of the number of links, assuming the thermal noise on all links is comparable. Increases in local multipath error scale similarly. In the future, substantial improvements are expected in the SNR of the orbiting receiver measurements (section 3.3). It is therefore important in differencing schemes 1 or 3 that similar substantial improvements be made to the set of differencing receivers such

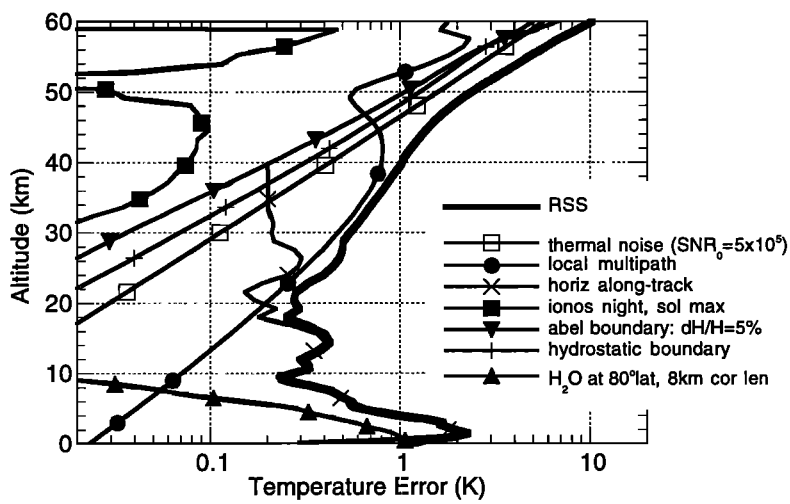

Figure 15. Summary of temperature errors versus height. Conditions same as Figure 14.

Table 3. Summary of differencing schemes to remove clock error

Differencing Scheme	Number of Transmitters	Number of Receivers	Links in Figure 21	Eliminates:	Thermal and Multipath Error Magnification
1, single transmitter difference	1	2	A,B	SA and transmitter clock	$\sqrt{2}$
2, single receiver differencing	2	1	A,C	receiver clock	$\sqrt{2}$
3, double differencing	2	2	A,B,C,D	SA and all clocks	2

that their SNRs are comparable with the SNRs of the flight receiver measurements or else the improved flight receiver SNR will have been wasted.

As mentioned in section 3.4, another penalty is introduced if the second receiver in schemes 1 and 3 is ground-based, caused by phase variations incurred during signal propagation through the troposphere on links B and D. This tropospheric noise is roughly equivalent to that of a quartz oscillator with 10^{-13} fractional frequency stability at 1 second integration time [*Treuheft and Lanyi*, 1987; *Linfield*, 1996] and is generally small compared with other sources of noise (section 3.4).

3.9. Refractivity Constant Uncertainties and Nonideal Behavior

The accuracy of the relationships among atmospheric refractivity, density, pressure, temperature, and water vapor as defined in (7) and the ideal gas law will be examined. Compressibility and nonideal behavior in the equations of refractivity and state lead to corrections up to 0.09% at the surface which decrease roughly in proportion to pressure at higher altitudes. The corrections should be included to achieve sub-Kelvin temperature accuracies expected in the upper troposphere (Figures 12 and 15). In the future, with a more general nonspherical retrieval process, some improvement in the refractivity equation and constants may be desirable.

3.9.1. Equation of Refractivity. The accuracy of variables derived from refractivity depends on the accuracy to which the relationship among refractivity, pressure, temperature, and water vapor is known. Equation (31) gives a more general expression for atmospheric refractivity than (7). It contains three terms representing dry gas polarizability, water vapor polarizability, and the permanent dipole moment of water vapor and includes effects of compressibility [*Thayer*, 1974]:

$$N = 77.60\left(P_d/T\right)Z_a^{-1} + 64.8\left(P_w/T\right)Z_w^{-1} + 3.776\times10^5\left(P_w/T^2\right)Z_w^{-1} \tag{31}$$

where P_a and P_W are the partial pressure of the dry gas and water vapor in mbar, T is temperature in Kelvin, and Z_a and Z_W are compressibility factors given by *Owens* [1967] as

$$Z_a^{-1} = 1 + P_a\left[5.79\times10^{-7}\left(1 + 0.52/T\right) - 9.4611\times10^{-4}t/T^2\right]$$

$$Z_w^{-1} = 1 + 1650\left(P_w/T^3\right)\left[1 - 0.01317t + 1.75\times10^{-4}t^2 + 1.44\times10^{-6}t^3\right]$$

where t is temperature in Celsius.

The uncertainty of the dry refractivity term in (31) is 0.02% [*Thayer*, 1974]. The *additional* uncertainty from the approximations in (7) for dry air is <0.06% (<0.03% above 500 mbar), due to neglect of the compressibility factor.

The uncertainty of the wet refractivity terms is approximately 1 %, due to the difficulty of measuring water vapor density. Use of (11) introduces a fractional error in wet refractivity of 1% (T-359)/300 due to the simplification of two terms and < 0.4% due to the neglect of the compressibility factor. The error in retrieved humidity will be < 2% due to errors in the refractivity formula that is used. Since occultations may ultimately yield near-surface, tropical humidities accurate to ~1% [*Kursinski et al.*, 1995], an improved knowledge of the wet refractivity constants in (31) may become desirable.

3.9.2. Equation of State. The van der Waals' equation of state which includes a first-order representation of nonideal behavior is given as

$$\left(P + n^2a\right)\left(1 - nb\right) = nRT \tag{32}$$

where n is number density in moles m^{-3}, $a = 0.0014$ m^6 mbar $mole^{-2}$, and $b = 3.75 \times 10^{-5}$ m^3 $mole^{-1}$. The values of a and b represent weighted averages of the important atmospheric constituents, nitrogen, oxygen, argon, and water.

3.9.3. Derivation of Density, Pressure and Temperature from Refractivity. Solving for n as a function of P and T (ignoring the cubic term in equation (32)) yields

$$n = \frac{P}{RT}\left[1 + \frac{P}{RT}\left(\frac{a}{RT} - b\right)\right] \tag{33}$$

Neglecting the effects of moisture, which are discussed in section 3.13, (31) and (33) can be combined to relate n as a function of N and T

$$n = \frac{N}{Rb_1}\left[1 + \frac{N}{Rb_1}\left(\frac{a}{RT} - b - b_aRT\right)\right] \tag{34}$$

where b_a is 5.79 x 10^{-7} $mbar^{-1}$ and b_1 is 77.60 N-unit K $mbar^{-1}$. The fractional difference in the densities defined by (34) and (8) is

$$\frac{\delta n}{n} = \frac{N}{Rb_1}\left(\frac{a}{RT} - b - b_aRT\right) \tag{35}$$

To evaluate the error defined in (35), a linear temperature gradient $\dot{T}$ will be assumed with

$$T = T_0 + \dot{T}\ (z - z_0),$$

$$\frac{P}{P_0} = \left(\frac{T}{T_0}\right)^{-mg/R\dot{T}} = \left(\frac{T}{T_0}\right)^{-c_0},$$

$$n \approx \frac{P_0}{R}T_0^{c_0}T^{-c_0-1} = c_1T^{-c_0-1}$$

such that the density error is

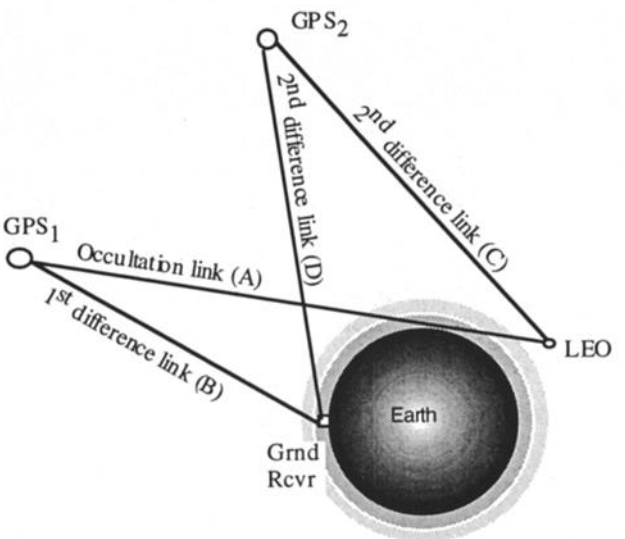

Figure 16. Geometry required for differencing to remove clock instabilities.

$$\delta n = n^2\left(\frac{a}{RT} - b - b_a RT\right) = c_1^2 T^{-2c_0-2}\left(\frac{a}{RT} - b - b_a RT\right) \quad (36)$$

Hydrostatically integrating the density error in (36) determines the pressure error, δP. The change in pressure error between two heights z_1 and z_2 is therefore given as

$$\delta P_2 - \delta P_1 = R c_0 c_1^2 T^{-2c_0-2}\left(\frac{a}{R(2c_0+2)} - \frac{bT}{(2c_0+1)} - \frac{b_a R T^2}{2c_0}\right)\Bigg|_{T_1}^{T_2} \quad (37)$$

The temperature error δT is the difference between the true temperature T and the temperature $\hat{T}_{ideal}$ derived from the ideal gas law. $\hat{T}_{ideal}$ contains errors because the density and pressure estimates are imperfect, and errors in converting pressure and density to temperature. Therefore the temperature error is

$$\delta T = T - \hat{T}_{ideal} = \frac{P}{nR}\left(1 + \frac{n^2 a}{P} - nb\right) - \frac{\hat{P}}{\hat{n}R} = \left(\frac{P}{nR} - \frac{\hat{P}}{\hat{n}R}\right) + \frac{P}{nR}\left(\frac{n^2 a}{P} - nb\right)$$

The first term in parentheses on the RHS is the temperature error resulting from errors in pressure and density. The second parenthetical term is the contribution from the nonideal portion of the van der Waals equation of state. From (22) the fractional error of $\hat{T}_{ideal}$ is the difference between the fractional pressure and the fractional density errors. Therefore

$$\delta T = \frac{P}{nR}\left(\frac{\delta P}{P} - \frac{\delta n}{n}\right) + \frac{P}{nR}\left(\frac{n^2 a}{P} - nb\right) \quad (38)$$

Combining (38) and (35) gives

$$\delta T = \frac{P}{nR}\left(\frac{\delta P}{P} + b_a nRT\right) = \frac{P}{nR}\left(\frac{\delta P}{P} + b_a P\right) \quad (39)$$

Figure 17 shows the density, pressure, and temperature errors for a simple mid-latitude atmosphere model with a surface temperature of 288 K, a constant lapse rate between the surface and the tropopause near 12 km ($T_{tropopause}$ ~ 215 K), and a constant lapse rate between the tropopause and the stratopause at 50 km ($T_{stratopause}$ ~ 260 K). The density and pressure errors are less than 0.04%. The maximum temperature error of ~0.09% occurs at the surface and decreases rapidly to <0.04% at 10 km altitude. Errors under tropical conditions are similar. The errors in Figure 17 are generally small in comparison with other sources of error. However, to derive temperatures accurate to tenths of a Kelvin in the upper troposphere (Figures 12 and 15), the effects of compressibility and nonideal behavior should be included to reduce errors in Figure 17 by at least an order of magnitude.

3.10. Upper Altitude Boundary Errors

The upper integration limits of the Abel and hydrostatic integrals extend to an infinite altitude whereas the occultation observations do not. Therefore high-altitude density and bending angle structure used in these integrals must be estimated above some maximum altitude z_u below which the occultation data are used directly in the integrals. Incorrectly estimated atmospheric structure above z_u will produce errors in refractivity, density, pressure and temperature at altitudes below z_u which will decrease with decreasing altitude and can limit accuracy over altitudes several scale heights below z_u. It is therefore desirable to start these integrals as high as possible. The trade-off of balancing these errors and other errors described in this section determines the altitude at which to start the Abel and hydrostatic integrals and is discussed in section 3.14. High-altitude climatological data will be used to characterize the variability and therefore the expected accuracy of estimated high-altitude atmospheric structure.

3.10.1. Abel Transform Upper Boundary. The Abel transform integrates bending angle times a weighting factor as a function of asymptotic miss distance with an upper integration limit of infinity (equation (2)). To estimate atmospheric bending above the altitude z_u where the data become too noisy or biased to be used directly in the Abel integral, a simple, climatologically based model can be used in which a few free parameters describe typical high altitude atmospheric structure for that latitude and season. The parameters can be estimated from a combination of measurements, including the occultation observations themselves, models, and climatology.

For the purpose of this discussion, a simple exponentially decaying model of $\alpha(a)$ above z_u will be used to characterize to first order the sensitivity of the refractivity and other retrieved variables to the high-altitude atmospheric model. This model has two free parameters, bending angle at z_u ($\alpha(z_u)$) and bend-

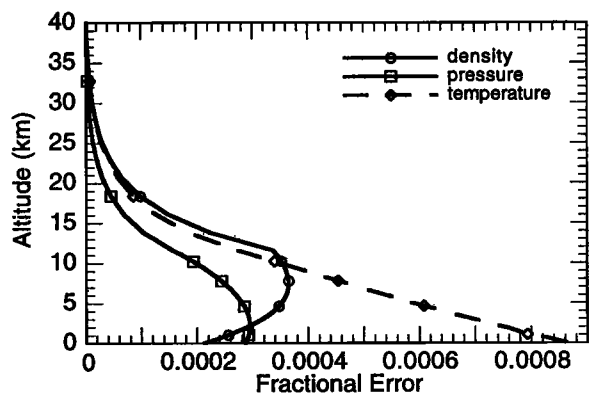

Figure 17. Fractional density, pressure, and temperature errors due to approximations in refractivity equation (equation (7)) and ideal gas law for conditions representative of midlatitudes.

Table 4. Comparison of Error Magnitudes at 60 km Altitude

Source of Error	Fractional Bending Angle Error (radians)
Orbital velocity	0.003
Local multipath (1 cm rms, 0-0.01 Hz spectrum)	0.006
Thermal noise (SNR (1 s) = 10^6, τ = 2 s)	0.0025
Ionosphere: daytime, solar maximum	0.07 (60 km) 0.03 (55 km)
Ionosphere: nighttime, solar maximum	0.004

ing angle scale height (H_α). Sensitivity of the retrieved variables such as refractivity can be characterized by varying $\alpha(z_u)$ and H_α. The $\alpha(z_u)$ can be estimated accurately from the occultation data if errors are small relative to the atmospheric bending. From (5) and (7), it can be shown that bending angle error due to frequency measurement error is approximately

$$\delta\alpha = \delta f \, \lambda / v_\perp$$

where δf is the frequency measurement error, λ is the GPS signal wavelength, and $v_\perp$ is the ray path descent velocity in the absence of the atmosphere. The error in $\alpha(z_u)$ for several types of error is given in Table 4.

On the basis of the U.S. Standard Atmosphere a nominal 60 km altitude bending angle of 5×10^{-6} radians is used in Table 4. The magnitudes of local multipath and orbital velocity errors have been discussed previously in sections 3.5 and 3.6. The thermal noise error in Table 4 corresponds to a 1 s SNR (signal power divided by thermal noise power) of 10^6 and an integration time of 2 s, roughly the time for the ray path to descend one scale height in the mesosphere, and includes amplification factors of 3 for the ionosphere correction and $2^{1/2}$ for clock differencing.

Under nighttime solar maximum conditions, where ionospheric electron densities are relatively small, the orbital velocity, local multipath, thermal, and nighttime solar maximum errors are comparable, yielding fractional bending angle and refractivity errors of the order of 1% or less at 60 km. Under daytime conditions during solar cycle maximum, incomplete removal of the ionosphere dominates the bending angle error at 60 km. The influence of the ionosphere error can be reduced by decreasing the altitude z_u at which the Abel integral is initiated with occultation data, although as indicated in section 3.14, 60 km is not far from optimum for minimizing overall errors near the tropopause. With the present ionosphere calibration scheme, this residual ionosphere error is also systematic and will bias derived refractivity.

The accuracy of the bending angle scale height estimate H_α depends on knowledge of atmospheric structure primarily over the three scale heights above z_u. Since bending angle scales in proportion to the vertical density gradient, the bending angle scale height is approximately the density scale height. The density scale height reflects the average temperature structure over several scale heights immediately above z_u. While the scale height can be estimated at z_u from the occultation measurements, the variations in the temperature structure above z_u are more difficult to estimate. On the basis of the 60 to 90 km climatology of *Champion et al.* [1985] the largest variations in the middle stratosphere to the mesopause regime occur during winter months in the Arctic and subarctic regions associated with sudden warming events. The variations in temperature between 60 and 90 km can be as large as +15/-30 K (+7/-14%). Since variations at other latitudes and seasons are smaller, a value of 10 K will be used here as globally representative of rms temperature variations with respect to mean seasonal climatology at a given height and location; 10 K corresponds to a fractional scale height uncertainty of ~5% which causes a refractivity error at z_u of roughly 2.5%.

On the basis of the estimated errors in $\alpha(z_u)$ and H_α for z_u =60 km under solar maximum nighttime conditions, the scale height error will primarily determine the refractivity error associated with the upper boundary of the Abel transform. Under daytime solar maximum conditions, the uncertainty in $\alpha(z_u)$ due to residual ionosphere will exceed the scale height uncertainty, and the refractivity error at z_u = 60 km will be ~7%.

3.10.2. Pressure and Temperature Errors. Hydrostatic equilibrium, integrated over a finite vertical interval, provides the change in pressure over the interval. Obtaining total pressure requires knowledge of the pressure at the upper boundary z_u of the hydrostatic integral. Fractional variations in pressure at mesospheric altitudes can be large because pressure at a given height depends exponentially on the temperature at all altitudes below. Since fractional temperature variations at heights near 60 km are generally smaller than the pressure variations, the pressure at z_u can be estimated using the density retrieved via the Abel transform and an estimate of temperature at z_u. The resulting fractional pressure error at z_u is

$$\frac{\delta P}{P}(z_u) = \frac{\delta T}{T}(z_u) + \frac{\delta \rho}{\rho}(z_u)$$

The temperature error term at z_u represents the a priori uncertainty in $T(z_u)$ and will be discussed shortly. The fractional density error at z_u (which is equal to the fractional refractivity error) is the error due to the Abel upper boundary error just discussed. As shown in Figure 18, refractivity error due to the extrapolated bending angle model decreases with decreasing altitude below z_u, and the pressure error therefore increases slowly over this same range. The fractional refractivity and pressure errors therefore decrease almost exponentially with decreasing height (Figures 10, 11, 13, 14). The fractional temperature error contribution begins at zero at z_u and increases until it nearly equals the fractional pressure error.

3.10.3. Pressure and temperature errors due to initial temperature guess. The error in the temperature guess at z_u used to initiate the hydrostatic integral produces a constant pressure error. Therefore the fractional pressure error

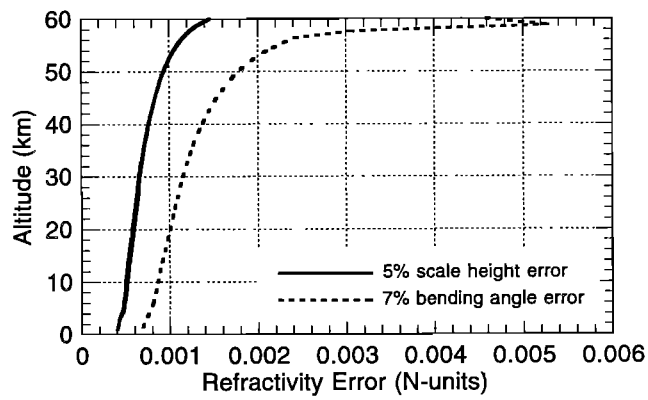

Figure 18. Refractivity boundary error in Abel transform due to error in simple exponential bending angle structure extrapolated above 60 km, the height below which occultation data are utilized in the Abel transform. Solid line, 5% in bending angle scale height H_α. Dashed line, 7% error in α(60 km) .

caused by this boundary error decreases exponentially with decreasing height. Since there is no refractivity error associated with the error in the initial temperature guess, the corresponding fractional temperature error equals the fractional pressure error such that

$$\frac{\delta T(z)}{T(z)} = \frac{\delta P(z)}{P(z)} = \frac{\delta T(z_u)}{T(z_u)} \frac{P(z_u)}{P(z)} \cong \frac{\delta T(z_u)}{T(z_u)} \exp\left(-\frac{(z_u - z)}{H}\right)$$

where H is the average pressure scale height over the altitude interval z to z_u. For example, a 2% or ~5 K temperature guess error at 0.2 mbar (~60 km) will produce a 0.004% pressure and temperature error at 100 mbar (~16 km) equivalent to a 0.25 m error in geopotential height and 0.01 K error in temperature. The impact of the initial temperature guess is therefore far more significant at high altitudes, and it is desirable to raise z_u as high as possible to minimize its contribution at a given altitude.

3.11. Horizontal Refractivity Structure

Conversion of observed atmospheric Doppler shift into bending angle versus asymptotic miss distance and the subsequent derivation into refractivity versus height assume spherical symmetry in the vicinity of the ray path. This assumption works quite well because the contribution to bending is focused around the ray path tangent point (Figure 5). To assess the impact of horizontal refractivity variations, simulations using a 51 level, 40 km resolution, regional model have been performed. The results indicate that horizontal variations in refractivity will limit retrieval accuracy from the lower stratosphere down to the lower troposphere. The limiting rms errors in temperature and geopotential height are estimated to be a few tenths Kelvin and 7 to 8 m. Ultimately, more general retrieval approaches will be developed which account for horizontal structure and improve upon the accuracy in the lower atmosphere.

Before discussing the simulation results, some intuition can be developed about the effect of horizontal refractivity variations on retrieval accuracy. Contours of constant atmospheric density would follow the geoid (defining a level of constant geopotential) in the absence of atmospheric dynamics. The geoid in turn can be approximated by an ellipsoid to an accuracy better than 100 m. The local center of curvature defined at the tangent to the ellipsoid can be used to interpret the occultation measurements. Therefore it is informative to consider a radius of curvature error where the atmosphere is spherically symmetric, but the assumed and actual centers of curvature differ. It can be shown that under these conditions, the values of a used in the Abel transform are incorrect, resulting in an error in refractivity δN such that

$$\frac{\delta N}{N} \cong -\frac{\delta a}{2a}\left(1 + \frac{aN}{H_N}\right) \tag{40}$$

where H_N is the refractivity scale height [*Kursinski*, 1997]. From (40) a fractional refractivity error of 10^{-3} requires a center of curvature error of the order of 10 km. Equation (40) indicates that the difference between the equatorial and polar radii of the Earth would produce systematic fractional refractivity errors of the order of 2×10^{-3}. Of course, since the shape of the geoid is known to the meter level, the nonspherical shape can be accounted for. In fact, an ellipsoid-based, local radius of curvature reduces this error by a factor of 100 or more.

Atmospheric dynamics alter the shape of constant density surfaces relative to the geoid. These distortions are generally small (but nonnegligible) over the 200 km and larger horizontal scales relevant to occultation measurements. The largest horizontal refractivity variations and therefore refractivity errors occur in the warm, lower troposphere caused by water vapor whose horizontal variations are not constrained by hydrostatic equilibrium in the same manner as the bulk gas.

3.11.1. Error due to Along-Track Horizontal Refractivity Structure. To characterize refractivity errors associated with realistic horizontal refractivity variations, retrievals have been simulated using both temperature and water fields obtained from a 40 km resolution National Meteorological Center (NMC) regional forecast ETA model [*Janjic*, 1990; *Mesinger et al.* 1988], modified by M. Zupanski for Atmospheric Infrared Sounder (AIRS) data simulation activities. The area covered by the model spanned roughly from Hawaii to the Great Lakes. Simulated measurements were created by ray tracing signal paths from GPS satellites through the model atmospheric structure to a receiver in low Earth orbit. Profiles of refractivity were then derived from the measurements using the Abel transform. The retrieved refractivity error statistics of Figures 10 and 13 show that rms errors are of the order of 0.2% above 500 mbar and increase rapidly at lower levels to approximately 1% associated with increasing horizontal humidity gradients. At the top of the trade wind inversion (~800 mbar) a layer roughly 200 m thick can contain vertical refractivity gradients sufficiently large for critical refraction to occur. As discussed in section 2.4, signal paths whose tangent heights lie within such a layer cannot emerge from the atmosphere. The current implementation of the retrieval scheme does not account for the bending angle singularity at the critical layer and does not derive refractivity accurately below critically refracting layers, so only profiles without critical refraction are included in Figures 10 and 13 below 800 mbar. As discussed in section 2.4, the refractivity profile within and below the critically refracting layer will be accurately derived with an improved Abel transform implementation.

3.11.2. Pressure and Temperature Accuracy. Figures 11 and 14 show the rms error in retrieved geopotential height. Again, the increase in rms error in the lower troposphere is associated with horizontal humidity gradients. RMS temperature error contributions are typically around 0.25 K above 400 mbar (~7 km) increasing to ~2 K within 3 km of the surface (Figures 12 and 15). The mean temperature error above 4 km is generally less than 0.05 K.

3.11.3. Horizontal Motion During an Occultation. Occultations are seldom diametric because the transmitter and receiver orbits are generally not coplanar, causing the ray path tangent point to drift horizontally as it descends through the atmosphere. The horizontal drift of the ray-path tangent point leads to an error in refractivity because the bending angle derived at higher altitudes is not the bending angle directly above the present tangent point. The ray path drift is generally of the order of the horizontal averaging interval or less, and the resulting errors are therefore relatively small. The ratio of horizontal drift to vertical descent is greatest near the surface and the largest errors can therefore be expected there.

The bending angle error $\delta\alpha(z,z_l,y)$ caused by horizontal drift of the ray path tangent point is given to first order as

$$\delta\alpha(z,z_l,y) = \Delta y(z,z_l,y)\frac{\partial\alpha}{\partial y}(z,y) \tag{41}$$

where z is the height of the error, z_l is the height of the lower integration limit of the Abel transform and the height of the refractivity retrieval, and Δy is the horizontal distance the ray path tangent point has drifted between heights z and z_l.

3.11.4. Horizontal drift. The motion of the tangent point is determined by the geometric motion between the transmitter and the receiver relative to the Earth. For occultations where the direction to the transmitter is within $\pm 45^\circ$ of the velocity vector, the ratio of horizontal to vertical motion of the ray path tangent point relative to the limb of the Earth

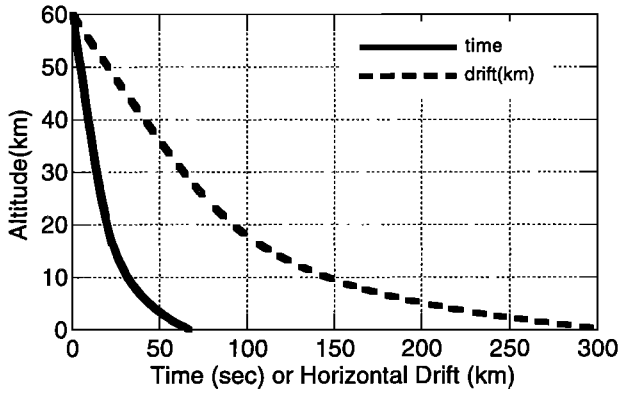

Figure 19. Ray path tangent height versus time (solid line) and versus horizontal location (dashed line) for an occultation located 30° in azimuth off the LEO velocity vector.

ranges from 0 to 3 at the top of the atmosphere. The number of daily occultations falling within ±45° of the receiver velocity vector for a high inclination orbit is 500, defining the number typically quoted as the daily occultations per orbiting receiver (another ~200 daily occultations occur at larger azimuths). As the raypath descends through the lower stratosphere, the vertical component of tangent point velocity slows as bending increases, while the horizontal component of motion remains basically unchanged. Near the surface the vertical descent velocity has decreased by an order of magnitude or more relative to the high-altitude descent velocity. For example, in the isothermal case of Figure 19 the ratio of horizontal to vertical displacement of the ray path tangent point ($\equiv dy/dz$) is 2 at the top of the atmosphere, whereas at the surface, $dy/dz \sim 30$. In this example the 10 km altitude ray path tangent point has drifted 140 km horizontally relative to its location at 60 km altitude, whereas over the last 10 km of descent to the surface, the ray path drifts an additional 160 km for a total drift of the order of 300 km, demonstrating the significant increase in horizontal drift near the surface.

3.11.5. Horizontal gradient of α. To simplify the discussion of the horizontal variation in α, α will be taken as proportional to the vertical density gradient such that $\alpha \sim c\,\rho/H_\rho$ where c is a scale factor, ρ is mass density, and H_ρ is the density scale height. This is a reasonable first approximation because the contribution to bending is very focused toward the ray path tangent region (Figure 5). With this approximation,

$$\frac{\partial \alpha}{\alpha\,\partial y}(z,y) \simeq \frac{\partial \rho}{\rho\,\partial y}(z,y) - \frac{\partial H_\rho}{H_\rho\,\partial y}(z,y) \simeq \frac{\partial \rho}{\rho\,\partial y}(z,y) - \frac{\partial T}{T\,\partial y}(z,y) \tag{42}$$

The density gradient can be characterized in terms of geostrophic and thermal wind balance. Taking the vertical gradient of the zonal geostrophic wind balance equation gives

$$\frac{\partial}{\partial z}(\rho u_g) = -\frac{1}{f}\frac{\partial}{\partial y}\frac{\partial p}{\partial z} = \frac{g}{f}\frac{\partial \rho}{\partial y}$$

from which the fractional meridional gradient of density can be related to the zonal geostrophic wind as

$$\frac{\partial \rho}{\rho\,\partial y} = \frac{f}{g}\left(\frac{\partial u_g}{\partial z} + \frac{u_g}{\rho}\frac{\partial \rho}{\partial z}\right) = \frac{f}{g}\left(\frac{\partial u_g}{\partial z} - \frac{u_g}{H_\rho}\right) \tag{43}$$

Further, the meridional temperature gradient in (42) is related to the vertical gradient of the geostrophic wind such that

$$\frac{\partial T}{T\,\partial y} = -\frac{H}{RT}\frac{f}{}\frac{\partial u_g}{\partial z} = -\frac{f}{g}\frac{\partial u_g}{\partial z} \tag{44}$$

Equations (42) and (44) relate the horizontal gradient of bending angle to the geostrophic wind such that

$$\frac{\partial \alpha}{\alpha\,\partial y} \simeq \frac{f}{g}\left(2\frac{\partial u_g}{\partial z} - \frac{u_g}{H_\rho}\right) \tag{45}$$

To estimate realistic and representative retrieval errors, the gradients have been derived from the climatology of the 25° to 40° south latitude band for the June-July-August period. This region contains some of the largest horizontal gradients and jets in both the troposphere and the stratosphere. The climatological gradients of this region should exceed typical atmospheric gradients and therefore yield generally conservative estimates of retrieved refractivity, pressure, and temperature accuracy. On the other hand, these gradients may yield error estimates within a factor of 2 or 3 of severe weather conditions.

Between 25°S and 40°S in the troposphere the peak zonal wind is ~35 m s^{-1} near 200 mbar, and the vertical gradient of the zonal wind between the surface and 200 mbar ranges from 2 to 4×10^{-3} s^{-1} [*Peixoto and Oort*, 1992, Figures 7.15 and 7.16]. Of the two terms in the parentheses of (45), the vertical gradient dominates in the lower half of the troposphere and the scale height term becomes larger near the jet. The net magnitude of the fractional bending angle gradient is ~5×10^{-5} km^{-1}. In the stratosphere the gradient grows from a value near 0 at 30 km to a value of 1.4×10^{-4} km^{-1} due primarily to the scale height term in.(45) and 100 m s^{-1} jet near the stratopause.

Figure 20 shows the refractivity, pressure, and temperature errors which result from the ~30°S climatological conditions for a 2:1 horizontal to vertical displacement ratio at the top of the atmosphere. All fractional error magnitudes are of the order of 0.1% or smaller. The two jets at 10 and 50 km have magnitudes of 35 and 100 m/s. The stratopause jet, through the scale height term in (45), dominates the error structure above 30 km. The peak in refractivity error and rapid reversal in sign of its slope near 8 km is associated with the change in sign of the gradient term in (45) above and below the jet at 10 km. The rapid increase in the near-surface error is associated with the relatively large horizontal drift in the ray path location there.

3.11.6. Pressure and Temperature Errors. The pressure error lags the refractivity error with a peak geopotential height error of about 6 or 7 m near 6 km altitude. In the 10 to 20 km altitude range, where the occultation observations are generally most accurate, the geopotential error goes through a relative minimum of 2 to 3 m and should not limit overall geopotential accuracy. Geopotential height errors in the

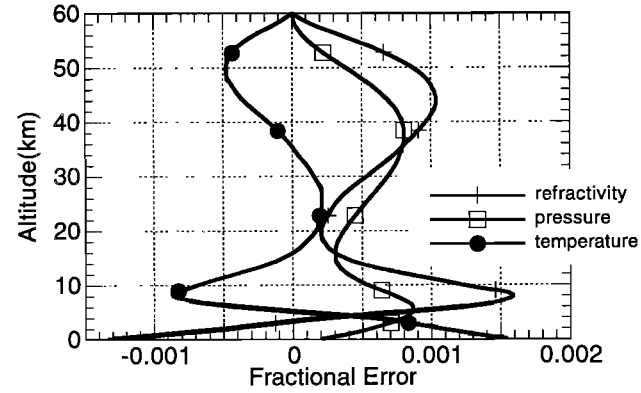

Figure 20. Fractional refractivity, pressure, and temperature error resulting from horizontal drift of ray path tangent point during the occultation based on June-July-August climatologies near 30°S for the troposphere from *Peixoto and Oort* [1992], and stratosphere from *Andrews et al.* [1987].

stratosphere range from 0 at 60 km to a peak of ~7 m near 40 km. Peak tropospheric temperature errors of about 0.2 K and 0.5 K occur near 8 km and the surface, respectively. Temperature errors in the stratosphere are generally less than 0.1 K.

3.11.7. Discussion. Since the dry horizontal gradients used to estimate the effect of horizontal motion of the ray path are representative of the largest climatological values found in the lower and middle atmosphere, the accuracy estimates should be generally conservative for dry regions. Errors under extreme weather conditions can be expected to exceed these estimates at least near the surface.

The horizontal structure of atmospheric water vapor will be important at low altitudes with a strong dependence on temperature. During warm tropospheric conditions in the summer hemisphere and the tropics, baroclinicity tends to be small on average and water vapor abundances large such that horizontal refractivity structure in the warmer regions of the lower troposphere will typically be dominated by water vapor. During winter when baroclinicity is often large, the temperature dependence of water vapor abundance tends to reduce refractivity contrast across winter cold fronts [*Hardy et al.*, 1994]. The refractivity of air on the cold side of the front has a higher dry density contribution due to the low temperature, whereas on the warm side, the dry density contribution is slightly lower due to warmer temperatures, but it is offset by the contribution of higher specific humidity. A more complete assessment of the influence of water is left as an area of future research as this and other data sets improve upon the presently limited knowledge of the distribution of atmospheric water vapor.

A final comment is that eventually, when multiple occultations are used in the retrieval process, the horizontal refractivity structure will be part of the solution and will improve upon the accuracies estimated here to the extent that the density of occultations is sufficient to observe the horizontal structure. Similar statements can also be made regarding use of models in the retrieval/assimilation process and the horizontal resolution of the models.

3.12 Accuracy of the Geometric Optics Approximation

Except for a brief mention of diffraction during the discussion on resolution in section 2.5 the geometric optics approximation has been assumed almost throughout. The error in this approximation can be assessed in comparison with a full diffraction approach. The results shown here are based upon on a series of simulations representative of the sharp changes in temperature lapse rate which may be found around the tropical tropopause. The results of a comparison between diffraction and geometric optics approaches indicate that the geometric optics approach is accurate to several tenths of a Kelvin near the tropopause and above.

The effects of diffraction were investigated in the vicinity of the tropopause because of the sharp change in density (and refractivity) scale height there. The dry density scale height is given as

$$H_\rho = H\left(1 + \frac{H\,dT}{T\,dz}\right)^{-1}$$

where H is the pressure scale height (RT/mg). The change in temperature gradient across the tropopause from a negative value in the troposphere to a positive one in the lower stratosphere above causes the density scale height in the overlying region to be smaller than that in the underlying region.

Forward modeling with diffraction was done with a series of intermediate "planes" (with values a function of only one coordinate along these planes because of spherical symmetry) between the transmitter and the receiver. Geometric ray tracing, including defocusing, determined the phase and amplitude at the first plane. Propagation between planes was accomplished in two steps. The first step consisted of geometric ray tracing from all points on a grid in one plane to all points on a grid in the second plane (i.e., a two-dimensional set of traces). This ray tracing established the phase and amplitude on the first plane, as seen from the second plane. A Fresnel integration then determined the amplitude and phase at the second plane. At the height of the tropopause, use of one intermediate plane (near the true impact plane) was adequate, based on its agreement with calculations for three, five and seven planes. For thicker atmospheric conditions (e.g., at lower altitudes in the troposphere), one plane may not suffice.

To characterize the error in the geometric optics approximation, the diffraction pattern in signal phase arising from sharp tropopause structures was simulated. The simulated phase was then passed through the retrieval process described in sections 2.2 and 2.3. The retrieved structure was then compared to the input (model) temperature profile. The results of four sample cases are given in Figure 21. Figures 21 a and 21 b each contain a single change in temperature lapse rate, with case b having the larger change. Figures 21 c and 21 d contain two and three lapse rate changes, respectively, with a separation of 0.5 km between the changes. The geometrically retrieved minimum temperature is systematically larger than the true minimum temperature because the sharp corner in the temperature structure is not resolved. The height of the minimum temperature in Figures 21 a and 21 b is also slightly higher than the actual tropopause by 200 to 300 m. The temperature differences in the lower set of panels in the Figure show the retrieval errors, which in all cases are ≤ 0.8 K and, except for the peak of the central error spike, are generally much less than that. The vertical extent of the error is mostly contained within ± 0.7 km (the radius of the first Fresnel zone) of the sharp structures. In Figure 21 d, which is perhaps the closest to typical tropopause structure, errors are 0.2 K or less. The rms error over the 15 and 16.5 km altitude interval is roughly 0.1 K. A small positive bias less than 0.05 K also exists over this interval. There will be no appreciable error in pressure because of the short vertical extent and small mean behavior of the effects.

The magnitude of the error when using the geometric optics approximation will depend on the sharpness of the tropopause. The results of Figure 17 indicate that errors due to sharp structure in the upper troposphere and above can be expected to be of the order of several tenths of a Kelvin or less. An investigation of lower troposphere diffraction effects, which will probably be larger due to water vapor structures, is planned. It is worth noting that the sharpness of changes in vertical thermal gradients at the tropopause will be apparent because it will produce a diffraction spike in the received signal amplitude as the signal path crosses the region. Some of the GPS/MET occultations clearly exhibit such spikes, indicating the existence of a very sharp change in lapse rate at the tropopause. These represent obvious regions where modeling of the effects of diffraction, as mentioned in section 2.5, would be warranted to retrieve the sub-Fresnel scale structure which apparently exists there.

3.13. Water Vapor Ambiguity

In the warm regions of the lower troposphere, water vapor contributes a large fraction of atmospheric refractivity at microwave wavelengths. Water vapor can therefore be derived from occultation observations, the accuracy of which was summarized in section 2.3. The high specific humidity in these regions also means uncertainties in humidity will adversely affect the accuracy of retrieved density, pressure, and temperature. The effect of water vapor is a strong function of latitude and height such that low-latitude derivations of temperature will be limited by uncertainties in water below 9 km,

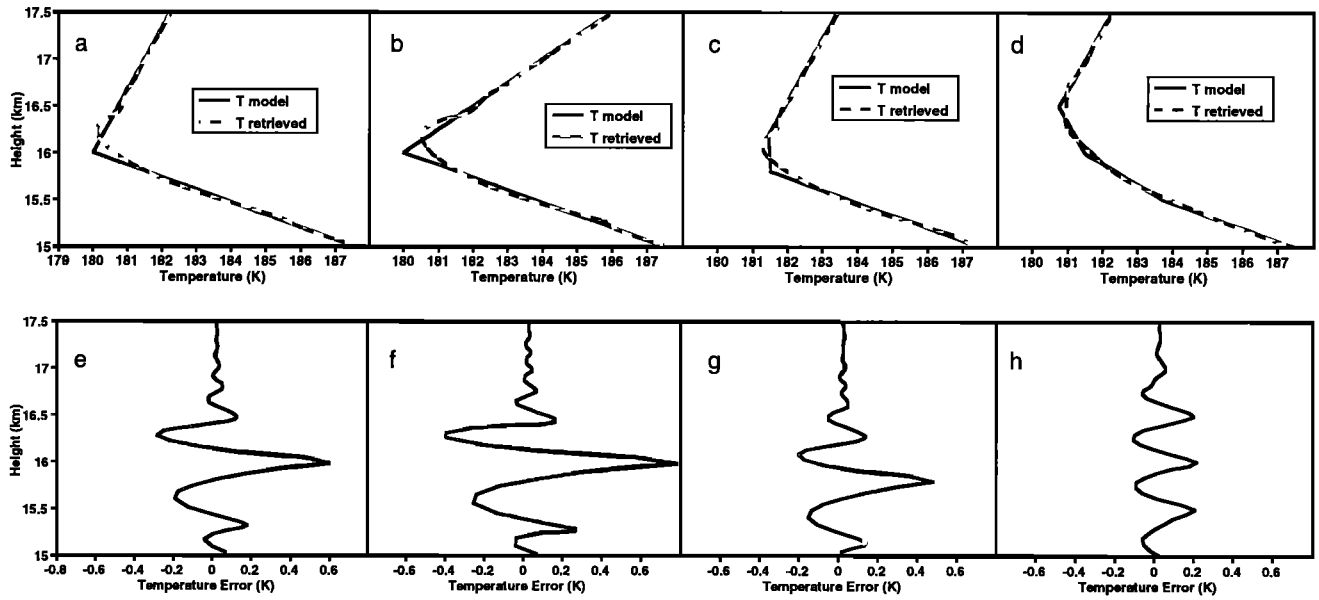

Figure 21. Errors in the geometric optics approximation under tropical tropopause-like conditions. (a-d) Four cases of model temperature (solid line) and geometrically retrieved temperature (dashed line) versus height. (e-h) Temperature difference (retrieved minus model) versus height.

whereas high-latitude temperature accuracy will on average be better than 2 K down to the surface.

The influence of water vapor on the GPS occultation observations was realized almost with the conception of the idea [*Yunck et al.*, 1988]. When water vapor contributions to refractivity are significant, there are three equations (state, hydrostatic equilibrium, and refractivity) and four unknowns (density, pressure, temperature, and humidity). Therefore additional information is required to separate the wet and dry contributions to refractivity.

3.13.1. Density, pressure and temperature accuracy. The refractivity equation, (11), can be differentiated to relate uncertainties in humidity, temperature, and pressure as follows:

$$\frac{dP_w}{P_w} = (B+2)\frac{dT}{T} - B\frac{dP}{P} = 2\frac{dT}{T} - B\frac{d\rho}{\rho}$$

where $B = \frac{b_1 TP}{b_2 P_w}$, and P_W is the partial pressure of water vapor.

For the purposes of this section, refractivity is assumed to be known perfectly. B varies from a minimum value of ~2.5 near the surface in the tropics to of the order of 10^4 at the tropical tropopause and above because of the strong dependence of the water vapor mixing ratio on temperature. The climatological dependence of B on latitude and pressure is given by *Kursinski et al.* [1995]. The impact of water vapor is nonlinear, in fact quite nonlinear for small B, because of the coupling among density, pressure, and temperature via the equations of hydrostatic equilibrium and state. Therefore a Monte Carlo approach has been used to characterize the impact of water. The uncertainty in water vapor is taken to be a percentage of the climatological water vapor abundance. An additional

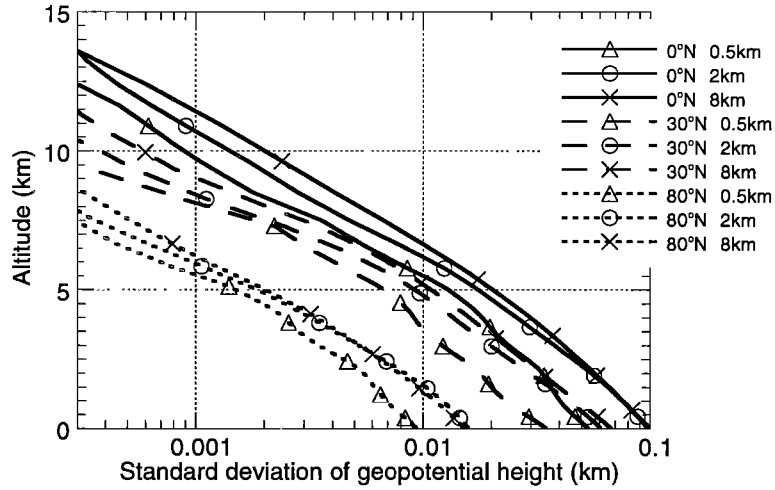

Figure 22. Geopotential height error due to 20% uncertainty in water vapor abundance based on annual climatologies for temperature and water vapor from Peixoto and Oort. Results are shown as a function of three latitudes, equatorial (solid line), 30°N (long dashed) and 80°N (short dashed) and three vertical water vapor uncertainty correlation lengths, 0.5 km (triangles), 2 km (circles), and 8 km (crosses).

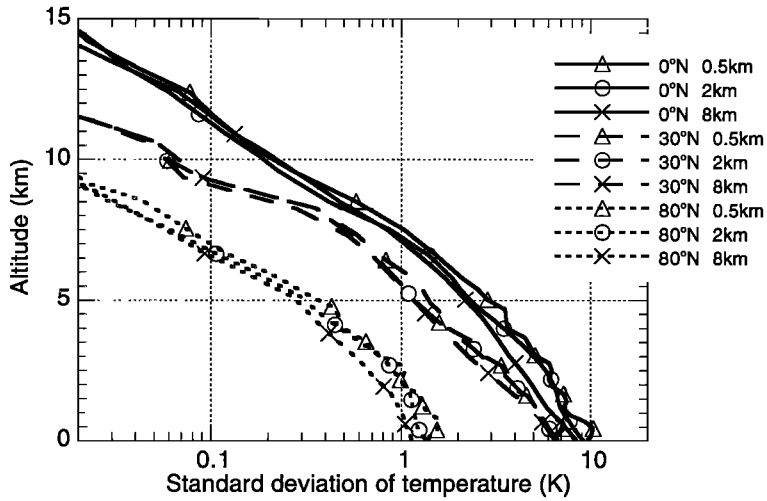

Figure 23. Temperature error due to 20% uncertainty in water vapor abundance. Conditions and legend same as Figure 22.

variable necessary to characterize the impact of water on geopotential is the vertical correlation length of the water vapor uncertainty.

Figures 22 and 23 show the resulting uncertainties in geopotential height and temperature for latitudes of 0°, 30°, and 80° spanning equator to pole. A 20% fractional uncertainty in water vapor is used, representative of uncertainties in the lower troposphere but probably too small in the middle troposphere where 50% or even larger uncertainties may be more representative of present knowledge. Therefore low-latitude accuracies in Figures 22 and 23 between 5 and 10 km altitude should be increased by a factor of 2 to 3 to be more representative of present uncertainties. Vertical correlation lengths in the uncertainty of the water vapor of 8, 2, and 0.5 km are shown, crudely corresponding to the scale height of the background atmosphere, the water vapor scale height, and small-scale vapor layering related perhaps to clouds. Significant changes in the vertical distribution of water vapor can occur over still smaller intervals which can be extrapolated from the results in Figures 22 and 23.

3.13.2. Discussion and Interpretation. The latitudinal and vertical dependence of accuracy in Figures 22 and 23 reflects the strong temperature dependence of atmospheric humidity associated with the Clausius-Clapeyron relation. Low-latitude errors are roughly an order of magnitude larger than those at high latitudes because low-latitude air is moister than high-latitude air by roughly this same factor. The results show that near-surface temperature errors at low latitudes will be 8 to 10 K for a 20% uncertainty in water vapor, whereas at high latitudes, errors will be of the order of 1.5 K or better.

The ~2 km scale height of atmospheric water (H_W), 4 to 5 times smaller than that of the bulk atmosphere (H), largely determines the vertical structure in Figures 22 and 23. The small water scale height means that the impact of water increases dramatically at lower altitudes. Uncertainties in temperature and geopotential increase by a factor ranging from 3 to 10 over the bottom 5 km of the atmosphere. Assuming 50% uncertainty in middle tropospheric water vapor, 1 K temperature accuracy will be limited to altitudes above about 9 km at low latitudes. Another result of the small size of H_W is that the increase in fractional pressure error at lower altitudes lags the increase in fractional density error such that the ratio of the two is of the order of H_W/H or less. Therefore from (22), the fractional temperature error must nearly equal the density error and be much larger than the fractional pressure error. The fractional accuracy of pressure will therefore be better than that of temperature near the surface in warm, moist regions. For instance, at low latitudes, a surface error of 9 K (Figure 23) is an error of ~3% error, whereas a 100 m geopotential height error represents a ~1% error in pressure (Figure 22). The difference is even more pronounced several kilometers above the surface.

Figure 23 also demonstrates that fractional pressure and therefore geopotential accuracy depend on the correlation length of the water vapor uncertainty for lengths less than the water vapor scale height. Reducing the correlation length by a factor of 4 from 2 to 0.5 km reduces the surface geopotential error by roughly a factor of 2, consistent with a square root scaling expected from integrating a randomly varying error (i.e. a random walk process). The height below which the geopotential error exceeds 20 m ranges from between 3.5 and 5 km at the equator and between 1.5 and 3.5 km at 30° depending on water vapor correlation length. RMS geopotential errors at 80° latitude are less than 20 m below 30 km altitude.

3.14. Summary of Refractivity, Density, Pressure, and Temperature Accuracy

The refractivity, pressure and temperature errors discussed earlier have been assembled to establish an overall estimate of accuracy as a function of height, latitude, season, and solar cycle. The predicted temperature accuracy is similar to the original prediction of G. Lindal [*Yunck et al.*, 1988] and subsequent update [*Kursinski*, 1994]. The analysis here also establishes the relative contributions and importance of individual sources of error as well as the vertical range of the retrievals. Because of the relevance to characterizing climate, biases and long-term variations in these errors are discussed later in the section.

Three pairs of Figures are shown, a pair each for refractivity, geopotential, and temperature accuracy as a function of height. The accuracy represents the rms accuracy of individual retrieved profiles. Each pair of Figures represents two extremes in conditions. The lower-accuracy Figure includes conditions representative of daytime solar maximum conditions where the impact of the ionosphere is maximum, relatively low SNR equivalent to that achieved by the prototype GPS/MET mission ($SNR_0=5x10^4$) and low-latitude tropospheric conditions for derived profiles of temperature and pressure where the contribution of water vapor to refractivity is maximum. The more optimal case represents nighttime so-

lar maximum conditions, a relatively high, 1 s SNR of $5x10^5$ expected of future instrumentation and high-latitude tropospheric conditions where the influence of water vapor is minimum. In each Figure, the square root of the sum of the squares of all error contributions is shown at each altitude level representing overall estimated accuracy. The orbit error and contribution of the troposphere on the differencing link discussed in sections 3.4 and 3.6 are small and not shown in this set of Figures in order to reduce clutter. Errors in the geometric optics approximation due to sharp vertical refractivity structure discussed in section 3.12 are not shown because the frequency and statistical distribution of these structures is needed to create representative curves for Figures 10-15. In fact, a global occultation data set may be the only data set capable of quantifying this distribution. A brief description of each Figure summarizing its important features follows.

3.14.1. Figure 10, refractivity: daytime solar maximum, low SNR. The thermal noise at the level of the GPS/MET prototype receiver limits accuracy above 30 km altitude. As discussed in section 3.3, the impact of thermal noise depends strongly on integration time and can be reduced at the expense of vertical resolution. The integration time used in Figure 10 is the time for the ray path to descend a Fresnel diameter (~1.4 km). Increasing the integration time to descend through a layer 2.8 km thick would reduce the thermal contribution to the error by a factor of almost 3, bringing the thermal error down to a level comparable with the ionosphere errors. Horizontal structure limits accuracy below 30 km. The increase in refractivity error below 8 km is due to horizontal refractivity structure associated with higher water vapor concentrations at lower altitudes. The altitude range over which the error is less than 0.4% (crudely equivalent to a 1 K error in temperature) ranges from roughly 5 km to 30 km.

3.14.2. Figure 13, refractivity: nighttime solar maximum, high SNR. Thermal noise and the 5% uncertainty in the high-altitude scale height limit accuracy in the top 5 km. Local multipath limits accuracy between 35 and 55 km. Horizontal refractivity structure limits accuracy below 30 km. Fractional accuracy of 0.4% or better is predicted between 5 and 40 km.

3.14.3. Figure 11, geopotential: daytime solar maximum, low SNR, low-latitude water vapor. Residual ionosphere error limits geopotential accuracy above 20 km. This error includes both the impact on the atmosphere model used above 60 km in the Abel integral discussed in section 3.10 and the impact on derived refractivity below 60 km discussed in section 3.7. The region between 8 and 18 km around the tropopause will be limited by horizontal refractivity structure to an accuracy of 8 to 10 m. At low latitudes in the middle to lower troposphere, the uncertainty in water vapor will limit accuracy causing errors to increase to ~50 to 80 m near the surface. The fractional water vapor uncertainty used in Figure 11 rises from 10% at the surface to 50% at 6 km altitude and above.

3.14.4. Figure 14, geopotential: nighttime solar maximum, high SNR, high-latitude water vapor. The 10 K climatological uncertainty in temperature above 60 km and its impact on the Abel transform (section 3.10) limits geopotential accuracy above 45 km. Local multipath limits accuracy over the altitude interval from 20 to 45 km. Horizontal refractivity structure limits accuracy below 20 km. The water vapor uncertainty represents the best case from Figure 22 (section 3.13) of high-latitude concentrations with a small vertical correlation length of 0.5 km so the hydrostatic integral does not accumulate much pressure error. Under these conditions, geopotential height will be accurate to 20 m or better below about 30 km. The highest accuracies of 8 to 10 m rms are predicted between 10 and 20 km altitude.

3.14.5. Figure 12, temperature: daytime solar maximum, low SNR, low-latitude water vapor. As in Figure 11, the ionosphere causes an erroneous high altitude atmosphere model impacting Abel transform accuracy at high altitudes. This error and the low SNR limit temperature accuracy above 40 km. As discussed in Figure 10, doubling the integration time (2.8 km vertical layer) would reduce the thermal contribution to the error by a factor of almost 3 bringing the thermal error down to a level comparable to the hydrostatic and local multipath errors. Between 17 and 40 km, accuracy is limited by contributions from thermal noise, local multipath, and residual ionosphere which has the largest influence. Between 9 and 17 km, horizontal refractivity structure limits retrieval accuracy. At equatorial latitudes the uncertainty in water abundance limits temperature accuracy below 9 km altitude such that below 6 or 7 km, the occultation data are better used to derive water vapor than temperature (section 4). As in Figure 11, fractional water vapor uncertainty rises from 10% at the surface to 50% at 6 km altitude and above. Temperature accuracies better than 1 K are predicted between 8 and 30 km with accuracies of 0.3 to 0.4 K accuracy expected between 10 and 20 km.

3.14.6. Figure 15, temperature: nighttime solar maximum, high SNR, high-latitude water vapor. Above 45 km altitude, several comparable sources of error influence derived temperature accuracy, including uncertainties in high-altitude structure which influence the Abel and hydrostatic integrals, thermal noise, and local multipath. Local multipath dominates temperature accuracy between 30 and 45 km. Horizontal refractivity structure limits retrieval accuracy between 6 and 20 km. Below 6 km, uncertainty in water abundance dominates the error. Sub-Kelvin accuracy is predicted to extend from 40 km altitude to within 1 or 2 km of the surface.

3.14.7. Diurnal, seasonal, and latitudinal dependence. A few additional comments can be made concerning the dependence of accuracy. In the lower troposphere, accuracy at high latitudes will exhibit a strong seasonal dependence associated with the large variations in temperature and therefore water vapor. The high-latitude results shown in Figures 13-15 represent an annual average so that results during winter will be better, whereas results during summer will look more similar to the midlatitude results in Figures 22 and 23. The magnitude of the horizontal drift error in the lower troposphere should increase some at lower latitudes because of the increase in water vapor abundance and horizontal variations in water vapor abundance. Residual ionosphere error can be expected to exhibit some latitudinal dependence due to systematic latitudinal structure such as the equatorial and auroral jets.

3.14.8. Biases and slowly varying errors. To this point, the error analyses have been concerned primarily with rms errors of individual retrieved profiles. However, for climatic observations, biases and slow systematic variations in the errors are of concern. Sources of error potentially important to biases in profiles of refractivity, pressure, and temperature retrieved in the upper troposphere are local multipath, horizontal refractivity structure, residual ionosphere and assumed water vapor for retrievals in the troposphere.

3.14.8.1. Local multipath: Errors due to local multipath depend systematically on the spacecraft geometry and electrical properties in the vicinity of the receiver antenna as well as the occultation-viewing geometry. To the extent that the viewing geometry changes from occultation to occultation, the local multipath errors will have zero mean and therefore average down when regional and temporal averages are calculated. As mentioned in section 3.5, directional antennas and modeling will reduce the multipath effect. Therefore errors due to local multipath in spatially and temporally averaged occultation profiles acquired by a GPS receiving system designed to make climate observations should be at least an order of

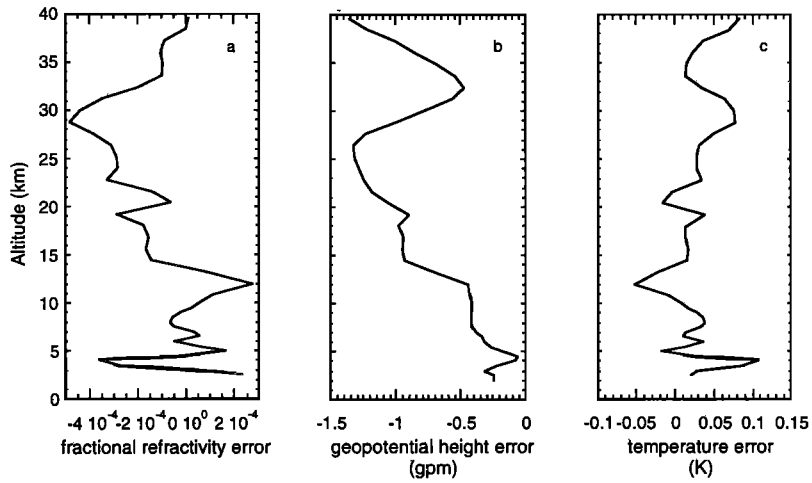

Figure 24. Averages of the refractivity, geopotential height, and temperature errors in 120 simulated retrievals caused by horizontal, along-track refractivity structure discussed in section 3.11.

magnitude smaller than the errors in individual profiles estimated in Figures 10-15.

3.14.8.2. Unmodeled horizontal refractivity structure: In section 3.11, a set of ~120 profiles were simulated to estimate the sensitivity to non spherical refractivity structure. The average refractivity error of the 120 profiles is less than 5 x 10^{-4} and generally less than 2.5 x 10^{-4} for altitudes above 2 km (Figure 24a). The average temperature error (Figure 24c) is less than 0.1 K, indicating a direct sensitivity to temperature at the retrieval altitude, while the average geopotential height error of 1.5 m or less (Figure 24b) indicates the accuracy to which the average temperature of the atmosphere below that height is measured. The error of 1 meter at the height of the tropical tropopause (~16 km) is equivalent to knowing the average temperature of the troposphere to ~0.02 K, a very sensitive measure of average temperature.

As discussed in sections 3.11 and 2.4, a sharp refractivity gradient can exist at the trade wind inversion typically at 1.5 to 2 km altitude over the ocean which is sufficiently large to cause critical refraction (section 2.4) causing problems for the present numerical implementation of the Abel transform, and results at and below 2 km are therefore not shown in Figure 24. As discussed, a numerical implementation of the Abel integral capable of handling the bending angle singularity is being developed as are ray tracing approaches which will significantly reduce this problem.

Persistent dynamical structure will distort surfaces of constant density (and therefore refractivity) relative to the geoid. For example, the strong winter anticyclone over Siberia which disappears by summer in favor of a low-pressure system north of the Indian subcontinent [*Peixoto and Oort*, 1992] will produce systematic seasonal biases in retrieved refractivity, pressure and temperature if not accounted for. Therefore minimizing biases in derived refractivity caused by such structures requires that the curvature of refractivity surfaces used in the retrieval process include both the shape of the geoid and the shape of the climatological density contours (section 3.11). If systematic horizontal structure becomes apparent in the averaged occultation profiles which differs from the climatology, then the climatology should be replaced by the derived systematic horizontal structure and the retrievals should be reestimated until average retrieved refractivity and curvature of constant refractivity surfaces are self-consistent.

3.14.8.3. Ionospheric Errors: Incomplete calibration of the daytime ionosphere will probably be the most important source of error to long-term climate studies because incomplete calibration will allow a small signature of the solar cycle to leak into the derived occultation profiles creating an apparent physical connection between the solar cycle and the atmospheric structure.

The results in section 3.7 indicate that the error in derived refractivity when using the ionosphere calibration scheme of *Vorob'ev and Krasil'nikova* [1993] is approximately independent of altitude, with a magnitude which depends strongly on the diurnal and solar cycles. The greatest systematic variations in error over the solar cycle will occur in daytime observations. Errors during nighttime, solar maximum and daytime, solar minimum conditions are smaller by more than an order of magnitude and insignificant. Daytime ionosphere refractivity error will vary by ~10^{-3} and ~10^{-4} at 30 km and 10 km altitude respectively over the solar cycle (Figure 10). Retrieved daytime temperatures at 30 km and 20 km altitude will systematically shift by 0.8 K and 0.2 K over the solar cycle (Figure 12). Geopotential will likely be the derived variable most affected by daytime ionosphere error because the relatively constant refractivity error with height will integrate to a large fractional error in pressure via the hydrostatic integral. The geopotential height error at 20 km altitude during daytime solar maximum conditions will be of the order of 10 m which is equivalent to a change in the average atmospheric temperature below 20 km of ~0.1 K, which as a worst case error still represents a very sensitive measure of average temperature. At 10 km height the geopotential error will be an order of magnitude less.

Higher order calibration schemes for ground based GPS observations reduce first-order calibration errors by an order of magnitude. A higher-order occultation calibration scheme which accounts for the vertical structure of the ionosphere (which can be derived from the occultation observations themselves) should reduce these errors by at least a factor of 3. A factor of 3 would reduce the daytime solar cycle signature to $3x10^{-4}$ at 30 km and $3x10^{-5}$ at 10 km representing a significant improvement in sensitivity to changes in climate.

3.14.8.4. Assumed water vapor: In deriving temperature and pressure estimates in the warmer regions of the troposphere, additional information about water vapor must be used. To the extent that the water vapor climatology is understood, the assumed water vapor should be consistent with the climatology, and biases will then depend on how good the climatology is.

In summary, biases and slowly varying errors should be at least an order of magnitude smaller than the rms errors of Figures 10-15 with the one notable exception that the variation in

the residual daytime ionosphere over the course of the solar cycle will equal that in Figures 10-12. The variation in daytime temperature error of 0.8K at 30 km over the solar cycle is not large and should be reduced by at least a factor of three with a higher order ionosphere correction. A long-term, database of nighttime observations should provide a still more sensitive set for studying long-term variations in climate.

3.14.9. Caveats to estimated accuracy. Several caveats exist regarding the estimated errors and conclusions. First, as a reminder, the measurements are made in a limb-viewing geometry so accuracies are relevant to a sampling volume roughly 200 to 300 km long and ~1 km across and tall (section 2.5). Caveats regarding removal of the ionosphere have already been discussed in section 3.7 and will not be repeated here. Horizontal refractivity variations in the lower atmosphere may be larger than those in the 40 km resolution regional model used to derive the horizontal sensitivity in Figures 10-15. Gravity waves with horizontal wavelengths ~100 km may impact accuracy depending on the frequency of occurrence and magnitude of these waves [*Belloul and Hauchecorne*, 1997].

The accuracy of refractivity retrieved within a few kilometers of the surface is complicated by the effects of diffraction, critical refraction, and atmospheric multipath. The error due to horizontal drift of the ray path during the occultation estimated in section 3.11 did not include horizontal variations of water vapor and therefore underestimates the error in the lower troposphere at low latitudes. Still it remains difficult to imagine that the errors due to horizontal water vapor inhomogeneity could approach a level comparable with the errors due to the water vapor uncertainty.

3.14.10. Future improvements. Improvements can be made such that accuracies will exceed those estimated in Figures 10-15. As mentioned, signal-to-noise ratio can be increased with higher-gain antennas and lower-noise amplifiers, improving refractivity and temperature accuracy at high altitudes and the ability of the receiver to track the signals at low altitudes. Better antennas will also reduce the magnitude of local multipath, and smaller spacecraft will reduce the impact of local multipath by decreasing the phase rate of the multipath error (*Kursinski*, 1997). An improved ionosphere calibration scheme would substantially improve stratospheric retrievals and reduce systematic error during daytime conditions of the solar cycle maximum. Ultimately, reducing the impact of the ionosphere would best be accomplished with an additional, higher-frequency signal. Sub-Fresnel scale structure may be retrievable by accounting for the effects of diffraction which will improve both resolution and accuracy. Characterization of vertical structure at the 100 to 200 m level might then be possible within several kilometers of the surface where it would be particularly important.

Improvements beyond the already high accuracy predicted in the upper troposphere through the lower stratosphere can be accomplished by combining multiple occultations with other data sets and models, such as the ECMWF weather analysis model, in a grander scale retrieval or assimilation scheme which would consider and derive both vertical and horizontal structure [*Gorbunov and Sokolovskiy*, 1993; *Eyre*, 1994]. The higher density of soundings provided by a constellation of orbiting receivers would be very useful in this regard. Tomographic simulations of *Gorbunov and Sokolovskiy* [1993] indicate a factor of 10 improvement may be achievable. On the basis of Figures 10-15 the improvement would primarily be in the troposphere and lower stratosphere.

3.14.11. Use of external information. The retrieval scheme described here uses the occultation data as much as possible, minimizing the use of independent information. Optimization under these conditions is a balance between the relative contributions of two types of error. The first type consists of the Abel and hydrostatic boundary value errors (section 3.10) where the desire is to raise the upper boundary altitude as high as possible to reduce the impact of the errors at lower altitudes. The other class consists of all other error types where the desire is to lower the upper boundary altitude in order to reduce the accumulation of error, particularly the hydrostatically integrated pressure error, at lower altitudes. The optimum upper boundary altitude which minimizes the error at some lower altitude can be found by approximating the behavior of the dominant error terms with some simple analytical approximations and either directly calculating an optimal altitude or numerically varying the starting altitude to find the minimum error. Taking minimization of error near 100 mbar as the goal, 60 km is not far from optimum. 60 km is a few kilometers higher than the optimum upper boundary altitude under the daytime, solar maximum and low SNR conditions of Figures 10-12, and it is several kilometers too low under the better conditions of Figures 13-15. This assessment assumes that the 5% scale height uncertainty in the upper atmosphere model (section 3.10) is independent of height.

The analysis here has minimized reliance on external information in the retrieval process in order to characterize the informational content of individual occultation soundings and the accuracy expected using an Abelian-based retrieval capability. External information has only been used at the upper boundary of the retrieval process. Despite the limitations of this approach, the resulting accuracy already exceeds that of present and many planned satellite sensors. For instance, sub-Kelvin temperature accuracy, a goal of NASA's Mission to Planet Earth, appears achievable over a significant fraction of the troposphere and stratosphere. A more optimal use of the occultation data can be achieved when the occultation data are combined with independent information with a weighting scheme consistent with the relative accuracies of the respective data types. In addition, accuracy will be improved when horizontal information available in weather analysis models is incorporated in the retrieval process [*Eyre*, 1994].

4. Applications

In this section, several areas of application well suited to the unique combination of features of the atmospheric profiles derived from GPS occultation measurements are discussed and summarized.

4.1. Weather

Assimilating observations of important atmospheric variables into weather models and assessing their impact are major activities within a number of research agencies. Existing data assimilation techniques are easily adapted to exploit the full potential of occultation data to be provided by a suite of spacecraft carrying GPS receivers. Such techniques are ideally suited to ingesting the globally dense but irregularly spaced and timed occultation measurements. Comparisons of data acquired from the prototype GPS-MET mission with atmospheric analyses available every 6 hours from ECMWF have already demonstrated desirable properties for their use in numerical weather prediction (NWP), namely, generally good agreement with a high-quality NWP analysis plus the ability to identify a minority of cases where there is room for significant improvement in the analysis [*Kursinski et al.*, 1996]. In effect, the GPS occultation system extends radiosonde-like measurements to the full globe Even the relatively sparse sampling of 500 daily occultations from a single orbiting receiver will more than double the number of high vertical resolution profiles presently available in the southern hemisphere while providing a far more even distribution. Furthermore, occultation measurement horizontal and vertical resolutions are gen-

erally similar to the horizontal and vertical resolution used in global models.

Data assimilation systems can use the multiple dependencies of the occultation measurement (7) on temperature, pressure, and water vapor directly and determine how to interpret tropospheric refractivity in terms of the moist and dry contributions. Studies evaluating the impact of GPS occultation observations on weather models have either assimilated retrieved refractivity [*Zou et al.*, 1995; *Kuo et al.*, 1996] or bending angle [*Eyre*, 1994]. Bending angle assimilation uses a forward approach where model variables are adjusted until simulated observations generated via ray tracing through the model match the observed bending angles. This approach, while more costly computationally, makes better use of the combined model and GPS data information and constraints.

Kuo et al. [1996] have examined the impact of assimilating refractivity on model extratropical cyclone prediction. Cyclogenesis is driven by vorticity anomalies at the upper and lower boundaries of the troposphere such that the high accuracy of temperatures and pressures derived near the tropopause is well matched to the dynamical importance of the topography of the tropopause [*Hoskins et al.*, 1985]. Kuo et al. examined the impact of refractivity below 3 km by removing it from the data assimilation. The result was a reduction in the rate of deepening of the cyclone in the forecast by more than a factor of 2 clearly demonstrating the constraints of refractivity on low-level temperature and latent heat to cyclogenesis. They also point out that constraints placed by refractivity are particularly important near the baroclinic wave because of the rapid growth of changes in initial conditions as the baroclinic wave develops. Assimilation of refractivity considerably improved the upper level potential vorticity anomaly, the primary upper level forcing mechanism for low-level cyclogenesis, due to the dynamic coupling among temperature, pressure, and winds. The coupling is demonstrated by simple scaling analysis which indicates ~8-10 m geopotential accuracy (Figure 14) is equivalent to 1% accuracy of the midlatitude jet velocities determined over scales of the Rossby radius of deformation.

Since refractivity in the warmer regions of the lower troposphere tightly constrains water vapor [*Kursinski et al.*, 1995], precipitation and moisture forecasts will undoubtably improve, as indicated in the simulation experiments by *Zou et al.* [1995] and *Kuo et al.* [1996]. Since condensed water content is usually a small fraction of total water content, GPS observations sense most of the total water and do so under any and all weather conditions unlike IR measurements. Interestingly, Kuo et al. found that the improvement in the moisture analysis and precipitation is largely lost 12 hours into the forecast, a duration which is short compared to water vapor's climatological mean time aloft of 9 days (≡ mean water content divided by mean precipitation). Since atmospheric water vapor should in some sense be correlated over the 9 days, the decorrelation over 12 hours implies that the processes controling atmospheric water within the model are less than optimum and will limit the impact of the GPS data on the forecast. Given the current state of models, assimilation of occultation data will at least improve the very short term precipitation forecasts.

Another point is that global weather analyses provide the best global stat of the atmosphere and are therefore used in a myriad of other applications such as field campaigns, process studies, and development of climatologies. By improving model analysis accuracy particularly in remote regions, GPS observations will indirectly influence many areas of research.

4.2. Climate

Perhaps the most obvious application of GPS occultation observations is monitoring regional and global atmospheric behavior on seasonal, interannual, and decadal timescales, thereby providing an important segment of the data needed to evaluate climate models. GPS radio occultation observations were in fact originally conceived for the purpose of observing predicted climatic changes in thermal structure from the midtroposphere through the stratosphere [*Yunck et al.*, 1988]. Like the solar occultation observations of Stratospheric Aerosol and Gas Experiment (SAGE), radio occultations have inherent features of self-calibration, high accuracy, and vertical resolution with the additional feature of insensitivity to atmospheric particulates. The GPS has been designed and implemented as a long-term capability implemented by the U.S. military and funded by U.S. taxpayers and will be available for producing a long-term data set needed to observe and understand the behavior of our climate system over the coming decades.

Data used to study climate will be temporally and spatially averaged and the horizontal averaging inherent to the occultation limb-viewing geometry is therefore a desirable feature in the context of climate research. The high accuracy of individual occultation profiles used in constructing regional averages reduces the number of soundings needed to achieve a specified level of measurement accuracy, thus allowing regional trends to be observed more quickly and longer-term trends to be observed more precisely to the extent that measurement accuracy rather than natural variability dominates the uncertainty in identifying longer-term trends and behavior.

4.2.1. Changes in propagation delay. To this point, our discussions have centered around derivation and interpretation of refractivity, pressure, temperature and water vapor from radio occultations. *Yuan et al.* [1993] have suggested another approach utilizing GPS occultation propagation delay as a potential measure of climate change. Their simulations of changes in atmospheric propagation delay using the nine layer NCAR community climate model between model atmospheres with and without a doubling of CO_2 concentration were as large as 300 m near the surface. In warm regions, increases in delay were caused by increased water vapor abundances associated with warming. In cold, high-latitude regions, decreases in delay were observed because near-surface warming caused bulk gas densities and therefore refractivities to decrease. These near-surface signatures are very large relative to the precision to which delay can be measured.

Identifying the signature of an anthropogenically induced change in climate requires that the signature stand out against natural climatic variability. Unfortunately, the same nonlinear sensitivity responsible for the large climatic changes in delay can also produce large natural variability. For example, Figure 25 shows the variations in propagation delay versus ray path tangent height calculated by ray tracing through a set of 61 atmospheres whose vertical structure is defined by the July 1991 radiosonde data set from Hilo, Hawaii, discussed by *Kursinski et al.* [1995]. Root mean square variations in delay over the month are large, in fact larger than the predicted climatic change signature, a result which is somewhat surprising because tropospheric pressure and temperature variations over the month are small at 1 mbar and 0.5 to 2 K.

Propagation delay of signals passing through the lower troposphere depends on vertical gradients of refractivity whose variability is fairly large, particularly that associated with the strength and height of the trade wind inversion typically found near 2 km altitude during the July 1991 period. For example, the standard deviation of water vapor just above the average height of the trade wind inversion is ~50%. The variability in Figure 25 demonstrates the sensitivity of the occultation delay to large vertical refractivity gradients, implying that climatic changes in the height and magnitude of systematically large vertical refractivity gradients may contribute a significant portion of long-term trends and variability in the occultation delay observable. Therefore to interpret observed

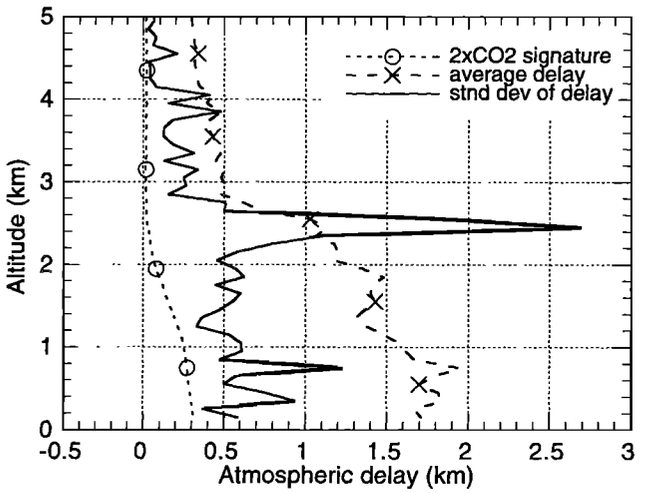

Figure 25. Atmospheric propagation delay at low latitudes: comparison of change in delay at low latitudes due to a doubling of atmospheric CO_2 (short-dashed line) as estimated by the NCAR community climate model [*Yuan et al.*, 1993] with the simulated average delay (long-dashed line) and standard deviation of delay (solid line) derived from the 63 radiosondes released from Hilo, Hawaii, during July, 1991.

changes in delay, climate models must have both sufficient vertical resolution to represent the large vertical gradients as well as adequate physical coupling between the gradients and the changes in radiative forcing which drive the purported changes in climate, posing an interesting challenge for the models.

4.2.2. Changes in Temperature near the Tropopause. Accurate, high vertical resolution temperature profiles of occultation measurements in the middle to upper troposphere and stratosphere provide an obvious tool for monitoring climatic variations complementing the very accurate but poor vertical resolution temperatures in this region and below produced by nadir-viewing microwave radiometers [*Spencer and Christy*, 1990]. Temperature monitoring in the stratosphere is expected to provide a relatively straightforward test of cooling predicted in response to observed increases in greenhouse gas concentrations. At somewhat lower altitudes, profiles in the upper troposphere through the lower stratosphere can be compared with the contrast expected between warming in the troposphere and cooling in the stratosphere, a signature which has been proposed as a detection fingerprint of climate change [*Epstein*, 1982; *Parker*, 1985; *Karoly*, 1987, 1989] but may be limited by inadequate knowledge of the sources and magnitude of natural variability producing similar signatures [*Liu and Schuurmans*, 1990]. The altitude at which warming reverses to cooling varies significantly between models, and comparisons between recent observations and model simulations indicate the model altitude is generally placed too high [*Houghton et al.*, 1990, chap. 8]. Trends reported by *Angell* [1988] indicate the upper troposphere may in fact be cooling. Results such as these are indicative of the need for accurate, long-term, and high vertical resolution observations in the tropopause regime which occultation observations can provide.

Measurements near the tropopause are well suited for observing the atmospheric response to impulsive changes in radiative forcing produced by massive volcanic injection of aerosol material into the upper troposphere and lower stratosphere. The global coverage and accuracy of individual GPS soundings in the stratosphere and upper troposphere allow one to peer inside and observe the spatial and temporal evolution of the thermal structure of the atmosphere as it adjusts to the changes in forcing, even in the presence of significant aerosol loading and clouds.

4.2.3. High-latitude, near surface warming. Climate models generally predict enhanced near-surface warming at high-latitude regions during winter months in response to a doubling of atmospheric CO_2 concentrations [*Houghton et al.*, 1990, chap. 5]. The models also exhibit relatively large natural variability at high latitudes, implying early detection and interpretation of gradual climatic shifts in temperature may be difficult. Nonetheless, both the natural variations and the gradual climatic shift are of interest to understanding the processes and behavior of the system, and profiles of atmospheric density pressure and temperature derived from the radio occultation observations at high latitudes will be very accurate and therefore useful particularly under winter conditions.

4.2.4. Expansion of the troposphere due to global warming. Because the altitude of an atmospheric pressure level depends on the average temperature at lower altitudes, geopotential height offers a sensitive monitor of tropospheric warming [*Gary*, 1992], a task for which the accuracy and coverage of GPS occultations are well suited [*Kursinski et al.*, 1994]. Occultation-derived geopotential height is particularly well suited for characterizing climate because of its inherent spatial averaging in both the vertical (through hydrostatic equilibrium) and the horizontal (through the limb-viewing geometry) dimensions.

A change in temperature δT over a pressure interval P_{surf} to P will alter the height of P in accordance with hydrostatic balance such that

$$\delta z \equiv z\,T(z)\left\langle \frac{\delta T}{T^2} \right\rangle \tag{46}$$

where z is the original height of P, δz is the change in z due to δT, and $\langle \delta T/T^2 \rangle$ represents the value of $\delta T/T^2$ averaged over the height interval 0 to z. Since climate models generally predict tropospheric warming and stratospheric cooling [*Houghton et al.*, 1992], the largest pressure height increase is predicted near the tropopause. In the tropics, where the height and pressure of the tropopause are ~16 km and 100 mbar, (46) indicates a sensitivity of ~55 meters change per Kelvin change in average tropospheric temperature. At 300 mbar, the pressure height sensitivity is roughly 30 m K^{-1}.

Daytime GPS observations of geopotential height in the upper troposphere will be limited by a systematic 8 to 10 m variation in geopotential height over the course of the solar cycle because of incomplete calibration of the ionosphere, an error source which can be reduced with a higher-order ionosphere correction scheme (sections 3.7 and 3.14). A long-term record of geopotential height derived from nighttime occultations may be accurate to the 1 m level or better (section 3.14), which at the tropical tropopause represents a sensitivity to fluctuations in average tropospheric temperature of the order of 0.02 K, providing an extremely sensitive tropospheric thermometer!

Identifying changes in climate as anthropogenic in origin requires that the changes be distinct from natural climatological variations. Observed variability depends strongly on latitude and season with a distinct minimum at low latitudes [*Peixoto and Oort*, 1992]. Day-to-day and seasonal variations of tropical, tropospheric geopotential height are of the order of 25 m equivalent to fluctuations in average tropospheric temperature of the order of 1 K or less.

Two representative examples of equilibrium climate models, *Hansen et al.* [1984] and *Manabe and Wetherald* [1987], which both predict globally averaged surface warming of 4 K, predict increases in average tropospheric temperature of 4.6 K and 3.4 K, respectively, at low latitudes. The corresponding increases in the height of the 100 mbar level of 260 m and 180 m, respectively, are large in comparison with occultation

measurement accuracy and low-latitude natural variability. The IPCC average predicted warming rate of 0.3 K per decade [*Houghton et al.*, 1990] predicts the tropical 100 mbar level will rise ~16 m per decade, a rate at which tropospheric warming could become apparent in one to three decades. The small observational errors, small natural variability and relatively large global warming signature predictions in the low-latitude, upper troposphere are features characteristic of a "fingerprint" variable for diagnosing climate change and features useful in evaluating climate model realism and accuracy.

4.2.5. Changes in humidity. In the lower to middle troposphere, particularly in tropical regions, changes in water vapor abundances provide one of the most sensitive indicators of modeled climatic change [*Barnett and Schlesinger*, 1987; *Santer et al.*, 1990; *Schlesinger et al.*, 1990]. Water vapor profiles derived from GPS measurements will be most accurate in the lower troposphere at the tropical latitudes particularly in the marine boundary layer where expected accuracies below 7 km altitude are similar to goals established by the Global Energy and Water Cycle Experiment (GEWEX) [*Starr and Melfi*, 1991] and may therefore yield robust signatures of changing climate.

An understanding of the control of water vapor in the free troposphere is required to make accurate predictions of global warming because of the water vapor feedback effect. Present knowledge of water vapor in the free troposphere is poor. *Sun and Lindsen* [1993] have pointed out that tropical climatological humidities derived from radiosonde and SAGE observations differ by a factor of 2 [*Oort*, 1983; *Rind et al.*, 1993]. Tropical water vapor profiles derived from GPS observations cover the altitude regime where SAGE and radiosonde observations overlap, offering an independent data set with sufficient accuracy and insensitivity to clouds (which limits the SAGE data set in particular) to improve the climatology significantly beyond that of present knowledge.

4.3. Stratosphere-Troposphere Exchange

Concern over decreasing ozone abundances in the stratosphere and their possible anthropogenic causes have focused research on understanding exchange between the stratosphere and the troposphere. The tropopause is important in this context as the region across which exchange takes place. For instance, the extremely low water vapor mixing ratios observed in the lower stratosphere at tropical latitudes have been used to infer that tropospheric air is migrating upward into the stratosphere at these latitudes where the very cold temperatures of the tropical tropopause and strong temperature dependence of the saturation vapor pressure of water combine to "freeze-dry" the air during its upward passage [*Newell and Gould-Stewart*, 1981].

There has been much debate over whether the low water vapor mixing ratios require extremely cold temperatures associated with penetrative convection events or whether slow upward migration of air across the tropopause is adequate to explain the mixing ratios. Existing data sets are not adequate to resolve the issue. Radiosonde data have the necessary vertical resolution, but coverage in the tropics is spatially very uneven. Further, the low densities of the tropopause affect radiosonde accuracy because of corrections required for effects such as radiation which depends on cloud cover, cloud top temperatures, solar zenith angle, surface temperature, vertical temperature structure and vertical distribution of aerosols, ozone, water vapor, and carbon dioxide [*Finger and Schmidlin*, 1991; *McMillin et al.*, 1988]. Present estimates of the maximum magnitude of these errors are of the order of 1 to 3 K [*Ahnert*, 1991; *McMillin et al.*, 1988]. Research is under way to improve radiosonde data for climate applications [*Luers and Eskridge*, 1995]. In situ airborne observations are extremely important but very limited in spatial and temporal coverage. Tropopause temperatures derived with nadir-viewing passive sounders tend to be biased high because of coarse weighting functions and the combination of a relative temperature minimum and approximately isothermal structure.

GPS occultations will provide globally distributed, high vertical resolution temperature structure in the vicinity of the tropopause for characterizing the relationship between temperature and lower stratospheric water vapor densities and, in the process, constraining the transport mechanism. Since each 3 K decrease in temperature reduces the saturation vapor pressure of water by a factor of 2 at tropical tropopause temperatures, temperature accuracy of 1 K or better is needed to be consistent with knowledge of water vapor mixing ratios. As shown in Figures 12 and 15, GPS-derived temperatures near the tropopause should provide sub-Kelvin accuracy. Further, since the knee of the tropopause can be quite sharp, vertical resolution of ~1 km or better is needed to resolve the minimum temperature achieved by the upward migrating air mass.

Finally, assimilation of occultation profiles into general circulation models should improve the understanding of the basic behavior in the tropopause regime as well as the dynamics of troposphere-stratosphere exchange particularly using profiles retrieved in the vicinity of the InterTropical Convergence Zone (ITCZ), tropopause folds, and high-latitude tropopause region where air is believed to return from the stratosphere to the troposphere.

4.4. Polar Regions

The importance of high altitude clouds in global change lies both in the radiative warming influence they exert [*Houghton et al.*, 1990, chap. 3; *Cess et al.*, 1990] and in the heterogeneous chemistry pathways they enable, such as the role of polar stratospheric clouds in the depletion of ozone [*Solomon*, 1988, 1990]. While the radio occultation observations are quite insensitive to the cloud particulates, the very accurate and high vertical resolution profiles of density, pressure and temperature which they provide will yield quantitative information on conditions in which these clouds form and decay and may in fact detect the signature induced in the vertical structure by the radiative properties of the cloud.

Because of the concern over reduced stratospheric ozone concentrations, much interest exists in understanding the thermodynamic structure and dynamical evolution of the winter polar vortices where ozone depletions are greatest and continue to increase. From a dynamical standpoint the highly variable behavior of the northern hemisphere vortex is particularly interesting. The very cold lower stratosphere represents near-ideal conditions for GPS observations of density, pressure, and temperature, and the high-density of high-latitude occultation profiles from high inclination orbits provide a quantitative, high vertical resolution data set of density, pressure, and temperature with which to observe and model polar vortices. Again, these measurements are insensitive to the presence of Polar Stratospheric Clouds (PSCs).

4.5. Boundary Layer and Surface-Atmosphere Interactions

Energy, momentum, and mass are exchanged between the Earth's surface and the free atmosphere above across boundary layers. The importance of properly representing the depth and thermodynamic structure of boundary layers in global forecast and climate models has been pointed out by *Heckley* [1985], *Albrecht et al.* [1986] and *Betts and Ridgeway* [1989]. Their short vertical extent makes space-borne remote sensing of boundary layers difficult. Boundary layers, in regions of relatively smooth topography can be characterized by radio occultation, particularly layers with distinctive vertical refractivity structure distinguishing them from the free atmosphere

(Figures 4a and 4b near 3.8 km). Diurnal variations in the structure of continental boundary layers and near-surface thermal inversions characteristic of nocturnal conditions, particularly strong in high-latitude winter climates, will also produce distinctive signatures. The sensitivity of radio propagation measurements to small-scale refractivity structure in the atmosphere will therefore prove useful for understanding energy, momentum, and constituent transfer between surface and atmosphere and their parameterization within General Circulation Models (GCMs) [e.g. *Betts et al.*, 1992].

Evaporation of water provides an upward flux of latent heat which is the largest energy flux on a global scale from the surface to the atmosphere. The upward flux of water vapor has associated with it a large vertical humidity gradient near the surface. It may be possible to retrieve these gradients and therefore infer vertical water vapor fluxes in marine environments if sub-Fresnel scale vertical resolution can be achieved (section 2.5). The sensitivity of occultation scintillation measurements for inferring structure and intensity of boundary layer turbulence and therefore the turbulent transport of energy, momentum and chemical species should be explored. This may also provide useful constraints on the exchange of energy and mass between the surface and atmosphere.

4.6. Small-Scale Waves and Turbulence

4.6.1. Background. Small-scale waves transport momentum and energy within the atmosphere contributing to middle atmospheric circulation and structure with an importance that increases with height. For instance, gravity waves may be responsible for the extremely cold summer-time mesopause [*Fritts et al.*, 1984]. The ability to remotely sense turbulence allows the identification of areas of momentum and energy exchange in the atmosphere and may have commercial applications for airline traffic. Radio occultation observations provide a sensitive, high vertical resolution measure of density and temperature perturbations associated with waves and turbulence used to characterize their properties in the atmospheres of Venus, Jupiter, Titan, Uranus and Neptune [*Allison*, 1990; *Hinson and Tyler*, 1983; *Hinson and Magalhaes*, 1991, 1993; *Hinson and Jenkins*, 1995]. These features combined with global coverage suggest GPS occultations will provide a quantum step in observational capability for wave-related research in the Earth's atmosphere.

4.6.2. Resolution. The sensitivity to waves of any remote sensing technique depends on resolution. For occultation observations, waves divide into two classes, those whose vertical wavelengths are either larger or smaller than a Fresnel diameter. Observations of waves in the first class are interpreted in terms of geometric optics, whereas those in the second class require interpretation through diffraction theory. GPS observations smoothed to the Fresnel scale are sensitive to waves of vertical wavelengths greater than ~2 km and horizontal wavelengths larger than of the order of 200 km. Sensitivity to higher horizontal wavenumbers is dependent on the orientation of the wave fronts relative to the GPS signal ray path. Optimum sensitivity occurs when the wave fronts lie parallel to the GPS signal ray path such that the density perturbation along the horizontal averaging interval of the radio ray path is roughly constant and adds constructively. Several multiazimuthal slices through a wave field are necessary to constrain its horizontal structure and type as well as its phase and group velocities through the dispersion relation. A constellation of orbiting receivers would be very useful in this regard. The diffraction-limited resolution is adequate for resolving the dominant, vertical, gravity wave scales of 2 to >15 km observed in the middle atmosphere [*Muruyama et al.*, 1992].

4.6.3. Sensitivity. Sensitivity to wave profiles is limited by thermal noise and perhaps residual sub-Fresnel scale ionosphere structure (section 3.7). Since fractional thermal error scales with height as exp(z/H), whereas nondivergent wave amplitude grows as exp(z/2H), the greatest sensitivity to waves exists at lower altitudes, allowing waves to be traced back to their source in the lower atmosphere. The thermal noise contribution in Figure 13 indicates ~1-2 km vertical wavelength waves will be apparent at amplitudes of 1-2% at about 60 km altitude and ~0.001% at 10 km altitude, sensitivity which is borne out by the 0.1 K amplitude waves derived in the stratospheres of Uranus and Neptune from Voyager radio occultation observations [*Hinson and Magalhaes*, 1991, 1993].

4.6.4. Side-looking occultations. Because of their relatively large vertical component of group velocity, short horizontal wavelength gravity waves may transfer significant momentum and energy from the lower atmosphere to the middle and upper atmosphere. Observing this class of waves has proven difficult [*Fritts et al.*, 1989] and side-looking occultations offer a new approach. In a side-looking occultation the ray path is approximately orthogonal to the orbiting receiver velocity vector such that its motion through the atmosphere is primarily horizontal. The pencil-beam sampling volume has a cross-track horizontal resolution of ~1.4 km defined by the diameter of the first Fresnel zone (Figure 4b), 1 to 2 km vertical resolution roughly defined by the 50% bending interval (Figure 5), and a corresponding along-path horizontal averaging interval of 200 to 300 km. Sensitivity to short horizontal wavelengths as small as 1 km or less will occur when the wave fronts are aligned parallel to the GPS ray path as discussed above. Again, multiple azimuthal cuts through a region would constrain the properties of the waves.

4.6.5. Scintillations. Sub-Fresnel scale wave and turbulent structure create scintillations in the measured phase and amplitude. Small-scale waves and turbulence differ in that waves are resonant whereas turbulence is dissipative. The azimuthal assymetry of waves can be used to determine whether scintillations reveal the presence of a wave propagating through a region or a turbulent transfer of momentum to the background circulation.

Diffraction maps the spatial spectrum of the wave and turbulence structure in the dimension orthogonal to the motion of the signal path tangent point to a temporal spectrum of phase and amplitude variations [*Yeh and Liu*, 1982; *Hinson and Magalhaes*, 1991]. Scintillations observed during vertical and side-looking occultations are due primarily to sub-Fresnel scale structure in the vertical and horizontal dimensions, respectively and provide 1-D spatial spectra of small-scale atmospheric structure. On the basis of the Nyquist criteria the minimum resolvable spatial wavelength with 50 per second sampling is 100 m in the vertical and 250 m in the horizontal.

4.6.6. Sources and sinks. Determination of the spatial and temporal distribution of waves, their sources and sinks, and excitation and dissipation mechanisms has been limited by the distribution of the present, land-biased observational database of balloons, radars, and lidars. The global perspective from space is yielding promising results and insight [*Wu and Waters*, 1996]. The resolution, sensitivity, and global coverage of radio occultation data offer a global database with vertical resolution higher than other present satellite techniques spanning an altitude range from roughly the midtroposphere (limited by the water vapor ambiguity) into the mesosphere (limited by thermal noise and possibly ionospheric scintillations). In addition, occultation-derived electron densities in the ionosphere above 90 km can be used to study coupling between the ionosphere and the neutral atmosphere below. All of these occultation attributes can be applied to study the sources and sinks of atmospheric waves.

4.6.7. Present and future observations. Occultation observations are well suited for observing planetary Kel-

vin, Rossby-gravity and inertio-gravity waves trapped in the equatorial region. While these waves have been observed with radiosondes since the 1960s, their short vertical wavelengths have limited their detection from space. We see a great deal of equatorial wave activity in the 1 to 4 km vertical wavelength range in the initial GPS-MET data, far more than is apparent at higher latitudes. Waves with a ~3 km vertical wavelength have been identified as either a Rossby gravity or an inertio-gravity wave because of their large horizontal wavelength and extent and clear asymmetry across the equator of the vertical phase structure [*Kursinski et al.*, 1996], demonstrating the resolution and sensitivity of the data. Equatorial waves are believed to couple tropospheric convective activity to stratospheric circulation. In particular, the theory of the quasi-biennial oscillation (QBO) couples Kelvin and Rossby-gravity waves to the zonal wind pattern of the lower stratosphere. While it is presumed that equatorial waves are driven from below by tropospheric convection, a quantitative understanding of the excitation process is open to question. Occultation observations offer the first global data set with which to develop an understanding of the sources and sinks and coupling mechanisms, study their influence on exchange between the troposphere and the stratosphere, as well as a possible method for monitoring tropical convection vigor, frequency and organization, and variability with space and time.

5. Conclusions

An overview has been presented of the concept to utilize the GPS satellites and the radio occultation technique to observe the Earth's atmosphere. Refractivity is derived as a function of height, from which density, pressure, and temperature are derived in the cold regions of the atmosphere, while profiles of water vapor can be derived in the warm regions of the middle to lower troposphere. Three orbiting GPS receivers would provide a globally distributed set of daily profiles equal in number to that provided by the present radiosonde network and twice that if the receivers could also acquire signals from the GLONASS constellation. Derived profiles extend from the surface to roughly 60 km altitude and could possibly be pushed higher. The spatial resolution of the profiles is comparable to or exceeds that of GCMs providing much needed ~1 km or better vertical resolution throughout the troposphere during all weather conditions.

Errors limiting the accuracy of derived refractivity, pressure, temperature and water vapor divide into three altitude regimes. Errors above 30 km are dominated by measurement error, calibration error, and upper boundary errors, the magnitudes of which depend on instrument quality, the solar and diurnal cycles, and knowledge of atmospheric structure above ~60 km altitude. Because atmospheric refractivity grows exponentially with decreasing altitude, the fractional errors in refractivity, density, pressure, and temperature are generally maximum near 60 km and decrease rapidly at lower altitudes. Refractivity, pressure, and temperature errors at 60 km where the Abel and hydrostatic integrals are initialized are estimated to be 2-3%, ~200 m, and ~10 K, respectively, under nighttime solar maximum (or daytime solar minimum) conditions and a level of thermal noise expected of future instrumentation. Incomplete removal of the effects of the ionosphere during daytime solar maximum conditions using the present ionosphere calibration scheme will affect accuracy, particularly geopotential accuracy, above 20 to 30 km and can be improved with a better calibration scheme. Thermal error can be reduced at the expense of vertical resolution. Errors decrease exponentially below 60 km with decreasing altitude to about 30 km altitude.

The greatest accuracy is expected between 5 and 30 km altitude limited by errors caused by horizontal refractivity variations. Within this vertical interval, refractivity, geopotential and temperature errors of 0.2%, 8 to 20 m, and 0.2 to 0.4 K, respectively, are expected when the Abel transform is used to derive refractivity. With a more sophisticated retrieval process which incorporates horizontal refractivity structure, these errors will decrease possibly by an order of magnitude.

Near the surface the influence of water vapor dominates both in terms of refractivity errors due to horizontal refractivity structure and the ambiguity in separating the dry and moist contributions to total refractivity. Simulations indicate rms refractivity error increases near the surface to ~1%, a result which will depend on latitude and seasonal conditions. The wet/dry ambiguity of tropospheric refractivity which limits the accuracy of geopotential and temperature derived in the lower troposphere exhibits a strong seasonal and latitudinal dependence. At low latitudes, temperatures accurate to 1-2 K will be limited to altitudes above 8 km. In contrast, under the very dry, high-latitude winter conditions, derived geopotential and temperature accuracies of 20 m and 2 K or better should extend to the surface. Despite the limit imposed on low-latitude, lower troposphere temperature accuracy by the wet/dry ambiguity, accurate geopotential of pressure surfaces derived at the midtroposphere provide an accurate measure of average temperature in the lower troposphere. For example, knowledge of the 300 mbar geopotential to an accuracy of 8 m is equivalent to knowing the average temperature below 300 mbar to ~0.3 K.

Because of the strong temperature dependence of the saturation vapor pressure of water, the contribution of water vapor to refractivity increases dramatically with decreasing altitude in the lower troposphere. A latitudinally and seasonally varying altitude band of the order of 2 km thick exists above which very accurate temperature and geopotential profiles can be recovered and below which the occultation data are best used to derive water vapor. Within the 2 km transitional band, refractivity is very accurate, but the information content in the context of present knowledge of temperature and humidity is somewhat evenly weighted between the two with temperature and moisture accuracies of 3-5 K and 30-50%, respectively. At low latitudes, water vapor can be derived to 20% accuracy up to 6 to 7 km and to 1 to 5% within the boundary layer, depending on the accuracy to which near-surface refractivity can be derived. Midlatitude accuracies will depend on season. At 45^{o} latitude the altitude of 20% accuracy varies from approximately 5 km in the summer to 2-3 km in the winter hemisphere [*Kursinski et al.*, 1995].

Several applications have been described briefly, a number which will undoubtedly increase with time. With regard to weather prediction and physical process studies, a global set of occultation measurements would greatly extend the temporal and spatial coverage provided by the present radiosonde network. In particular, the characterization of weather systems which evolve over the ocean prior to moving over continents should be a natural application for this data set. Because of the coverage and resemblance to conventional in situ measurements, the radio occultation data are ideally suited to existing data assimilation techniques. Data assimilation systems can also enhance the impact of the occultation measurements by resolving the ambiguity between water vapor and temperature contributions to refractivity in the troposphere. Since the products of such data assimilation systems are expected to form the basic data sets for climate and physical process studies, GPS radio occultation measurements have the potential to significantly advance our understanding of the Earth's climate and of both natural and anthropogenic factors contributing to climate variations.

GPS occultations are well suited to the long-term needs of climate research because of their absolute accuracy. The one systematic error in long-term variations appears to be residual

daytime ionosphere error over the course of the solar cycle which is small (at 30 km altitude are ~30 m and ~1 K respectively and decreases to ~1 m and 0.01 K at 10 km altitude), and improvements of at least a factor of 3 are expected with a higher-order calibration scheme. Profiles derived at nighttime have no obvious long-term error and may be accurate at the hundredths of a Kelvin level both in terms of temperature and average tropospheric temperature implicit in observations of geopotential.

Several possible approaches have been discussed in which the occultation data could be used for monitoring and detecting anthropogenically induced climate change, including propagation delay, the transition from tropospheric warming to stratospheric cooling near the tropopause, expansion of the troposphere due to tropospheric warming, near-surface warming of the winter troposphere at high latitudes, and increased water vapor abundances in the lower troposphere associated with tropospheric warming. Of these, measuring the expansion of the troposphere using geopotential is particularly attractive because of large warming signatures predicted by models, low natural variability at low latitudes, and high measurement accuracy. Further, the accuracy of derived refractivity and the ease of its calculation in models makes refractivity a candidate as a climate variable as well.

The uniqueness of the observable, the atmospheric Doppler shift, combined with the independence of the retrieval process from initial model guesses except at the upper boundary, implies that errors in these observations will be independent of errors inherent to passive remote sensors and therefore provide an important database for assessing and sorting out observational accuracy in long-term climate data sets. For similar reasons the data may also be useful for calibrating other remote sensing or even in situ observations for weather.

The ability to acquire a global set of high vertical resolution observations insensitive to aerosols, clouds, and precipitation means atmospheric conditions can be observed during all atmospheric phases of the hydrological cycle, an important capability needed for GEWEX and a significant enhancement over the dry-biased conditions inherent to IR and visible observations. Further, the response of the atmosphere to changes in radiative forcing due to large injections of volcanic aerosols can be observed both inside and below the aerosol layers, avoiding some of the problems experienced by the UARS IR and visible sensors with the eruption of Mount Pinatubo.

The sensitivity of radio occultation observations to vertical wave structure demonstrated at the other planets and in the equatorial lower stratosphere in the GPS-MET results promises GPS occultations will provide an unprecedented sensitive, global, high vertical resolution database characterizing atmospheric waves and turbulence in the lower and middle atmosphere. The high horizontal sampling density and multiazimuthal scans provided by a constellation of orbiting receivers would be particularly useful in resolving ambiguities between candidate wave types and distinguishing between turbulence and small-scale waves.

In summary, the GPS occultation technique provides an unusual combination of important features complementary to other present and planned sensors. Further, the small size, simplicity, and low cost of GPS instrumentation required in comparison with other remote sensing instruments is an increasingly important attribute in today's era of shrinking research budgets and promises significant roles in the future.

Acknowledgments. The research described in this publication was largely performed at the Jet Propulsion Laboratory, California Institute of Technology, supported jointly by the National Aeronautics and Space Administration and Caltech through the Director's Discretionary Research Fund and the Caltech President's fund. K. R. Hardy was supported by the Independent Research program of Lockheed Martin Missiles & Space. We would like to thank Richard Goody, Dan McCleese, Duane Muhleman, and Richard Zurek for helpful comments on this manuscript, Stephen Leroy for comments and help in the geometric optics versus diffraction comparisons, and Charles Greenhall for help on the Fourier transform representation of the inversion process.

References

Ahnert, P. R., Precision and comparability of National Weather Service upper air measurements, paper presented at the Seventh Symposium on Meteorological Observations and Instrumentation, Natl. Weather Serv., New Orleans, La., 1991.

Albrecht, B. A., V. Ramanathan, and B. A. Boville, The effects of cumulus moisture transports on the simulation of climate with a general circulation model, *J. Atmos Sci., 43*, 2443-2462, 1986.

Allison, M., Planetary waves in Jupiter's equatorial atmosphere, *Icarus, 83*, 282-307, 1990.

Angell, J. K., Variations and trends in tropospheric and stratospheric global temperatures, 1958-1987, *J. Clim., 1*, 1296-1313, 1988.

Augstein, E., H. Schmidt, and F. Ostapoff, The vertical structure of the atmospheric planetary boundary layer in undisturbed trade wind over the Atlantic Ocean, *Boundary Layer Meteorol., 6*, 129-150, 1974.

Barnes, J. A., et al., Characterization of frequency stability, *IEEE Trans. Instrum. Meas., IM-20*, 105-120, 1971.

Barnett, T. P., and M. E.Schlesinger, Detecting changes in global climate induced by greenhouse gases, *J. Geophys. Res., 92*, 14,772-14,780, 1987.

Bassiri, B., and G. A. Hajj, Higher-order ionospheric effects on the global positioning system observables and means of modeling them, *Manuscr. Geod., 18*, 280-289, 1993.

Belloul, B., and A. Hauchecorne, Effect of periodic horizontal gradients on the retrieval of atmospheric profiles from occultation measurements, submitted to *Radio Sci., 32* (2), 469-478, 1997.

Bertiger, W. I., and S. Wu, Single frequency GPS orbit determination for low Earth orbiters, paper presented at the National Tech. Meeting, Inst. of Nav., Santa Monica, Calif., Jan. 1996.

Bertiger, W. I., et al., GPS precise tracking of TOPEX/POSEISON: Results and implications, *J. Geophys. Res., 99*, 24,449-24,464 , 1994.

Betts, A. K., and W. Ridgway, Climatic equilibrium of the atmospheric convective boundary layer over a tropical ocean, *J. Atmos. Sci., 46*, 2621-2641, 1989.

Betts, A. K., R. L. Desjardins, and J. I. MacPherson, Budget analysis of the boundary layer grid flights during FIFE 1987, *J. Geophys. Res., 97*, 18,533-18,546, 1992.

Born, M., and E. Wolf, *Principles of Optics*, 122 pp., 6th ed., Pergamon, New York, 1980.

Cess, R. D., et al., Intercomparison and interpretation of climate feedback processes in 19 atmospheric general circulation models, *J. Geophys. Res., 95*, 16,601-16,615, 1990.

Chahine, M. T., D. J. McCleese, P. W. Rosenkranz, and D. H. Staelin, Interaction mechanisms within the atmosphere, in *Manual of Remote Sensing*, edited by R.N.Colwell, pp. 165-230, Am. Soc. of Photogramm., Falls Church, Va., 1983.

Champion, K. S. W., A. E. Cole, and A. J. Kantor, Standard and reference atmospheres, in *Handbook of Geophysics and the Space Environment*, edited by A. S. Jursa, Air Force Geophys. Lab., Bedford, Mass., 1985.

Epstein, E. S., Detecting climate change, *J. Appl. Meteorol., 21*, 1172-1182, 1982.

Eyre, J. R., Assimilation of radio occultation measurements into a numerical weather prediction system, ECMWF Tech. Memo. 199, Eur. Cent. for Medium-Range Weather Forecasts, Geneva, 1994.

Finger, F. G., and F. J. Schmidlin, Upper-air measurements and instrumentation workshop, *Bull. Am. Meteorol. Soc, 72*, 50-55, 1991.

Fishbach, F. F., A satellite method for temperature and pressure below 24 km, *Bull. Am. Meteorol. Soc., 9*, 528-532, 1965.

Fjeldbo, G., and V. R. Eshleman, The atmosphere of Venus as studied with the Mariner 5 dual radio-frequency occultation experiment, *Radio Sci., 4*, 879-897, 1969.

Fjeldbo, G., A. J. Kliore, and V. R. Eshleman, The neutral atmosphere of Venus as studied with the Mariner V radio occultation experiments, *Astron. J., 76*, 123-140, 1971.

Fritts, D. C., et al., Research status and recommendations from the Alaska Workshop on Gravity Waves and Turbulence in the Middle Atmosphere Fairbanks, Alaska 18-22 July 1983, *Bull. Am. Meteorol. Soc, 65*, 149-159, 1984.

Fritts, D. C., R. C. Blanchard and L. Coy, Gravity wave structure between 60 and 90 km inferred from space shuttle reentry data, *J. Atmos. Sci., 46*, 423-434, 1989.

Gary, B. L., A novel method for monitoring global warming using unmanned aerial vehicles and GPS receivers, in White Paper, Jet Propul. Lab., Pasadena, Calif., 1992.

Gorbunov, M. E., and A. S. Gurvich, Interpretation of the GPS/MET

data. diffraction and multipath effects in the lower troposphere, submitted to *J. Geophys. Res.*, 1997.

Gorbunov, M. E., A. S. Gurvich, and L. Bengtsson, Advanced algorithms of inversion of GPS/MET satellite data and their application to reconstruction of temperature and humidity, *Rep. 211*, Max Planck-Inst. for Meteorol., Hamburg, 1996.

Gorbunov, M. E., and S. V. Sokolovskiy, Remote sensing of refractivity from space for global observations of atmospheric parameters, *Rep.119*, Max Planck-Inst. for Meteorol., Hamburg, 1993.

Hajj, G. A., and E. R. Kursinski, Analysis of errors in the vertical temperature profiles recovered from GPS occultation observations, *Eos Trans. AGU, 72* (44), Fall Meet. Suppl., 372, 1991.

Hajj, G.A., R. Ibanez-Meier, E. R. Kursinski and L. J. Romans, Imaging the ionosphere with the Global Positioning System, *Int. J. Imaging Syst. and Technol., 5*, 174-184, 1994.

Hajj, G. A., E. R. Kursinski, W. I. Bertiger, S. S. Leroy, T. Meehan, L. J. Romans, and J. T. Schofield, Initial results of GPS-LEO occultation measurements of Earth's atmosphere obtained with the GPS-MET experiment, paper presented at the IUGG XXI General Assembly, Int. Union of Geod. and Geophys., Boulder, Colo., July 2-14, 1995.

Hansen, J., A. Lacis, D. Rind, L. Russell, P. Stone, I. Fung, R. Ruedy, and J. Lerner, Climate sensitivity analysis of feedback mechanisms, in *Climate Processes and Climate Sensitivity, Geophy. Monogr.*, vol. 29, edited by J. Hansen and T. Takahashi), pp. 130-163, AGU, Washington, D. C., 1984.

Hardy, K. R., D. P. Hinson, G. L. Tyler, and E. R. Kursinski, Atmospheric profiles from active space-based radio measurements, paper presented at the 6th Conference on Satellite Meteorology and Oceanography, Am. Meteorol. Soc., Atlanta, Ga., January 5-10, 1992.

Hardy, K. R., G. A. Hajj, and E. R. Kursinski, Accuracies of atmospheric profiles obtained from GPS occultations, *Int. J. Satell. Commun., 12*, 463-473, 1994.

Haugstad, B. B., Effects of the inhomogenoeus background on radiation propagating through turbulent planetary atmospheres, *Radio Sci., 13*, 435-440, 1978.

Heckley, W. A., Systematic errors in the ECMWF operational forecasting model in tropical regions, *Q. J. R. Meteorol. Soc., 11*, 709-738, 1985.

Hinson, D. P., and J. M. Jenkins, Magellan radio occultation measurements of atmospheric waves on Venus, *Icarus, 114*, 310-327, 1995.

Hinson, D. P., and J. A. Magalhaes, Equatorial waves in the stratosphere of Uranus, *Icarus, 94*, 64-91, 1991.

Hinson, D. P., and J. A. Magalhaes, Inertio-Gravity Waves in the Atmosphere of Neptune waves in Neptune, *Icarus, 105*, 142-161, 1993.

Hinson, D. P., and G. L. Tyler, Internal gravity waves in Titan's atmosphere observed by Voyager radio occultation, *Icarus, 54*, 337-352, 1983.

Hoskins, B. J., M. E. McIntyre, and A. W. Robertson, On the use and significance of isentropic potential vorticity maps, *Q. J. Meteorol., 111*, 877-946, 1985.

Houghton, J. T., G. J. Jenkins and J. J. Ephraums (eds.), *Climate Change, The IPCC Scientific Assessment*, Univ. of Cambridge, Cambridge, England, 1990.

Janjic, Z. I., The step-mountain coordinate physical package, *Mon. Weather Rev., 118*, 1429-1443, 1990.

Karayel, E. T., and D. P. Hinson, Sub-Fresnel-scale vertical resolution in atmospheric profiles from radio occultation, *Radio Sci., 32* (2), 411-423, 1997.

Karoly, D. J., Southern Hemisphere temperature trends: A possible greenhouse gas effect?, *Geophys. Res. Lett., 14*, 1139-1141, 1987.

Karoly, D. J., Northern Hemisphere temperature trends: A possible greenhouse gas effect?, *Geophys. Res. Lett., 16*, 465-468, 1989.

Kelley, M. C., *The Earth's Ionosphere: Plasma Physics and Electrodynamics*, 487 pp., Academic, San Diego, Calif., 1989.

Kerr, R. A., A military navigation system might probe lofty weather, *Science, 256*, 318-319, 1992.

Kliore, A. J., and I. R. Patel, Thermal structure of the atmosphere of Venus from Pioneer Venus radio occultations, *Icarus, 52*, 320-334, 1982.

Kuo, Y.-H., X. Zou, and W. Huang, The impact of GPS data on the prediction of an extratropical cyclone: An observing system simulation experiment, *J. Dyn. Atmos. Ocean*, in press 1996.

Kursinski, E. R., Monitoring the Earth's atmosphere with GPS, *GPS World, 5*, 50-54, 1994.

Kursinski, E. R., The GPS radio occultation concept: theoretical performance and initial results, Ph.D. thesis, Calif. Inst. of Technol., Pasadena, 1997.

Kursinski, E. R., G. A. Hajj, and K. R. Hardy, Observing Climate Change with the Global Positioning System, *Eos Trans. AGU, 75* (44), 114, 1994.

Kursinski, E. R., G. A. Hajj, K. R. Hardy, L. J. Romans and J. T. Schofield, Observing tropospheric water vapor by radio occultation using the Global Positioning System,*Geophys. Res. Lett., 22*, 2365-2368, 1995.

Kursinski, E. R., et al., Initial results of radio occultation observations of Earth's atmosphere using the Global Positioning System, *Science , 271*, 1107-1110, 1996.

Leroy, S. S., Measurement of geopotential heights by GPS radio occultation, *J. Geophys. Res., 102*, 6971-6986, 1997.

Lindal, G. F., The atmosphere of Neptune: An analysis of radio occultation data acquired with Voyager 2, *Astron. J., 103*, 967-982, 1991.

Lindal, G. F., G. E. Wood, H. B. Hotz, D. N. Sweetnam, V. R. Eshleman, and G. L. Tyler, The atmosphere of Titan: An analysis of the Voyager 1 radio occultation measurements, *Icarus, 53*, 248-263, 1983.

Lindzen, R. S., and M. Fox-Rabinovitz, Consistent vertical and horizontal resolution, *Mon. Weather Rev., 117*, 2575-2583, 1989.

Linfield, R., The effect of aperture averaging upon tropospheric delay functions seen with a DSN antenna, *Telecommun. Data Acquisition Prog. Rep. 42-124*, pp. 1-7, Jet Propul. Lab., Pasadena, Calif., 1996.

Liu, Q., and C. J. E. Schuurmans, The correlation of tropospheric and stratospheric temperatures and its effect on the detection of climate changes, *Geophys. Res. Lett., 17*, 1085-1088, 1990.

Luers, J. K., and R. E. Eskridge, Temperature corrections for the VIZ and Vaisala radiosondes, *J. Appl. Meteorol., 34*, 1241-1253, 1995.

Lusignan, B., G. Modrell, A. Morrison, J. Pomalaza, and S. G. Ungar, Sensing the Earth's atmosphere with occultation satellites, *Proc. IEEE, 4*, 458-467, 1969.

Manabe, S., and R. T. Wetherald, Large scale changes of soil wetness induced by an increase in atmospheric carbon dioxide, *J. Atmos. Sci., 44*, 1211-1235, 1987.

Marouf, E. A., G. L. Tyler, and P. A. Rosen, Profiling Saturn's rings by radio occultation, *Icarus, 68*, 120-166, 1986.

McMillin, L. M., M. E. Gelman, A. Sanyal, and M. Sylva, A method for the use of satellite retrievals as a transfer standard to determine systematic radiosonde errors, *Mon. Weather Rev., 116*, 1091-1102, 1988.

Mesinger, F., Z. I. Janjic, S. Nickovic, D. Gavrilov, and D. G. Deaven, The step-mountain coordinate-model description and performance for cases of alpine lee cyclogenesis and for a case of an Appalachian redevelopment, *Mon. Weather Rev., 116*, 1493-1518, 1988.

Muruyama, Y., T. Tsuda, M. Yamamoto, T. Nakamura, T. Sato, S Kato, and S. Fukao, Dominant vertical scales of gravity waves in the middle atmosphere observed with the MU radar and rocketsondes, *J Atmos. Terr. Phys., 54*, 339-346, 1992.

National Research Council (NRC), *The Global Positioning System A Shared National Asset: Recommendation for Technical Improvements and Enhancements*, p. 6, Committee on the future of the Global Positioning System, National Academy Press, Washington, D. C. 1995.

Newell, R. E., and S. Gould-Stewart, A Stratospheric Fountain?, *J. Atmos. Sci., 38*, 2789-2796, 1981.

Oort, A. H., Global atmospheric circulation statistics 1958-1973, *NOAA Prof. Pap. 14*, 180 pp., U.S. Gov. Print. Off., Washington, D. C., 1983.

Owens, J. S., Optical refractive index of air: Dependence on pressure, temperature and composition, *Appl. Opt., 6*, 51-58, 1967.

Papas, C. H., Theory of electromagnetic wave propagation, McGraw-Hill, New York, 1965.

Papoulis, A., *Probability, Random Variables, and Stochastic Processes*, 2nd ed., 235 pp., McGraw-Hill, New York, 1984.

Parker, D. E., On the detection of temperature changes induced by increasing atmospheric carbon dioxide" *Q.J.R. Meteorol. Soc , 111*, 587-601, 1985.

Peixoto, J. P., and A. H. Oort, *Physics of Climate*, 520 pp., Am. Inst. Phys, New York, 1992.

Rich, F. J., and S. Basu, Ionospheric Physics, in Handbook of Geophysics and the Space Environment, edited by A. S. Jursa, Air Force Geophys. Lab., Bedford, Mass., 1985.

Rind, D., E.-W. Chiou, W. Chu, S. Oltmans, J. Lerner, J. Larsen, M. P. McCormick, and L. McMaster, Overview of the Stratospheric Aerosol and Gas Experiment II water vapor observations: Method, validation, and data characteristics, *J. Geophys. Res., 98*, 4835-4856, 1993.

Santer, B. D., T. M. I Wigley, M. E. Schlesinger, and P. D. Jones, Multivariate methods for the detection of greenhouse-gas-induced climate change, in *Greenhouse-Gas-Induced Climatic Change: A Critical Appraisal of Simulatiuons and Observations*, edited by M.E.Schlesinger, Elsevier Sci., New York, 1990.

Schlesinger, M. E., T. P.Barnett and X. J. Jiang, On greenhouse gas signal detection strategies, in *Greenhouse-Gas-Induced Climatic Change: A Critical Appraisal of Simulations and Observations*, edited by M.E.Schlesinger, Elsevier Sci., New York, 1990.

Smith, E. K., and S. Weintraub, The constants in the equation for atmospheric refractive index at radio frequencies, *Proc. IRE, 41*, 1035-1037, 1953.

Solomon, S., The mystery of the Antarctic ozone "hole", *Rev. Geophys., 26*, 131-148, 1988.

Solomon, S., Progress towards a quantitative understanding of Antarctic ozone depletion, *Nature, 347*, 347-354, 1990.

Spencer, R. W., and J. R. Christy, Precise monitoring of global temperature trends from satellites, *Science, 247*, 1558-1562, 1990.

Spilker, J. J., GPS signal structure and performance characteristics, *Navigation, 25*, 29-54, 1978.

Starr, D. O'C., and S. H. Melfi (Eds.), The role of water vapor in climate, A strategic research plan for the proposed GEWEX water vapor project (GVaP), *NASA Conf. Publ. 3120*, 1991.

Sun, D. Z., and R. S. Lindsen, Water vapor feedback and the ice-age snowline record, *Ann. Geophys., 11*, 204-215, 1993.

Thayer, G. D., An improved equation for the radio refractive index of air, *Radio Sci., 9*, 803-807, 1974.

Treuheft, R. N., and G. E. Lanyi, The effect of the dynamic wet troposphere on radio interferometric measurements, *Radio Sci., 22*, 251-265, 1987.

Tyler, G. L., D. N. Sweetnam, J. D. Anderson, J. K. Campbell, V. R. Eshleman, D. P. Hinson, G. S. Levy, G. F. Lindal, E. A. Marouf, and R. A. Simpson, Voyager 2 radio science observations of the Uranian system: Atmosphere, rings, and satellites, *Science, 233*, 79-84, 1986.

Tyler, G.L., et al., "Voyager Radio Science Observations of Neptune and Triton", *Science, 246*, 1466-1473, 1989

Vorob'ev, V. V., and T. G. Krasil'nikova, Estimation of the accuracy of the atmospheric refractive index recovery from Doppler shift measurements at frequencies used in the NAVSTAR system, *Phys. Atmos. Ocean, 29*, 602-609, 1994.

Ware, R., et al., GPS sounding of the atmosphere from low Earth orbit - preliminary results, *Bull. Am. Meteorol. Soc., 77*, 19-40, 1996.

Wu, D. L., and J. W. Waters, Variances: A possible indication of gravity waves, *Geophys. Res. Lett.*, in press, 1996.

Wu, S. C., W. I. Bertiger, and J. T. Wu, Minimizing selective availability error on TOPEX GPS measurements, paper presented at the Conference on Astrodynamics, Am. Inst. of Aerosnaut. and Astronaut./Am. Astron. Soc., Portland, Oreg., Aug. 20-22, 1990.

Yeh, K. C., and C. H. Liu, Radiowave scintillations in the ionosphere, *Proc. IEEE, 70*, 324-360, 1982.

Yuan, L. L., R. A. Anthes, R. H. Ware, C. Rocken, W. D. Bonner, M. G. Bevis and S. Businger, Sensing climate change using the global positioning system, *J. Geophys. Res., 98*, 14,925-14,937, 1993.

Yunck, T. P., G. F. Lindal and C. H. Liu, The role of GPS in precise Earth observation, paper presented at the Symposium on Position, Location and Navigation Symposium, Orlando, Fla., Nov. 29 to Dec. 2, 1988.

Zou, X., Y.-H. Kuo, and Y.-R. Guo, Assimilation of atmospheric radio refractivity using a nonhydrostatic adjoint model, *Mon. Weather Rev., 123*, 2229-2249, 1995.

G. A. Hajj, E. R. Kursinski , R. Linfield and J. T. Schofield, Jet Propulsion Laboratory, California Institute of Technology, Pasadena, Ca 91109. (e-mail: hajj@maggie.jpl.nasa.gov; erk@mercu1.caltech.edu; linfield@jpl.nasa.gov; tim@scn1.jpl.nasa.gov)

K. Hardy, AS&T, 1520-208 Sand Hill Road, Palo Alto, CA 94304, khardy@batnet.com

(Received June 6, 1996; revised January 31, 1997;
accepted April 22, 1997.)